

# UNIVERSITY OF MISKOLC

Faculty of Mechanical Engineering and Information Technology



**MISKOLCI**  
EGYETEM  
UNIVERSITY OF MISKOLC

## DEVELOPMENT AND EVALUATION OF THERMAL MODELS FOR ANGULAR CONTACT BALL BEARINGS IN SPINDLE SYSTEMS

**PhD Dissertation**

**Author:**

**Sebastián Cabezas**

Mechatronics Engineering (BSc),  
Mechanical Engineering (MSc)

**István Sályi Doctoral School of Mechanical Engineering Sciences**

**Head of Doctoral School**

**Dr. Gabriella Bognár**

DSc Full Professor

**Head of Topic Group**

**Dr. György Hegedűs**

Associate Professor

**Scientific Supervisors**

**Dr. György Hegedűs**

Associate Professor

**Dr. Péter Bencs**

Associate Professor

Miskolc, 2025



# Acknowledgments

With sincere gratitude, I would like to thank my supervisors Dr. Hegedűs György, and Dr. Bencs Péter, for undertaking the challenging task of guiding my doctoral studies. I am deeply thankful to them not only for their scientific support, but also for their guidance and encouragement in my personal life. Without their guidance and help, the good things that have happened in my life would not have been possible.

I would like to thank my family, to whom I owe all my achievements. They are the core of my life.

To my love, Mila, for your support, conversations, and endless wonderful moments we share.

I want to thank my friends who were encouraging me to pursue my dreams and for offering their invaluable advice and support.

I want to thank to the University of Miskolc for all the knowledge I have been able to acquire.

I want to thank this wonderful land, Hungary, for allowing me to grow and develop in various aspects of my life. Additionally, I extend my heartfelt thanks to my home country, Ecuador, for the privilege of being its citizen.

Finally, and most important, I want to thank God, my creator and savior.

Sebastian Cabezas

December, 2024

# Contents

<b>1</b>	<b>Introduction and Objectives</b>	<b>1</b>
1.1	Objectives . . . . .	3
<b>2</b>	<b>Literature review. State of the art</b>	<b>5</b>
2.1	Assembly analysis, type of loads, and the variation of the contact angle in ACBB . . . . .	5
2.1.1	Type of bearing arrangement in a spindle unit . . . . .	6
2.1.2	Type of loads in a rolling bearings of spindle units . . . . .	6
2.1.3	Analysis of the variation of the contact angle . . . . .	8
2.2	Frictional moments in angular contact ball bearings of spindle units . . . . .	9
2.3	Hertzian contact in rolling contact between two bodies . . . . .	12
2.4	Lubrication film between the rings and the balls of the angular contact ball bearing . . . . .	13
2.5	Heat generation analysis in rolling bearings of spindle systems . . . . .	14
2.5.1	Heat partitioning . . . . .	15
2.6	Thermal models for rolling bearings based on FEM and CFD simulations . .	16
2.7	Thermal resistance networks for rolling bearings in spindle units . . . . .	17
2.7.1	Methods of solution of the system of equations describing thermal resistance models . . . . .	22
2.7.2	Steady-space approach and Euler's method . . . . .	23
2.8	Conclusion of the chapter . . . . .	24
<b>3</b>	<b>Methodology of Study</b>	<b>26</b>
3.1	Thermal analysis of rolling bearings in spindle units . . . . .	26
3.2	Representative model of the bearing arrangement . . . . .	27
3.3	Dynamic equivalent radial load . . . . .	27
3.4	Determination of the rolling contact . . . . .	29
3.5	Determination of the fluid film parameters . . . . .	32
3.5.1	Determination of the kinematic viscosity . . . . .	33
3.5.2	Determination of the fluid film thickness . . . . .	34
3.5.3	Determination of the convective coefficient of the lubricant film . . . . .	35
3.6	Convective coefficients of air surrounding the housing . . . . .	37
3.7	Determination of the frictional moments . . . . .	40
3.8	Determination of the heat generation . . . . .	43
3.9	Thermal contact resistances . . . . .	46
3.9.1	Thermal resistance formulation for static cylindrical components . . . .	47
3.9.2	Thermal resistances of the Mellor thermal network . . . . .	47

3.9.3	Thermal contact resistances for static, moving, and combined heat sources . . . . .	49
3.9.3.1	Thermal contact resistances for stationary heat sources . . . . .	49
3.9.3.2	Thermal contact resistances for moving heat sources . . . . .	49
3.9.3.3	Thermal contact resistances for combined heat sources . . . . .	50
3.9.4	Thermal constriction resistance . . . . .	52
3.9.5	Thermal resistances by convection . . . . .	53
3.10	State Space Method for monitoring thermal fields in rolling bearings of spindle systems . . . . .	53
3.11	Conclusion of the chapter . . . . .	55
<b>4</b>	<b>Dark Gray-Box LPTN</b>	<b>56</b>
4.1	Definition of the DGB Lumped parameter thermal network . . . . .	56
4.2	Development of the DGB thermal network . . . . .	57
4.3	Results and new contributions . . . . .	59
4.3.1	Mathematical model of the Dark Gray-Box LPTN . . . . .	59
4.3.2	Solutions in stationary state using the State-Space approach . . . . .	59
4.3.2.1	Experimental validation of the Dark Gray-Box LPTN . . . . .	60
4.3.2.2	Finite Element Analysis Simulation . . . . .	61
4.3.2.3	Dark Gray-Box LPTN model validation for stationary conditions . . . . .	63
4.3.3	Dark Gray-Box LPTN. Solutions in continuous time. . . . .	67
4.3.4	Conclusion of the chapter . . . . .	71
<b>5</b>	<b>Light Gray-Box and White-Box LPTN</b>	<b>72</b>
5.1	Development of the LGB and WB thermal networks . . . . .	72
5.2	Results and new contributions . . . . .	74
5.2.1	Mathematical model of the Light Gray-Box LPTN . . . . .	74
5.2.2	Mathematical model of the White-Box LPTN . . . . .	75
5.2.2.1	Light Gray-Box LPTN model validation for stationary conditions . . . . .	76
5.2.2.2	White-Box LPTN model validation for stationary conditions . . . . .	79
5.2.3	Light Gray-Box LPTN. Solutions in continuous time. . . . .	81
5.2.4	White-Box. Solutions in continuous time . . . . .	83
5.2.5	Conclusion of the Chapter . . . . .	86
<b>6</b>	<b>New scientific results and contributions</b>	<b>87</b>
6.1	Theses . . . . .	87
6.2	Related publications . . . . .	90

# Nomenclature

$\dot{Q}_f$	Total heat generation (W)
$\dot{Q}_i$	Heat generation in the inner-ring (W)
$\dot{Q}_o$	Heat generation in the outer-ring (W)
$a$	Semi-major axis (mm)
$b$	Semi-minor axis (mm)
$C_0$	Basic static load rating (N)
$D_2$	Outer-ring shoulder diameter (mm)
$d_2$	Shoulder of the inner- ring of the bearing in the smallest front surface (mm)
$d_m$	Mean diameter of the bearing (mm)
$D_{pw}$	Pitch diameter (mm)
$D_w$	Diameter of the ball (mm)
$E$	Young's modulus (GPa)
$e$	Eccentricity of the ellipse
$f_0$	Coefficient of rolling friction
$f_1$	Friction coefficient related to loading direction (Nmm)
$F_a$	Axial or thrust load (N)
$F_r$	Radial load (N)
$G^*$	Dimensionless material parameter
$h_b$	Heat convection coefficient of the oil-film related to the balls ( $\frac{W}{m^2K}$ )
$h_b$	Heat convection coefficient of the oil-film related to the outer-rings ( $\frac{W}{m^2K}$ )
$H_{IR}$	Minimum oil-film thickness for the inner-ring (mm)
$h_i$	Heat convection coefficient of the oil-film related to the inner-ring ( $\frac{W}{m^2K}$ )
$h_{lub}$	Heat convection coefficient of the oil-film ( $\frac{W}{m^2K}$ )
$H_{OR}$	Minimum oil-film thickness for the outer-ring (mm)
$k$	Thermal conductivity of the elements of the angular contact ball bearing ( $\frac{W}{mK}$ )
$K_1(e, \frac{\pi}{2})$	Complete elliptic integral of the first kind
$K_2(e, \frac{\pi}{2})$	Complete elliptic integral of the second kind

$k_{air}$	Thermal conductivity of the air surrounding the housing ( $\frac{W}{mK}$ )
$k_{oil}$	Thermal conductivity of the lubricant ( $\frac{W}{mK}$ )
$L$	Width of the housing (mm)
$M_f$	Total frictional moment (Nmm)
$M_{rr}$	Rolling frictional moment (Nmm)
$M_{sl}$	Sliding frictional moment (Nmm)
$n$	Rotational speed (rpm)
$Nu$	Nusselt number
$Nu_{air}$	Nusselt number of the air related to the housing
$Nu_b$	Nusselt number of the lubricant related to the ball
$Nu_i$	Nusselt number of the lubricant related to the inner-ring
$Nu_o$	Nusselt number of the lubricant related to the outer-ring
$P(x, y)$	Pressure distribution over the ellipse (MPa)
$P_m$	Dynamic equivalent radial load (N)
$Pr$	Prandtl number
$Pr_f$	Prandtl number of the air film
$Pr_w$	Prandtl number of air and the surface of the housing
$r_b$	Radius of the ball (mm)
$r_{ext.}$	External radius (mm)
$r_{int.}$	Internal radius (mm)
$r_i$	Radius of the inner-ring (mm)
$r_o$	Radius of the outer-ring (mm)
$R_{th}$	Thermal contact resistance ( $\frac{K}{W}$ )
$Ra_{th}, Rb_{th}, Rc_{th}, Rm_{th}$	Thermal contact resistances of the Mellor thermal network ( $\frac{K}{W}$ )
$Re$	Reynolds number
$Re_{air}$	Reynolds number of the air
$Re_b$	Reynolds number for the balls
$Re_i$	Reynolds number for the inner-ring
$Re_o$	Reynolds number for the outer-ring
$t_r$	Ellipticity ratio
$T_b$	Temperature of the balls ( $^{\circ}C$ )
$T_b$	Temperature of the inner-ring ( $^{\circ}C$ )
$T_b$	Temperature of the shaft ( $^{\circ}C$ )
$T_{ho}$	Temperature of the housing / outer-ring subassembly ( $^{\circ}C$ )
$T_h$	Temperature of the housing ( $^{\circ}C$ )

$T_{lf}$	Final temperature of the lubricant ( $^{\circ}\text{C}$ )
$T_{li}$	Initial temperature of the lubricant ( $^{\circ}\text{C}$ )
$T_{lref}$	Reference temperature of the lubricant ( $^{\circ}\text{C}$ )
$T_{lub}$	Temperature of the lubricant ( $^{\circ}\text{C}$ )
$T_{op}$	Operational temperature ( $^{\circ}\text{C}$ )
$T_o$	Temperature of the outer-ring ( $^{\circ}\text{C}$ )
$Ta_i$	Taylor number for the inner-ring
$Ta_o$	Taylor number for the outer-ring
$U^*$	Dimensionless speed parameter
$v_{air}$	Air speed in cross flow ( $\frac{\text{m}}{\text{s}}$ )
$W^*$	Dimensionless force parameter
$x$	Coordinate of the major axis (mm)
$y$	Coordinate of the minor axis (mm)
$\dot{Q}_b$	Heat generation in the balls (W)
$\epsilon_r$	Radial clearance of the angular contact ball bearing (mm)
$\mu_1$	Sliding friction coefficient to change (Nmm)
$\mu_{sl}$	Coefficient of sliding friction
$\phi_{housing}$	Hydraulic diameter of the housing (mm)
$\Phi_{rs}$	Kinematic replenishment factor
$\Phi_{sl}$	Inlet shear heating reduction factor
$\alpha$	Contact angle ( $^{\circ}$ )
$\alpha_D$	Thermal diffusivity of the lubricant ( $\frac{\text{mm}^2}{\text{s}}$ )
$\beta$	Factor for the Vogel's equation ( $\frac{1}{^{\circ}\text{C}}$ )
$\eta$	Non-dimensional factor for semi-minor axis $b$
$\kappa_i$	Osculation of the inner-ring (mm)
$\kappa_o$	Osculation of the outer-ring (mm)
$\mu_0$	Sliding friction coefficient to change (Nmm)
$\nu$	Kinematic viscosity of the lubricant ( $\frac{\text{mm}^2}{\text{s}}$ )
$\nu_{lf}$	Kinematic viscosity of the lubricant at final reference temperature ( $\frac{\text{mm}^2}{\text{s}}$ )
$\nu_{li}$	Kinematic viscosity of the lubricant at initial reference temperature ( $\frac{\text{mm}^2}{\text{s}}$ )
$\nu_{ref}$	Kinematic viscosity of the lubricant at reference temperature ( $\frac{\text{mm}^2}{\text{s}}$ )
$\omega$	Rotational speed ( $\frac{\text{rad}}{\text{s}}$ )
$\rho_{IR}$	Curvature radius of the inner-ring (mm)

$\rho_{OR}$	Curvature radius of the outer-ring (mm)
$\nu$	Poisson's coefficient
$\xi$	Non-dimensional factor for semi-minor axis $a$

## Abbreviations

**ACBB** Angular Contact Ball Bearing

**CFD** Computational fluid dynamics

**DB** Back-to-back Arrangement

**DGB LPTN** Dark Gray-BoxLumped Parameter Thermal Network

**EHL** Elasto Hydodynamic Lubrication

**LPTN** Lumped Parameter Thermal Network

**FEA** Finite Element Analysis

**FEM** Finite Element Method

**LGB LPTN** Light Gray-Box Lumped Parameter Thermal Network

**rpm** Revolutions per minute

**TRD** Thermal Resistance Detector

**WB LPTN** White Box Lumped Parameter Thermal Network

# 1 Introduction and Objectives

A crucial factor influencing precision and accuracy in machine tools is the thermal behavior of the spindle units. Thermal errors in spindle units account for 60-70 % of the total errors of machine-tools [1], leading to critical conditions including permanent deformation of the machine elements, low machining precision, material wear, reduction of service life span, internal heat generation and dissipation, improper dynamic behavior, among other concerns [2]. Recent investigations demonstrate that the rolling bearings of the spindle units are highly impacted by the temperature increase within the spindle unit, which determine the structural temperature fluctuation in machining processes [3],[4],[5]. Angular contact ball bearings are mainly used in spindle units due to their capacity to accommodate and distribute radial and thrust loads produced due to external machining operations [6]. Furthermore, this type of bearing is suitable for implementation in spindles due its proper performance at high rotational speeds maintaining shaft balance. However, not only the forces acting on the bearings and the rotational speed determine the thermal behavior of these elements. It is also necessary to analyze and investigate essential factors including the assembly geometry and bearing arrangement [7], the effects of internal lubrication in the bearing [8], and stress analysis in the contact area between the inner components of the bearing (inner-ring, balls, outer-ring) [9].

The thermal analysis of bearings in spindles has primarily been conducted by three types of methodologies: numerical, experimental and analytical.

Numerical techniques involve the implementation and application of finite element analysis (FEA), and computational fluid dynamics (CFD) [10]. This is the most widely used technique for both developing and validating thermal models, owing to the vast availability of FEA and CFD software in the market. Furthermore, somewhat accurate results can be obtained through FEA and CFD simulations. This type of analysis involves defining correct boundary and initial conditions, adequate meshing of the elements, and simulation time. Nevertheless, it is limited by the high cost of the FEA software, and the large

amount of time that is required for each simulation.

Experimental techniques estimate values by applying devices capable of measuring the temperature distribution in the rolling bearings and other components of the spindle system. These devices include thermocouples, thermal resistance detectors (TRDs), thermal cameras [11], and more recent techniques such as passive optical sensors [12] and wireless temperature micro-sensors integrated onto the bearings [13]. In general, experimental techniques are primarily used to validate the results obtained by the numerical and analytical techniques. However, this type of analysis could incur high expenses due to the complexity of the instrumentation systems making it impractical in most applications.

The last methodology relates analytical techniques focused on the development of mathematical models to predict the thermal behavior of mechanical elements such as rolling bearings, shafts, housings, rings, among others. These analytical techniques can be categorized by their approaches. In the first approach, complex mathematical operations are used to obtain the solution of the energy equation to predict the thermal distribution in elements of known common geometries such as cylinders, rings, spheres or multilayered elements that emulate the mechanical components [14]. However, this approach is limited due to the high complexity involved in obtaining mathematical solutions for models represented by differential equations. When analyzing a compound element like the angular contact ball bearing, this approach may not yield adequate results.

The second and most popular analytical approach is the solution of lumped parameter thermal models. It has been implemented in the analysis of complex mechanisms with complex geometries including, electrical motors, turbines, blades, and many other mechanisms. This a versatile methodology, which enables the development of complex thermal models separating the elements as lumping parameters with nodes of finite capacitance or diffusion nodes, zero capacitance or arithmetic nodes, and infinite capacitance or constant temperature sources within a thermal model. The heat paths are represented by conductors, which encompass the complete structure of the elements of the thermal network, such as material properties, type of contact between the surfaces, the heat transfer mechanism, and time dependance [15].

Although many researchers have created lumped thermal models that have yielded important results in the prediction of thermal fields, several factors including the methods of solution in both stationary and transient state, the design of thermal resistances based on the type of heat sources (stationary, moving and combined), accurately conceptual-

izing low-order thermal models, and implementing thermal models capable of relating axial and radial heat flux, among others, could enhance and improve the development of thermal models for rolling bearings in spindle systems.

Considering the factors mentioned in the previous paragraph, the present PhD dissertation has as primary objective the development of new thermal models to determine the temperature distribution in rolling bearings, specifically angular contact ball bearings of spindle systems based on the global identification of low order lumped parameter thermal networks [16].

## 1.1 Objectives

The investigation, design and development of the thermal networks in this work has the following specific objectives:

- Conducting an extensive research based on recent and previous investigations related to the methodologies and theories of thermal analysis in rolling bearings, aiming to establish advancements made in this field. Subsequently, establish the current state of the art, which mainly focuses on thermal models for angular contact ball bearings of spindle units.
- Developing three thermal networks for angular contact ball bearings based on the global identification of low-order lumped parameter thermal networks and the heat transfer theory. The models involve the analysis of bearing configurations, the forces acting during machining operations, the analysis of frictional moments due to the contact between the inner components of the bearing, the lubrication type and its influence on heat dissipation, the generation of heat and the its main contributors.
- Implementing thermal resistances for real contact heat sources of stationary, moving and combined conditions, which arise due to elliptical contact. This implementation is based on the mathematical solutions proposed by Y. S. Muzychka and M.M. Yovanovich, along with the Hertzian contact theory. Furthermore, to enhance the predictability of the models, Mellor's formulation for cylindrical geometries for analyzing axial and radial heat flow is implemented on the inner- and outer-ring of the bearing.
- Setting up two methods of solution of the thermal models, which are mathematically

represented by systems of first-order ordinary homogeneous differential equations. The first novel methodology, is based on the state space approach, solving the thermal models as Multiple Input, Multiple Output (MIMO) systems for both stationary and transient state. The second methodology is based on the solution of continuous time-dependent systems. Both, the state-space approach and the continuous time dependent systems are solved using Python.

- Testing and validating the thermal models using FEA solutions based on ANSYS steady and transient state thermal. The simulations will be performed considering the elements of the angular contact ball bearing as separate, independent entities, while utilizing heat generation analysis as initial and boundary conditions. Furthermore, the effects of lubrication are implemented and analyzed through convective heat transfer analysis.
- Testing and validating the new lumped parameter thermal models experimentally using a bearing testing rig. In this rig, a representative model consisting of an angular contact ball bearing model SFK 7203BEP placed inside a housing emulates a rolling bearing in a spindle unit. Controlled radial force and rotational speed, and measurements are taken using Type-J thermocouples placed on the surfaces of the static elements of the representative model, including the housing and the outer-ring of the bearing. Additionally, a thermal camera is used to obtain measurements of the rotational parts, including the surface of the inner-ring and the surface of the cross-section of the shaft.

## 2 Literature review. State of the art

In the present chapter, recent and prior studies concerning the development and creation of thermal models of rolling bearings will be analyzed and discussed. These studies serve as the foundation for creating enhanced thermal models for rolling bearings in spindle units. The analysis of thermal behavior in rolling bearings of spindle units is crucial, with main factors such as assembly geometry, the effects of external loads during machining operations, the effects of variations in the contact angle, the analysis of frictional moments, the effects of lubrication type, the generation of heat inside the angular contact ball bearings being studied. Methodologies applied up to the present to find thermal solutions including numerical experimental and analytical solutions are examined. Subsequently, special attention is given to the development of novel thermal networks in rolling bearings of spindle units, with emphasis on the global identification of lumped parameter thermal networks. Furthermore, approaches for solving mathematical models in steady and transient state are analyzed.

### 2.1 Assembly analysis, type of loads, and the variation of the contact angle in ACBB

The thermal influence on the spindle systems has emerged as an important field for investigation, given that thermal errors account for about 70 % of the total error of a machine tool, affecting its accuracy and precision [17]. However, it is not just performance that must be considered; but the unnecessary consumption of energy, which will be dissipated as heat, should be minimized, making the spindle units more feasible and sustainable. Achieving this involves applying thermal models in both design and working phases. During the design phase, the thermal models can predict the temperature distribution. Subsequently, these models can be applied to calculate thermal deformations in the components of the spindle unit, thermal elongation, and thermal tilt angles [18]. Another significant advantage in the design phase could be the possibility to develop

computational analytical tools and packets specifically dedicated to analyzing the thermal field in spindles. In the working phase, the development of thermal models could serve as input for the thermal error compensation and thermal error control techniques [19]. For decades, several researches have been focused on the thermal error compensation to improve accuracy; however, real-time correction has been of high complexity to eliminate design defects related with the thermal phenomena [20],[21].

### **2.1.1 Type of bearing arrangement in a spindle unit**

Basically, the heat distribution analysis on the rolling bearings begins with the bearing design and arrangement. Primarily, the angular contact ball bearings of a spindle unit are mounted on the shaft in a back-to-back DB arrangement. This configuration offers low friction coefficient, high operation precision and cost-effectiveness, while also enabling support for high-temperatures at high-speeds [22], [23]. However, not only does the arrangement influence the thermal behavior of the rolling bearings, but also the type of load exerted, including thrust, radial, preload in axial and radial directions, and the centrifugal forces, which can induce different thermal phenomena [24]. To provide relevant information about the types of forces and the influence in the thermal performance of the bearings in the spindle units, this analysis begins discussing preloads. After that, the effects of axial loads are described, then the effects of radial loads.

The type of bearing arrangement is addressed at detail in Chapter 3, Section 3.1 Thermal analysis of rolling bearings in spindle units, and Section 3.2 Representative model of the bearing arrangement of the present manuscript.

### **2.1.2 Type of loads in a rolling bearings of spindle units**

The preload in axial and radial directions in the angular contact ball bearings is crucial to prevent skidding, to maintain rotational accuracy and sufficient stiffness in both axial and radial directions [25]. The proper preload identification can be achieved using the preload determination technology according to the operating conditions. Tao Xu et al. [26] proposed an analytical method to calculate the optimum preload for achieving excellent thermal performance under rotational speeds of 10000 rpm, resulting in only a slight increase in the bearing temperature. For speeds exceeding 10000 rpm, a maximum axial preload was established, which does not affect the safety-limited maximum

temperature increase. B. Bossmanns et al. [27] developed a finite difference model to characterize the power distribution of a high-speed motorized spindle, which was verified through experimental measurements using a preloading mechanism on the front bearings by a series of 23 compressive springs around the perimeter. The force on the springs was varied using a hydraulic chamber. The results not only validate the thermal model but also provide a set of values of axial preload on bearings, which can be utilized in thermal error control within the machine tool. Spring configurations have been proposed for use in bearing preload within spindles, along with active bearing load monitoring and control mechanisms. Jenq-Shyong Chen et. al [28] introduced a bearing arrangement, incorporating piezoelectric actuators and strain-gage sensors, along with an active bearing load monitoring and control mechanism. While this solution provided good results, it was observed that this type of configurations cannot meet the requirements with various cutting conditions. Furthermore, this type of configuration will raise the cost of a spindle exuberantly.

Despite its simple design, several complexities appear in analyzing the internal load distribution of a ball bearing. In most studies, closed-form solutions have been implemented. These types of solutions deal in general with ring displacement and do not properly account for the change in contact angle. In this sense, the prediction of the frictional moments will not be accurate, and the determination of temperature distributions will not be accurate as well. General solutions were proposed by A. B. Bones [29]. In his work exact solutions for internal load distribution were found for ball bearings. The study extended the scope in the determination for an entire assemble unit, including bearings, shaft and the housing. The solutions not only define the formulation to find the forces acting on the bearing, but the elastic compliance of a point on the shaft with respect to the housing in five degrees of freedom. Based upon this contribution, mathematical models to determine radial, and axial loads were proposed, in which the contact angle variations are considered.

During machining operations, two main types of loads occur in the rolling bearings of the spindle unit: thrust loads and radial loads [30] (see Fig. (1)). The thrust load produces three main effects. First, deformation in the axial direction, leading to an increase of diametral clearance. Second, the nominal contact angle changes. Third, it decreases the lifetime of the bearings due to material fatigue [31]. A correct load distribution will minimize the axial load distribution, leading to operation mostly under radial loads, which

are optimal for the functioning of the rolling bearings.

The radial loads are absorbed by the angular contact ball bearings, resulting in two main effects. First, they distribute the radial load through the inner components of the bearings. Second, they allow the spindle unit to function adequately under rotational movement.

The axial and radial forces must be in balance; thus, skidding can be avoided. This phenomenon occurs when the applied bearing load is inadequate for developing enough elastohydrodynamic tractive force between the raceway and the rolling elements, leading to shear stresses of significant magnitude in the contact area [32],[33]. The raceway control was a common analytical assumption to analyze high speed ball bearings, introduced by T.A. Harris [34]. It assumed that the balls roll relative to the controlling raceway and roll and spin with respect to the non-controlling raceway. Hence, skidding of the ball is determined by the raceway in which the rolling motion occurs.

The analysis of radial, thrust, and the determination of the dynamic equivalent radial load are addressed in detail in Chapter 3, Section 3.3 Dynamic equivalent radial load of the present manuscript.

### **2.1.3 Analysis of the variation of the contact angle**

Another important factor in the analysis of load distribution in rolling bearings is the contact angle. Conventionally, it has been assumed that this angle is constant. Although, this assumption simplifies the calculations, it does not consider the real elastic deformation due to the varying force acting on the rings and each ball of the bearing. In the work conducted by Neng Tung Liao et al. [35], a simplified three-dimensional model for elastic deformation was introduced. Based on the model, the total force acting on the bearing, in axial and radial directions was determined based on the force balance. The mathematical model is implemented in different books and used by bearing manufacturers for the determination of the basic equivalent radial load, and this work uses this model as well. It is important to remark that one of the disadvantages in the model is that for the derivation of the contact angle, thermal effects due to lubrication were neglected.

In spindle units, angular contact ball bearings with relatively large magnitude are implemented due to their capacity to absorb axial loads (thrust loads). However, if the contact angle is considerably large, the bearing will perform better under axial loads with lower rotational speeds, which are generally smaller than radial loads in spindle units. Typi-

cally, a contact angle of  $40^\circ$  is implemented in this type of systems, as illustrated in Fig. (1).

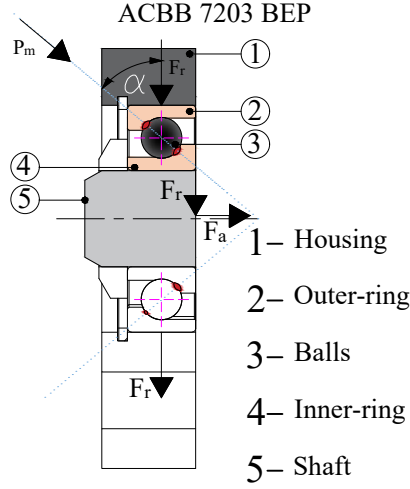


Figure 1: Contact angle of an angular contact ball bearing

The influence of the contact angle  $\alpha$ , in the determination of the Axial load  $F_a$ , radial loads  $F_r$ , and dynamic equivalent radial load  $P_m$  is addressed in detail in Chapter 3, Section 3.3 Dynamic equivalent radial load, and Section 3.4 Determination of the rolling contact of the present manuscript.

## 2.2 Frictional moments in angular contact ball bearings of spindle units

Although angular contact ball bearings are considered non-frictional elements, the exerted forces over the rolling elements under machining operations produce friction. The frictional effect in rolling bearings is essential to carrying the load from the spindle, and to convert the sliding contact of the raceways and rolling elements in rotational movement. The excess of friction would have negative effects on the rolling elements, including generation of heat, thermal expansion, radial displacement of the inner- and outer-ring of the bearing, wear and reduction of service life. The formulation of exact solutions for the determination of the frictional moments in rolling bearings is not possible due to the complexity of the bearing structure and the several factors influencing friction. An empirical solution given in Eq. (1) was proposed by Palgrem A. [36], which until now serves as the model foundations for the different frictional models in rolling bearings. The model relates the effects of lubrication viscosity, loading direction, the coefficient of rolling friction, the friction coefficient due to loading, the geometry of the angular contact

ball bearing, and the force. Equation (1) is empirical and is presented below as function of the moving elements of the spindle bearing arrangement, inner-ring and balls. This function is adaptable and depending on the application, this configuration may vary.

$$M_f = 0.8 \cdot f_o \cdot (\mu_o \cdot)^{2/3} \cdot (r_i + r_b)^3 + \mu_1 \cdot f_1 \cdot (P_m) \cdot (r_i + r_b) \quad (1)$$

It is important to determine and establish the types of friction torque that angular contact ball bearings in spindles undergo during machining operations and the effect that the different types of friction produce on the angular contact ball bearings of spindle units. While the rolling elements move over the raceway, the material in the forward position of the contact area undergoes compression, and the material in the rear position releases stress. This type of friction is called elastic hysteresis [37], and it is very small in comparison to other types of friction. In the majority of cases is neglected in the calculations. The first important type of friction in the thermal analysis is the sliding friction, which occurs between the inner- and outer-ring of the bearing and the balls. The linear velocity of the inner-ring is proportional to the distance of the bearing axis, likewise the linear velocity of the balls is proportional to the distance of their own axis. The difference between the linear velocities produces the sliding effect of the elements [37]. This effect is called differential sliding friction torque. There are many other types of sliding friction inside the rolling bearing, including sliding between the cage and the ring, balls and cage, balls and the inner-ring edge. All of them together compose the total sliding frictional moment.

The second relevant type of friction is rolling friction, which is influenced by elastohydrodynamic lubrication. A hydrodynamic film forms between the rings of the bearing and the rolling elements, which varies relative to the speed. Only a small amount of lubricant passes through the contact area; the rest of the lubricant produces a reverse flow, resulting in rolling friction [37].

The spinning friction is directly proportional to the 3/4 of the contact load and occurs due to the rotation of the balls around the normal direction of the contact surface [38]. Having established the different types of friction that angular contact ball bearings undergo during machining operations, various theoretical models have been developed. M. R. Lovell et al. [39], developed a three-dimensional FEM model to simulate frictional properties. Their findings show that for ceramic balls the stresses in the normal directions are higher than in steel balls. The maximum stress in the normal direction is

significantly less in coated surfaces than in uncoated. As described in their work, through the FEM model, they could characterize the effect of friction of different types of balls with coated and uncoated surfaces.

Considering the lack of information, C. R. Gentle et al. [40], conducted simulations to study the effects of drag forces in an angular contact ball bearing due to viscous friction of the balls and the cage. The validation of the simulations was performed using theoretical expressions for predicting friction showing good agreement. This work ensures the capacity of using computational tools to simplify the frictional modeling. Based on the comparisons performed with theoretical models, it can be seen that these methodologies lead to accurate results in the determination of frictional moments.

To simplify the determination of frictional moments, Kosmol Jan [41], proposed a fast method to compute frictional coefficients based on the assumption that friction coefficients will be proportional to the semi-minor axis  $b$  of the ellipse contact zone, which is found using Hertz contact theory. Analytical models have been studied by Heras I. et al. [42], using a FEM model. Through their validation, the analytical models proved to be accurate for sliding and rolling friction. In the case of spinning, the analytical models are satisfactory when the stick region is very small as in the case of the contact zone between the races and the balls. This analysis can be applied where large tilting moments are not involved.

In spindle systems, angle misalignment in the angular contact ball bearings is unavoidable, mainly resulting from the elastic deformations of the shaft and the housing. Another factor contributing to misalignment in angular contact ball bearings is the assembly errors during installation of the bearings onto the shaft. Van Canh Tong et al. [43] investigated the effects of misalignment on frictional behavior in angular contact ball bearings preloaded using constant force and constant displacement methods. The frictional torque was obtained for each individual ball reflecting the influence in the increase of the elastohydrodynamic lubrication rolling resistance and spinning friction.

Experimental methods to determine the frictional moments in bearing of spindle units might not be preferred due to the extensive cost of the experimental setup. Cousseau T. et al. [44] describe procedures developed for testing frictional moments on a four-ball machine. Their findings correlate the bearing friction with the generation of heat. The measurements were taken by thermocouples and a torque sensor for precise measurement. As described, implementing a testing rig presents difficulties in instrumentation installa-

tion. While the method is reliable, the costs are high if this analysis were to be performed on a spindle unit.

Bearing manufacturers have developed their own frictional calculation methods. These methods can be simply divided into bearing-based global methods, as developed by SKF (Svenska Kugellagerfabriken), or Schaeffler, and contact-based local methods, as developed by Schleich. The first method is based on Palgrem's empirical formulation, which divides the frictional torques in load-dependent and non-load dependent. For contact-based calculations, the frictional torque is divided into several components, including frictional torque irreversible deformation, rolling frictional torque, sliding frictional torque, frictional torque from rib contacts, non-load frictional torque [45]. Reflecting the current state of the art in the calculations of rolling frictional torques, the contact-based local methods are preferred for accurate calculations.

The determination of the rolling frictional moment  $M_{rr}$ , sliding frictional moment  $M_{sl}$ , and total frictional moment  $M_f$ , is detailed in Chapter 3, Section 3.4 Determination of the rolling contact, Section 3.5 Determination of the fluid film parameters, and Section 3.7 Determination of the frictional moments of the present manuscript.

### **2.3 Hertzian contact in rolling contact between two bodies**

The precision of a thermal model in the angular contact ball bearings will depend on the correct calculation of the contact region between the inner-ring and balls, and outer-ring and balls. According to Hertz classical theory, the contact area between two spherical or cylindrical elastic bodies under pressure has the shape of an ellipse [46], [47]. The pressure distribution will be represented by a semi-ellipsoid projected over the contact area. The contact area is a function of the normal deformation and the contact load at the center of the ellipse. Two types of contact were established by Hertz, line and point contact. According to Luc Houpert [47], there is no simple relationship for calculating the normal force as a function of the normal deformation for line contact. In his studies mathematical formulations to determine the normal deformation were derived for inner-ring and roller contact, outer-ring and roller contact. Subsequently, the contact load was derived. This type of contact is not applicable in angular contact ball bearings, where the contact is described by discrete points on the surface of the inner-ring and outer-ring. To describe the contact phenomena in angular contact ball bearings, the point contact is the adequate approach. Through this assumption the semi-major axis  $a$  and semi-minor axis

$b$  of the ellipse is calculated by the geometrical characteristics, the material properties of the elements of the bearing and the basic equivalent radial load acting on the center point of the ellipse contact. The theory of hertzian contact is applied only under the assumption that there is no misalignment between the contacting surfaces. When the pressure distribution is not symmetrical due to misalignment, it cannot be described by the Hertzian contact theory [48], [49]. The elliptical contact formed between the inner-ring and the balls, and outer-ring and balls due to the external loads are detailed in Chapter 3, Section 3.4 of the present manuscript.

#### **2.4 Lubrication film between the rings and the balls of the angular contact ball bearing**

To ensure less friction, the reduction of wear, and the appropriate performance of the angular contact ball bearings, a film lubricant must separate the inner components of the bearing. Sliding of the balls through the races of the bearing under heavily stressed load-carrying contact is only possible when a tiny lubricant film is developed between the inner-ring and balls and outer-ring and balls of the bearing [50]. Two types of lubricants are the most commonly used in rolling bearings, grease and oil. Grease lubrication is more common than oil, and covers about 80 % of lubrication in rolling bearings [51]. However, angular contact ball bearings are mainly lubricated by oil or a combination of oil-grease. This difference, naturally will cause different effects due to heat generation and dissipation. In general, the selection of thickener and base oil type is based on the operating temperatures, slip rates, kinematic viscosity and the exerted load [52]. Special attention must be given to the lubricant viscosity, which under the influence of elastohydrodynamic lubrication (EHL) produced under high pressure will result in considerable variations of its value. Analytical models to determine EHL traction behaviors are not well established until now with regards to rolling bearings in spindle units. The most common approach is to consider the contact as an average zone with constant film thickness [53]. The oil-film lubrication in the thermal models of the angular contact ball bearings is characterized by the kinematic viscosity, which is a function of the temperature of the lubricant, and is crucial in the determination of the frictional moments, the heat generation, and the heat transfer by convection. It has been analytically described by different viscosity-temperature models including, Reynolds, Slotte Sun, Vasquez, Eyring, Walther, Vogel [54]. Generally, the Vogel approach has been commonly implemented to

determine the kinematic viscosity in various investigations and in the industrial field. This approach, in fact leads to reliable approximations within the operational conditions of a bearing in a spindle unit, i.e., temperatures in the range of 50–125 °C [55]. However, under operational conditions of the bearings in the spindle unit, it has been seen that the Walther’s viscosity-temperature model is more accurate within ranges between 25–80 °C, which is an estimated average operating temperature of bearings in spindle units [56]. The application and calculation of the Vogel, and Walther approach are described in detail in Chapter 3, Section 3.5 Determination of the fluid film parameters, of the present manuscript.

## 2.5 Heat generation analysis in rolling bearings of spindle systems

It has been stated that the assembly geometry of the angular contact ball bearings of the spindle unit, the geometrical conditions, the exerted forces under rotational speeds during machining operations, and the contact between the inner components of the bearing are the contributing factors for the frictional torque between the inner components of the bearing. Furthermore, it was stated that the lubricant alters the frictional torque. Heat is generated in the bearing due to friction, which is a tribological feature, and it is reflected on the increase of the temperature in the bearings and the other mechanisms of the spindle unit [57]. In solid bodies where there are variations in temperature, heat flow moves from regions of higher temperature to regions of lower temperature, in accordance to the Second Law of Thermodynamics. The heat transfer of energy is governed by both the conservation of energy (First law of Thermodynamics), and constitutive laws, including Fourier’s Law of heat transfer, which describe the material-dependent nature of heat conduction. The energy equation in general form and independent of the coordinate system is given in Eq. (2) [58], [59].

$$-\nabla \cdot \mathbf{q} + g(\mathbf{r}, t) = \rho c \frac{\partial T}{\partial t}, \quad (2)$$

where  $-\nabla \cdot \mathbf{q}$ , represents the divergence of heat flux,  $g(\mathbf{r}, t)$ , represents the rate of energy generation, and  $\rho c \frac{\partial T}{\partial t}$ , represents the rate of energy storage.

Two types of heat transfer mechanism occur within the angular contact ball bearing: conduction and convection. To apply heat transfer theory, first, it is necessary to assume that the rolling bearings are homogeneous, isotropic components defined at macroscale level.

Similarly, the surroundings of the bearings (shaft, retainer, housing, seals, lubricants, environmental surroundings) are also homogeneous and isotropic [58], [59]. Conduction occurs due to the contact of the surfaces of the inner-ring and balls, outer-ring and balls, inner-ring and shaft, outer-ring and housing. This type of heat transfer mechanism is described by the Fourier's law of heat. Convection takes place among the inner components of the bearing—inner-ring, balls, and outer-ring—and the lubricant. Within the spindle system, convection occurs due to the surface contact of the housing and the surrounding environment. In spindle units, it is preferable to describe convection using Newton's law of cooling.

Radiation is not considered in the heat transfer analysis of rolling bearings in spindle units, as bearings operate under conditions where conduction and convection are the dominant heat transfer mechanisms, dissipating heat more effectively. Furthermore, radiation is proportional to the surface area and the material's emissivity. Bearings have small surface areas, which emit negligible radiative heat. Another important aspect to consider is that heat transfer by radiation becomes significant at high temperatures ( $Q_{rad} \propto T^4$ ). In the case of rolling bearings of spindle units, temperatures do not exceed 125°C, [55].

Solutions of the energy equation Eq. (2), by analytical methodologies are complex. The majority of proposed solutions deal with simple geometries such as plates, cylinders, spheres among others. Furthermore, only 1-D and 2-D solutions are solvable, if the boundary and initial conditions are mathematically given as well. The boundary conditions are classified as follows: no physical boundary (ideal case), prescribed temperature (more accurate and practical method), prescribed heat flux (for applications where heat flux can be measured), convective condition, thin film with no convection and thin film with convection [59], [60]. Another solution method are the numerical approaches, which provide approximate solutions of the heat equation through computational interactions [61].

### 2.5.1 Heat partitioning

The generation of heat in the development of thermal models in angular contact bearings of spindles can be determined by two approaches. In the first approach, heat generation is assumed to be concentrated in a single element [62]. This approach simplifies the determination of the heat flow distribution in most cases, assuming that the only heat-

generating elements are the balls or the bearing itself. The second approach is called heat partitioning. A. Clarke et al. [63] studied the problems emerging from heat partitioning in lubricated rolling and sliding contact by performing experiments on two disks. Their analysis involved various partitioning methods, which consider the surfaces of the disks as one heat source and the lubricant film between the disks as another heat source. Experimental measurements were used to compare the proportionality of heat generation from each source. This methodology can also be applied in rolling bearings, with the selection of heat sources based on the description of the thermal phenomena. Evans H. et al. [64] conducted further studies involving heat partition experiments and frictional resistance. They measured the temperature distribution and calculated the heat flux. This methodology is valid for the analysis of rolling bearings, in which heat can be divided between the balls, the inner-ring and the outer-ring. The conceptualization is determined and calculated in Chapter 3, Section 3.8 Determination of the heat generation of the present manuscript.

## **2.6 Thermal models for rolling bearings based on FEM and CFD simulations**

Until now, none of the theoretical models have been able to precisely predict the thermal fields in spindle units and their rolling bearings. Moreover, determining the boundary and initial conditions requires extensive mathematical knowledge and the use of acceptable assumptions to simplify the determination of solutions. As a result, many researchers have turned to finite element methods (FEM) and computational fluid dynamics (CFD) solutions to analyze the thermal fields in spindle units and bearings. FEM analysis aids in solving complex 3-D geometries, treating the spindle unit as a holistic structure [65]. This approach is popular due to the availability of FEM software, which offers accurate solutions. FEM simulations can provide solutions in steady and transient state conditions, often used to evaluate experimental solutions or develop thermal networks [66]. However, the implementation of Finite Element Analysis can be costly for developing thermal models in rolling bearings [57]. Significant contributions have been made by researchers such as L. Q. Wang et al. [67], who developed a computational model based on ANSYS to evaluate the operating temperatures of high-speed ball bearings. This model, based on frictional heating, determines heat generation and transient temperature. The study revealed that heat generated due to differential motion in the outer ring is the largest heat source as rotational speed increases. Additionally, the curvature coefficient of the

inner ring significantly affects heat generation. In another study by Wenjun Gao et al. [68], a computational fluid dynamic method was developed to predict churning losses in cylindrical roller bearings. This method considers a configuration of multiple in-line finite length circular cylinders packed between two flat surfaces. The analysis showed the impact of churning moments dependent on the orbital speed and the adjacent rollers inside the bearing. A formulation was proposed for predicting losses in cylindrical roller bearings for high-speed applications, where 50 % of the power losses are dissipated due to churning effects. Numerical simulations by Jingyu Zhao et al. [69] for oil film motion in bearing chambers demonstrate the relevance of FEM and CFD solutions in analyzing thermal fields. Their model, based on theoretical three-dimensional unsteady oil film motion, predicts characteristics such as oil film thickness, velocity, and temperature with rotational speed and lubricating oil flow. The simulations provide solutions for complex configurations, including the analysis of drag forces generated in the bearing cavity with finite length elements during high-speed motion, and predicting flow patterns around spheres and drag coefficients when adjacent balls are in the nearest zones [70], [71]. While FEM (Finite Element Simulations), and CFD (Computational Fluid Dynamics) solutions are valuable for analyzing thermal fields, it's important to note their costliness, especially for specific characteristics in rolling bearings.

## **2.7 Thermal resistance networks for rolling bearings in spindle units**

Generally, the objective of establishing an adequate thermal resistance network is to achieve the highest level of accuracy. The development of a thermal resistance network is founded on thermodynamics and heat transfer laws [15], [58]. The theory of heat transfer law delineates the mechanisms of heat flow, primarily described by differential equations along with initial and boundary conditions.

In the study conducted by Kovács Endre et al. [109], the system equivalence of four different phenomena: heat conduction, diffusion, flow of fluids through porous media, and the flow of electrons (electrical systems), were analyzed. The analogy of a system means that, although each physical phenomena is different, mathematically they are indistinguishable from each other [109].

A thermal system is said to be analogous to an electrical system, as both systems are governed by similar equations [72], [73]. The behavior of one system can be translated into equations for other simply by substituting the symbols of the variables. The variables

of a thermal system analogous to the electrical system are listed in Table 1.

Table 1: Analogy between electrical systems and thermal systems

Electrical system	Thermal system
Current $I$ (A)	Heat flow $Q$ (W)
Voltage $V$ (V)	Temperature difference $T$ (°C)
length of conductor $l$ (mm)	length of path $l$ (mm)
Electrical conductivity $\sigma$ ( $\frac{S}{m}$ )	Thermal conductivity $k$ ( $\frac{W}{mK}$ )
Electrical resistance $R$ (ohm)	Thermal resistance $R$ ( $\frac{K}{W}$ )
Electrical capacitance $C$	Thermal capacitance $C_h$
Current density $J$ ( $\frac{A}{m^2}$ )	Heat flow density $\dot{Q}$ ( $\frac{W}{m^2}$ )

To implement a thermal resistance network in an angular contact ball bearing of a spindle unit, it is necessary to conceive this element as a system that can be subdivided into finite sub-volumes called nodes. Each of the nodes comprising the thermal network of the bearing is effective if it can be described mathematically by numerical techniques. This implies that its thermal properties, thermal potential, heat flow, and thermal capacitance can be expressed by equations. The appropriate design of a thermal network depends on several factors including the desired accuracy, the placement of the measurement points, the expected temperature distribution, the ease of solving the equations, the structural design of the components of the bearing and spindle arrangement [15]. Unlike the finite element method, where the precision and accuracy of the models depend on the element discretization, thermal networks do not depend on a fine discretization, but relies more on physical reasonableness.

The creation of thermal resistance networks has been used for decades, and to the present, the methodology has been implemented in modern investigations due to the capabilities of providing accurate results in spindle systems. Thermal mappings of high-speed angular contact ball bearings have been implemented by thermal networks. These models are based on load distribution and power losses. In the investigation conducted by F. Pouly et al. [74], a thermal network consisting of 12 nodes comprising the housing, shaft, lubricant space, and bearings was developed. The model showed the sensitivity of the bearing temperature distribution to the location of the heat sources, the percentage of heat vary from 70 to 100 %, depending purely on the way on how the power losses are simulated.

K. Yan et al. [61] proposed three thermal models, a three-node model, a five-node model

and a seven-node model to investigate the heat distribution in the bearings in spindle units. Several comparisons were taken with experimental data of the temperature varying with respect to the rotational speed. It could be seen that the seven-node model approximates more to the experimental solutions. However, the results do not show the exactness of the model. Nevertheless, the comparison provides information about the features of the thermal networks implemented on their investigation that could be implemented in further analysis.

Yang L. et al. [75] developed a 32-node thermal network for a motorized spindle system with cooling system. The model provides solutions in steady and transient state. An important characteristic of this model was that the bearings were considered as heat sources along with the power losses generated by the motor. The heat distribution was based on the heat transfer theory assuming layered cylindrical shape for the components of the spindle system. Experimental measurements were conducted to validate the model. The model demonstrates that the response in the transient state is swift. In most of their experiments, the system reaches steady-state conditions in less than 60 seconds.

Kai Li et al. [76] created a thermal network to analyze the maximum temperature rise in a hollow cylinder based on the 2-D heat conduction equation. The results were applied for the analysis of electrical motors. This analysis is also applicable to rolling bearings, as both elements are based on cylindrical geometries. The study is relevant for more advanced thermal networks, considering that they implemented Mellor's formulation in their analysis. This allowed for the analysis and calculation of heat flow in both radial and axial directions. The low-order lumped parameter thermal network they utilized maintains an advantage in determining the maximum temperature rise of a hollow cylinder geometry. In the investigation conducted by Changjiang Zhou et al. [77], a thermal network for a motorized spindle system has been created, in which a new methodology of solving the bearing heat is presented. In their model, two methods for the thermal networks are conceived: global and local. The global method comprises the analysis of the complete motorized spindle, while the local comprises specifically a detailed thermal network for the bearing and its surroundings. The model describes specific formulations for determining thermal resistances for each component, involving axial and radial heat flow. However, it was observed that no specific formulation is provided for the contact of moving surfaces. The results were compared with experimental measurements showing a decrease of the relative error about 9.56 % and 3.44 % in comparison to previous

models where the thermal-mechanical coupling effect was omitted. The importance of analyzing vibrations as a factor in heat generation was addressed by Dexing Zheng et al. [78]. Their research dealt with investigating the energy exchange in vibration of angular contact ball bearings, aiming to simplify the bearing-shaft system to a forced vibration model. Subsequently, the vibration heat induced was determined and introduced into the system as a heat loss. The researchers modelled a thermal network and validated the results experimentally, showing improvements in the heat generation model, the thermal characteristics, and operating accuracy. The thermal network did not consider the implementation of static, moving, or combined heat sources. However, the results showed good agreement with the experimental results. To improve accuracy in thermal networks, the solid joints and the change of heat generation was studied by Xu min et al. [79]. In their study, a model including the thermal contact resistance at solid joints based on a fractal model was introduced. In their model it is possible to analyze the heat generation per second (heat rate). The consideration of the solid joints as a thermal resistance provided contact conductance coefficients for the inner-ring and shaft, and outer-ring and housing (bearing support). The contact conductance coefficients at the joints will be implemented in this work in the development of the thermal networks.

Another relevant aspect that has been studied is the uneven distribution of radial loads, which can cause variations in the thermal effects in rolling bearings. The study conducted by Yanfei Zhang et al. [80] analyzed the heat distribution considering non-uniform preload. In their study, the preload of the bearings was controlled by three piezoelectric actuators attached to the outer-ring of the bearing. Following the principle of space force transformation, a non-uniform preload will be equivalent to a principal vector. The principal frictional moment will depend on this principal vector of force. This study is relevant to consider for simplifying load distribution calculations, which will be established in the following sections of this study as the basic equivalent radial load. The force will be one of the input factors of the thermal resistance networks. Some researchers have pursued the creation of simplified thermo-mechanical models for rolling bearings. The aim is to obtain lumped information of the components of the bearing with a minimum input data. In the studies conducted by Niel D. et al. [81], only the external geometry was used to analyze the thermal behavior of the rolling bearings as an input variable. The intermediate thermal resistance network was developed for an angular contact ball bearing under oil jet lubrication for high-speed applications. The simplified thermal network

was composed of four nodes. A significant contribution to the development of thermal networks in rolling bearings for high-speed applications was the implementation of thermal resistances of striction based on the flash temperature concept introduced by Blok H. [82].

An important development in the creation of thermal networks is the determination of heat caused by internal loads. The study conducted by Chao J. et al. [83] presented an analytical approach to calculate the heat generation rate of the supporting bearings specifically for machine tools, analyzing the internal force distribution on the bearing. The formulations presented in their work clarify the formulations for the internal loading, which depend on the variations of rotational speed, pressure, and the variation of the contact angles for both the outer and inner-ring of the bearing.

In the study performed by Jialan Liu et al. [84], the thermal structure interaction characteristics of the bearings of the spindle units was studied, and a close-loop iterative modelling method of thermal characteristics was proposed. The aim was to modify the heat sources and the thermal boundary conditions. A geometrical-mechanical thermal model based on thermal contact resistances was created characterizing the rough surface morphology of the elements establishing the multiscale contact mechanics of joint surfaces. The model accuracy was higher than 90 % in comparison to the transient analysis which had an accuracy of 80 %. The thermal contact resistances between the inner-ring and balls, and outer-ring and balls were considered static and determined by the shape and size of the Hertz contact surface.

Constriction is another significant aspect to be analyzed in the development of thermal networks. The term thermal constriction refers to the narrow paths that are formed between two surfaces in contact through which heat flows. The constriction will be understood as the thermal resistance that is formed between two bodies in contact that are joined by a very tiny surface. In the majority of cases, its value has been calculated as functions of the geometrical, mechanical and thermal characteristics. Initial models were proposed by Kek-Kiong T. et al. [85], using spatially periodic arrangements of circular disks on the surface of a semi-infinite solid. The analysis was performed for three types of boundary conditions: uniform flux, isothermal flux, and isothermal disks. From the three approximations, the authors claimed that the case of isothermal contact provides the best description solution. An improvement of the solution was proposed by Laraqi N. et al. [86] for solids with randomly sized and located contacts. The solution can be

adapted to Hertzian contacts, which can be implemented in the determination of thermal contact resistances of rolling bearings. The solution is simpler to implement and allows numerous contacts.

The implementation and the determination of the thermal contact resistances for cylindrical components, Mellor thermal network, and thermal resistances for static, moving, and combined heat sources are described in detail in Chapter 3, Section 3.9 Thermal contact resistances of the present manuscript.

### **2.7.1 Methods of solution of the system of equations describing thermal resistance models**

Not only is the determination of thermal contact resistances implemented in thermal networks of consideration, but the methods of solutions that can also be used to minimize the calculations and computation. The most traditional methods implemented in heat transfer are discrete approximations of derivatives. Two approaches are commonly used: the Taylor series expansion and the use of control volumes, which are referenced as finite difference methods. Apparently, the methods of solution are seemingly simple. However, the difficulty of the set of algebraic equations depends on the character of the differential equation, that is whether they are parabolic, elliptic or hyperbolic [87], [88]. Furthermore, the solutions can be more complicated to solve depending on whether they are analyzed as steady or transient states, where models are represented by partial differential equations. Depending on the thermal network model, the finite difference method might not be commendable in the determination of the solutions of the system of differential equations due to the complexity of the solutions. Another approach used in the solutions of heat transfer problems is the combination of finite element methods and finite difference solutions. Support for this approach is the study conducted by Chi Ma et al. [89], in which a FEA model was proposed to analyze transient thermal-structure analysis in a high-speed spindle system. The model considered thermal contact resistances at solid joints. The model predicted the fractal parameters, the thermal errors, and heat power losses. The paper describes methods of solution including Newton-Raphson to compute heat generation, M-T fractal models were implemented in the thermal contact resistances, and the W-M function was used to characterize the rough surface morphologies.

### 2.7.2 Steady-space approach and Euler's method

Throughout my investigation, I have observed that finite difference approaches might be difficult to implement in determining solutions for the thermal models of angular contact ball bearings in spindle systems due to the complexity of the thermal networks. Therefore, two approaches are proposed. One new approach utilizes the steady-state method to determine steady-state solutions. Transient-state solutions for the thermal models of spindle systems were solved using the implicit Euler's method. This method is widely used in solving the heat equation. However, the steady-state approach has not been particularly applied in rolling bearings of spindle systems. The investigation conducted by Stein J. L. et al. [90] introduced the first model for dynamically estimating thermally induced pre-load. This model is applied for online monitoring of both dynamic and static induced pre-load. The system functions as a state observer and was validated through experimental measurements.

The state-space approach is a time-domain method used for modeling, analyzing, and designing control systems for multiple input and multiple output systems, as well as for nonlinear and time-variant systems [91].

For application in the angular contact ball bearings of spindle systems, the state must be defined. This depends on a set of variables, including the temperature fields of the inner components of the bearing and the surroundings, along with the state variables, which are the smallest number of states describing the complete behavior of the dynamic nature of the system. The form in which the state variables change as functions of time is thought of as a trajectory in the dimensional space.

Two types of applications can be obtained through the state-space approach: as an observer and as a controller [92]. For the purpose of estimating the temperature fields in rolling bearings of spindle units, the system will be considered as an observer.

The determination of the formulation for the State-space approach are described in Chapter 3, Section 3.10 State Space Method for monitoring thermal fields in rolling bearings of Spindle systems of the present manuscript.

## 2.8 Conclusion of the chapter

The chapter provides a comprehensive overview of the most important factors necessary for developing thermal models in rolling bearings of spindle units. To begin with, the importance of the bearing arrangement is discussed, explaining why the back-to-back DB bearing arrangement is implemented in these units. Following this, the types of loads and their effects are analyzed, citing previous investigations that detail the types of loads and methods to calculate axial, radial, and preload in both axial and radial directions. In my dissertation, the determination of the basic equivalent radial load is considered to account for the effects of axial and radial loads. Next, the contact angle is examined to establish that this angle is not constant but can vary according to the rotational speed and the applied forces during machining operations. The frictional moments that occur as functions of rotational speed, type of lubrication, and loads are also investigated, providing mathematical formulations for analyzing different types of frictional moments. My investigation considers two main types of frictional moments: sliding and rolling friction, as these are the most influential in the thermal analysis of rolling bearings. To calculate the contact zones, the Hertzian contact theory is applied to rolling contacts is investigated, and relevant studies were analyzed to determine the method of calculations. The effects of lubrication were then studied. In my investigation, two methods for determining kinematic viscosity as a function of temperature variation are implemented: Vogel's and Walther's approaches. The calculations support the implementation of Walther's approach for determining kinematic viscosity. The heat generation analysis begins with the application of the conservation of energy. The types of heat transfer, including conduction and convection, are described. To enhance the calculations, my work proposes implementing the heat partitioning concept to accurately identify heat sources inside the rolling bearing. Several important studies on the development of thermal models using FEM and CFD simulations are described. This methodology was implemented in my research to validate the thermal models. Finally, the thermal resistance network for bearings in spindle units was analyzed through numerous significant studies. It was observed that no specific process for obtaining thermal networks had been implemented until now. Therefore, I propose three thermal networks, which will be described in the following chapters: the Dark Gray-Box, Light Gray-Box, and White Box lumped parameter thermal networks [16]. The investigations revealed that very few applications have utilized the concept of thermal contact resistances for stationary, moving, and combined heat sources.

Therefore, in the development of thermal networks for rolling bearings in spindle units, I implement the thermal contact resistances of elliptical contact for stationary, moving, and combined heat sources, based on the investigation by Y. S. Muzychka et al. [93]. Furthermore, Mellor's formulation is used in my investigation to obtain simple solutions that combine axial and radial heat flow in the inner and outer rings of the bearing [94], [95]. Finally, a new approach to obtain solutions in both steady and transient states for rolling bearings in spindle units is proposed, based on the state-space method. In general, the literature review presented in this chapter reveals valuable insights for creating new thermal models that are more accurate and can be applied to various applications with similar conditions.

## 3 Methodology of Study

The present chapter describes the methodology applied for the development of the thermal models: Dark Gray-Box, Light Gray-Box, and White Box Lumped parameter thermal networks (LPTN). All the necessary concepts for the creation of the thermal models including, type of bearing arrangement, external and internal parameters, the rolling contact analysis, the frictional model, the heat generation, the thermal contact resistances, and the methods of solution are extensively analyzed to develop the new lumped parameter thermal models.

### 3.1 Thermal analysis of rolling bearings in spindle units

The block diagram depicted in Fig. 2, shows the stages in a general overview for the development of the thermal models. To begin with, the type of bearing arrangement used in spindle units is presented. The same arrangement is implemented in the representative model for the validation of the thermal models. Following that, the external and internal factors influencing the thermal behavior are described. These factors include external loads, lubrication type, and operational speeds. Then, the rolling contact analysis must be performed based on the Hertzian contact theory for elliptic contact. The external and internal parameters along with the rolling contact analysis are foundation for the determination of the sliding frictional moment  $M_{sl}$  and rolling friction  $M_{rr}$ , which determine the total frictional moment  $M_f$ . Following this analysis, the heat generation is calculated. As explained in Section 2.5.1, the heat partition concept is implemented to determine the heat generation in the outer-ring  $\dot{Q}_o$ , the balls  $\dot{Q}_b$ , and the inner-ring  $\dot{Q}_i$ , of the bearing; and the heat distribution is analyzed based on the heat transfer laws. The thermal contact resistances for static, moving and combined heat sources, along with the axial and radial flow analysis are determined in the following stage. Finally, these factors, along with the heat generation and the thermal characteristics of the rolling bearing

components, are implemented in the new lumped parameter thermal models. For solving the system of differential equations, the new proposal based on the state-space approach is given, calculating the heat distribution in steady and transient state. Euler's method is implemented to determine the continuous time dependent function of the thermal models. The final stage is the verification of the thermal models.

### 3.2 Representative model of the bearing arrangement

A representative model, which embodies the bearing arrangement in a spindle unit, is depicted in Fig. 3a. The angular contact ball bearings are used in spindle units due to their capacity to accommodate radial and axial loads at high rotational speeds [22]. Further advantages of implementing the back-to-back arrangement include the capacity to resist highest moment its ability to handle tilting loads. When the temperature increases, the radial expansion will tend to increase the pre-load of the bearings. To mitigate this effect, the axial growth allows the bearings to move. Therefore, this type of arrangement is implemented in high-temperature / high-speed applications [25]. The representative model selected in this study consists of two angular contact ball bearings, model SKF 7203BEP, mounted on a shaft with bore diameter equal to that of the bearings. The bearings are packed on a housing, which, for the experimental analysis will be loaded in the radial direction under rotational speed, emulating the basic equivalent radial load  $P_m$  produced during machining operations.

### 3.3 Dynamic equivalent radial load

During machining operations, forces are exerted by the contact between the machine tool and the workpiece. These forces are primarily absorbed by the angular contact ball bearings and are classified as axial  $F_a$  and radial loads  $F_r$  [34] (see Fig. 3b) . The magnitude of these loads varies according to the contact angle  $\alpha$ . However, it is important to note that the optimal performance of the rolling elements occurs under radial loads. This assumption is theoretical; therefore, it is necessary to mathematically analyze these loads. The combination of axial  $F_a$  and radial  $F_r$  loads is referred to as the dynamic equivalent radial load  $P_m$  [30], as given in Eq. (3).

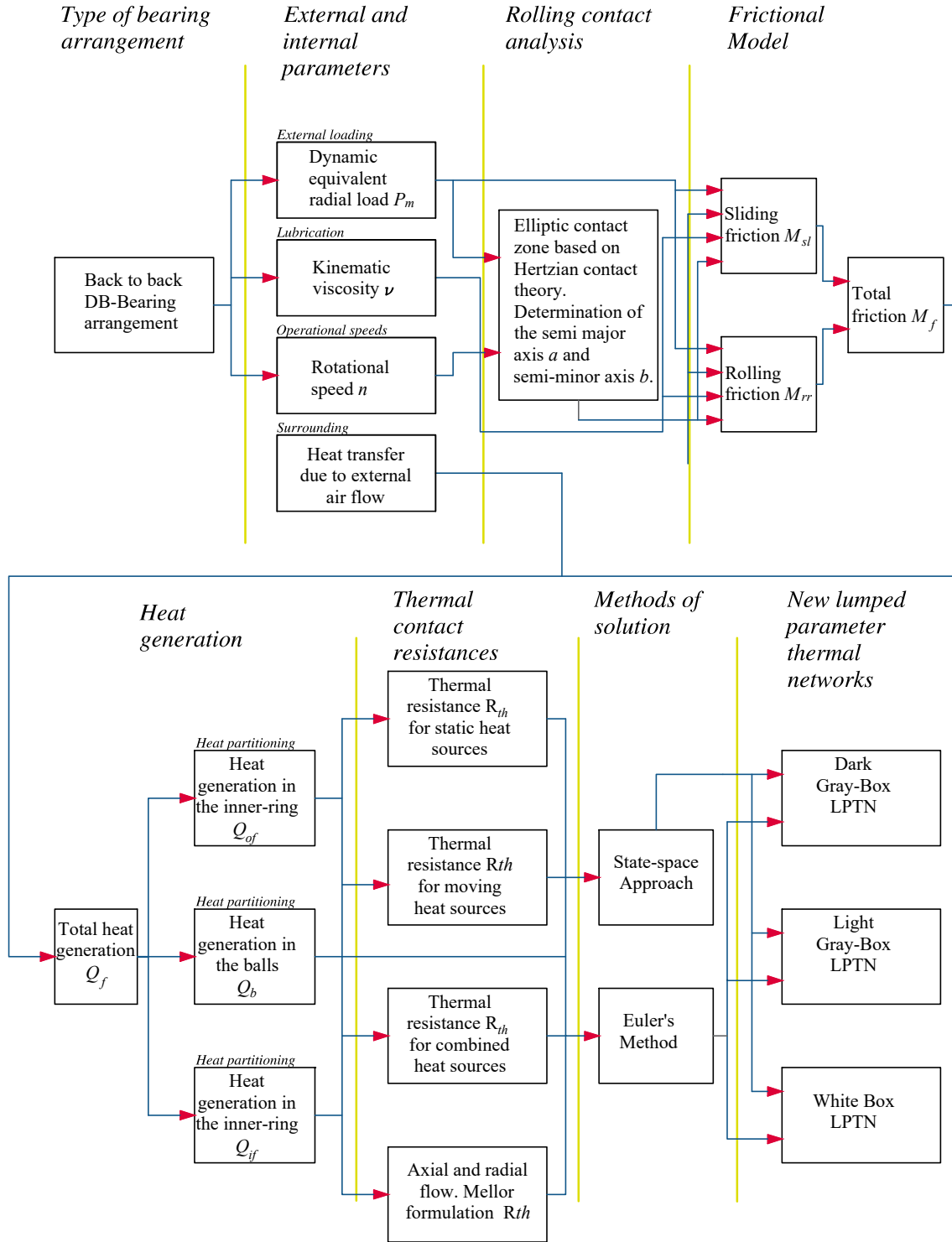


Figure 2: Block diagram of the thermal analysis of rolling bearings in spindle units

$$\begin{aligned}
 \frac{F_a}{F_r} \leq 0.505 \cdot \left( \frac{F_a}{C} \right)^{0.231} & ; P_m = F_r \\
 \frac{F_a}{F_r} > 0.505 \cdot \left( \frac{F_a}{C} \right)^{0.231} & ; P_m = 0.56 \cdot F_r + \frac{0.84 \cdot F_a}{\left( \frac{F_a}{C} \right)^{0.24}}
 \end{aligned} \tag{3}$$

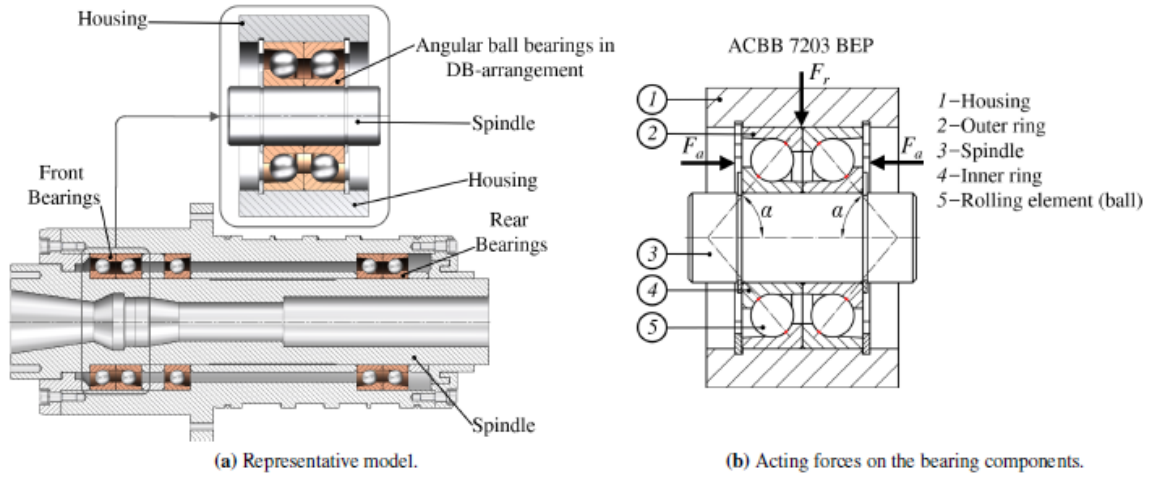


Figure 3: Bearing arrangement in a spindle unit

The dynamic equivalent radial load  $P_m$  depends on the relation between the relation axial  $F_a$  and radial  $F_r$  loads, along with the relation axial  $F_a$  and basic static load rating  $C_0$

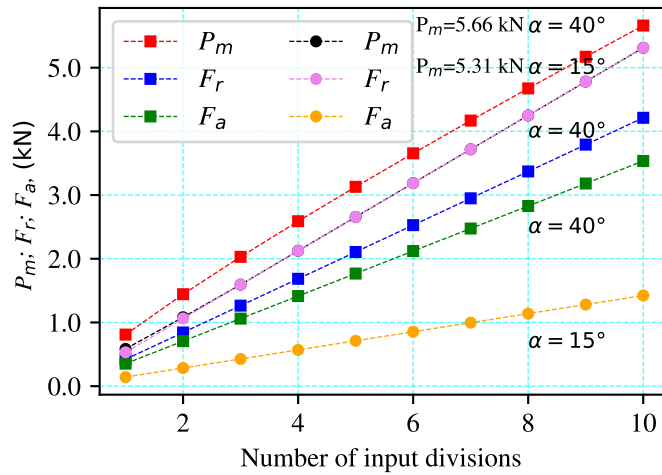


Figure 4: Variation of the dynamic equivalent load  $P_m$  as function of the contact angle  $\alpha$

The calculated maximum dynamic equivalent radial load  $P_m$  varies significantly with the contact angle  $\alpha$ . Fig. 4, compares the SKF 7203 BEP bearing with two alpha contact angles  $\alpha = 40$ , and  $\alpha = 15$ . When the contact angle is higher, the dynamic equivalent radial load  $P_m$  is higher. Nevertheless, exceeding the contact angle of  $\alpha = 40$ , will produce an increase in the axial load  $F_a$ , thus, limiting the functionality of the rolling bearing.

### 3.4 Determination of the rolling contact

In Section 2.3, it is discussed that the size and shape of the contact zone influence the heat transfer behavior in the rolling bearings [47], [48]. According to Hertzian classic theory

[95], when two elastic bodies (inner-ring and ball, or outer-ring and ball) are subjected to pressure generated by external forces, the contact area has the shape of an ellipse of semi-major axis  $a$  and semi-minor axis  $b$  as depicted in Fig. 5. The pressure distribution is represented by a semi-ellipsoid projected over the contact area, where the maximum value is given at the center of the ellipse.

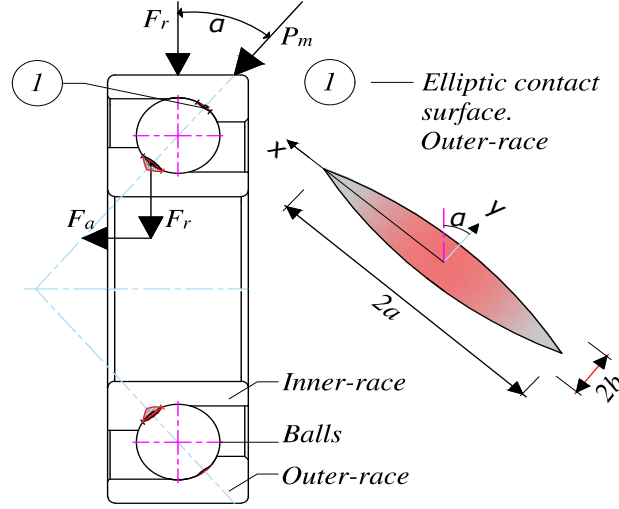


Figure 5: Semi-major axis  $a$  and semi-minor axis  $b$  of the elliptic contact zone in rolling bearings of spindle units

The semi-major axis  $a$  and semi-minor axis  $b$  determine the elliptic contact zone and are calculated for the inner-ring and outer-ring as functions of the sum of curvature radius  $\rho_{IR}$ , and  $\rho_{OR}$ , respectively, given by Eq. (4); the modulus of elasticity  $E$ , the dynamic equivalent radial load  $P_m$ , and the factors  $\xi$  and  $\eta$

$$\begin{aligned} \sum \rho_{IR} &= \frac{2}{D_w} \left( 2 + \frac{1}{\frac{D_{pw}}{D_w \cos(\alpha)} - 1} - \frac{1}{2\kappa_i} \right) \\ \sum \rho_{OR} &= \frac{2}{D_w} \left( 2 + \frac{1}{\frac{D_{pw}}{D_w \cos(\alpha)} - 1} - \frac{1}{2\kappa_o} \right) \end{aligned} \quad (4)$$

The factors  $\xi$  and  $\eta$  are calculated as functions of the ellipticity ratio  $t_r$ , and the eccentricity  $e$ , which is determined by Eq. (5), along with the complete elliptic integrals of the first kind  $K_1(e, \frac{\pi}{2})$  and second kind  $K_2(e, \frac{\pi}{2})$  [96]. The factors  $\xi$  and  $\eta$  are given in Eq. (6).

$$e = \left[ 1 - \left( \frac{b}{a} \right)^2 \right]^{1/2} \quad (5)$$

$$\xi = \left( \frac{\frac{2}{e^2} \left[ [K_1(e, \frac{\pi}{2}) - K_2(e, \frac{\pi}{2})] + \left[ \frac{K_2(e, \frac{\pi}{2})}{1-e^2} - K_1(e, \frac{\pi}{2}) \right] \right]}{\pi} \right)^{1/3}; \quad (6)$$

$$\eta = \xi \cdot (1 - e^2)^{1/2}$$

In most of the cases related to thermal analysis of rolling elements, the values for the factors  $\xi$  and  $\eta$ , are taken from plots and diagrams from the bearing manufacturers. Since the determination of the semi-major axis  $a$  and semi-minor axis  $b$  are sensitive and influence the thermal analysis, this common assumption is not considered in this research. The values are calculated and depicted as a function of the ellipticity ratio  $t_r$  in Fig. 6. The minimum divisions that can be achieved in the ellipticity ratio, enhance the accuracy of the values obtained for the semi-major axis  $a$  and semi-minor axis  $b$ .

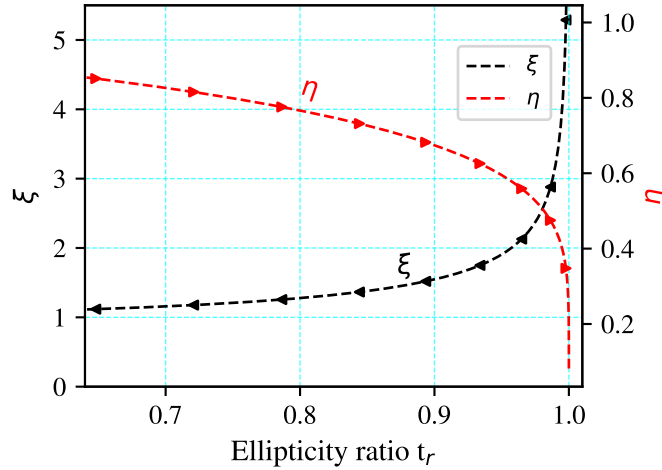


Figure 6:  $\xi$  and  $\eta$  factors as a function of the ellipticity ratio  $t_r$

The semi-major axis  $a$  and semi-minor axis  $b$  are calculated using Eq. 7.

$$a_{IR,OR} = \xi \left[ \frac{3P_m}{\left(\frac{1-v^2}{E}\right) \sum \rho_{IR,OR}} \right]^{1/3}; \quad (7)$$

$$b_{IR,OR} = \eta \left[ \frac{3P_m}{\left(\frac{1-v^2}{E}\right) \sum \rho_{IR,OR}} \right]^{1/3}$$

The pressure distribution over the elliptical contact area is calculated using Eq. (8) [31], [95]. The maximum concentration of pressure occurs at the center of the ellipse where the semi-major axis  $a$  and semi-minor axis  $b$  tend to zero. Figure 7 depicts the pressure distribution when the angular contact ball bearing is subjected to a radial force  $F_r$ , not

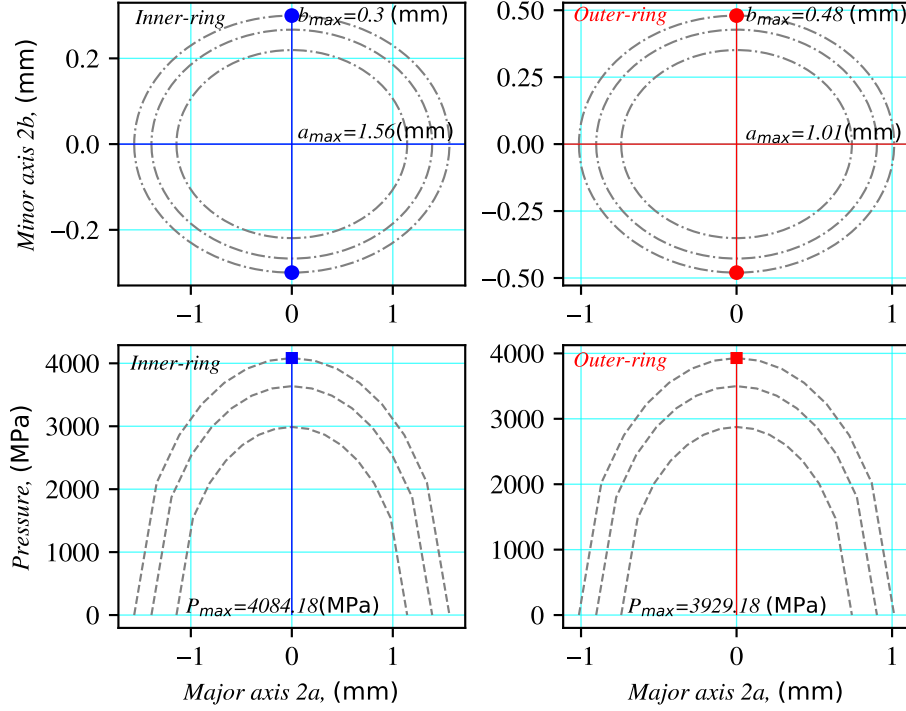


Figure 7: Semi-major axis  $a$  and Semi-minor axis  $b$  of the inner and outer ring) and pressure distribution  $P(x, y)$ .

exceeding the dynamic equivalent radial load  $P_m$  as specified by the requirements of the manufacturers of the bearing.

$$P(x, y) = P_m \left[ 1 - \left( \frac{x}{a} \right)^2 - \left( \frac{y}{b} \right)^2 \right] \quad (8)$$

The determination of the maximum pressure for the inner-ring and outer-ring of the angular contact ball bearing SKF 7203BEP, was  $P(x, y)_{max} = 4084.18$  MPa for the inner-ring and  $P(x, y)_{max} = 3929.18$  MPa for the outer-ring. This occurs when the bearing is loaded until the basic equivalent radial load  $P_m$  is reached.

### 3.5 Determination of the fluid film parameters

Two regimes can describe the tribological phenomena occurring during rotation in the bearings of a spindle system: dry sliding and fluid-film lubrication [50]. The first case represents the absence of a fluid (liquid or gas) between the rubbed surfaces (balls and rings). The practise is not commonly used in modern machinery, considering that the direct contact of the surfaces decreases the life span of the elements, and limits the heat transfer distribution along them. The second regime involves a fluid-film lubrication. In

this regime, the balls and the inner and outer-ring are separated by a tiny film, which generates a load supporting pressure by three types of actions:

- Hydrodynamic lubrication, which occurs by the self pumping action of the moving surfaces [50]. In this regime, the pressure, along with the frictional losses are functions of the lubricant viscosity.
- The squeeze film action, founded in dynamically loaded bearings in reciprocating engines. Two types of fluids are commonly used: oil and air. The squeeze film action is not a common practise in rolling bearings of spindle systems. However, it is mainly used in applications where non-contact suspension mechanisms enhance the ability of rotation in machines [97].
- External pressurized lubrication, which requires external pumping to generate pressure and recirculate the fluid into the bearing. This method is commonly implemented in heavy duty machinery at low-speed and low viscosity fluids [50].

This research focuses on the most commonly implemented systems, where a small amount of lubricant is used to generate elastohydrodynamic lubrication (EHL) [50], [51], [52]. In this regime, the pressure is large enough to cause significant elastic deformation of the surfaces. EHL lubrication is characterized by the kinematic viscosity  $\nu$  of the lubricant, which is directly influenced by the temperature variations. The oil lubricant selected in the analysis was ISO VG-32, due to its excellent thermal stability, applicability in machine tools and long oil lifetime.

### 3.5.1 Determination of the kinematic viscosity

As described in Section 2.4, two approaches can be applied to calculate the kinematic viscosity of the lubricant in the angular contact ball bearing: the Vogel and Walther approaches. To ensure accuracy, the present work uses the Walther approach, which yields more precise results for the kinematic viscosity as studied by [98]. The Vogel and Walther approaches are determined by Eq. (9) and Eq. (10), respectively.

$$\nu = \nu_{ref} \cdot \exp(-\beta (T_{lub} - T_{lref})), \quad (9)$$

where  $\beta = \frac{\ln \frac{\nu_i}{\nu_f}}{T_i - T_f}$ , depends on the kinematic viscosity of the lubricant at ambient temperatures and a maximum value of temperature  $T_f$  that for this analysis is 150°C.

$$\nu = \log \log (\nu_{lf} + 0.7) - \frac{\log \log (\nu_{lf} + 0.7) - \log \log (\nu_{li} + 0.7)}{\log \left( \frac{T_{lf}}{T_{li}} \right)} \cdot \log (T_{lf}) \quad (10)$$

Figure 8 describes the behavior of the kinematic viscosity  $\nu$  as a function of the temperature, using the Vogel and Walther approaches. Within the operational conditions, the two approaches behave similar; however, this small variation substantially influences the determination of the frictional moments, which determine the heat generation in the angular contact ball bearings.

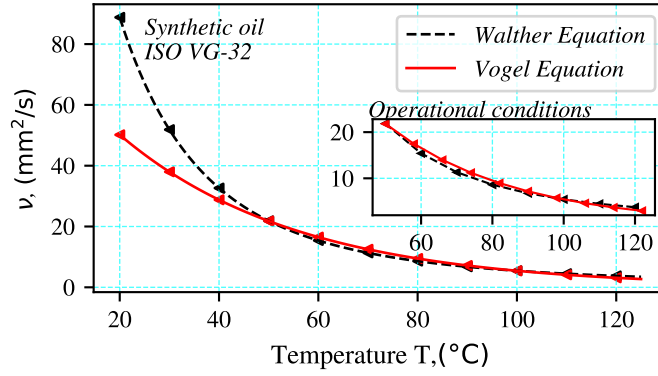


Figure 8: Kinematic viscosity  $\nu$  of the Oil lubricant ISO VG-32 as a function of the temperature.

### 3.5.2 Determination of the fluid film thickness

A minimum lubricant film thickness must be formed in order to support the loads and allow the rotating movement of the balls and rings of the bearing. The film thickness is determined as a function of three main coefficients, the dimensionless speed parameter  $U^*$ , the dimension load parameter  $W^*$  and the dimensionless material parameter  $G^*$ .

The speed parameter  $U^*$  is given by Eq. (11).

$$U_{IR,OR}^* = \frac{\nu_0 \cdot \frac{\pi \cdot n \cdot D_{pw}}{120} \cdot \left( 1 - \left( \frac{D_w \cos(\alpha)}{D_{pw}} \right)^2 \right) \cdot 10^{-3}}{E \cdot \rho_{IR,OR}} \quad (11)$$

The force parameter  $W^*$  is determined by Eq. (12).

$$W_{IR,OR}^* = \frac{P_m}{E \cdot \rho_{IR,OR}^2} \quad (12)$$

The material parameter  $G^*$  is determined by Eq. (13).

$$\begin{aligned} G^* &= 5.1 \cdot 10^{-9} \cdot Z \cdot (\ln \nu_0 + 9.67) \cdot E \\ Z &= [7.81 (H_{40} - H_{100})]^{1.5} \cdot (0.885 - 0.864 H_{40}), \end{aligned} \quad (13)$$

where  $H_{40} = \log(\log \nu_{40} + 1.2)$ , and  $H_{100} = \log(\log \nu_{100} + 1.2)$ .

The minimum oil film thickness is determined by Eq. (14)

$$H_{IR,OR} = 3.63 \cdot U_{IR,OR}^{*0.68} \cdot W_{IR,OR}^{*-0.073} \cdot G^{*0.49} \cdot \left[ 1 - \exp \left( -0.68 \cdot 1.03 \frac{b_{IR,OR}}{a_{IR,OR}} \right) \right] \quad (14)$$

The minimum fluid film thickness for the inner-ring and balls  $H_{IR}$ , and outer-ring and balls  $H_{OR}$ , is illustrated in Fig.(9), as a function of the rotational speed  $\omega$ , for different values of the basic equivalent radial load  $P_m$ . This parameter shows that a very tiny film is generated, thus, allowing the elastohydrodynamic lubrication (EHL) to occur.

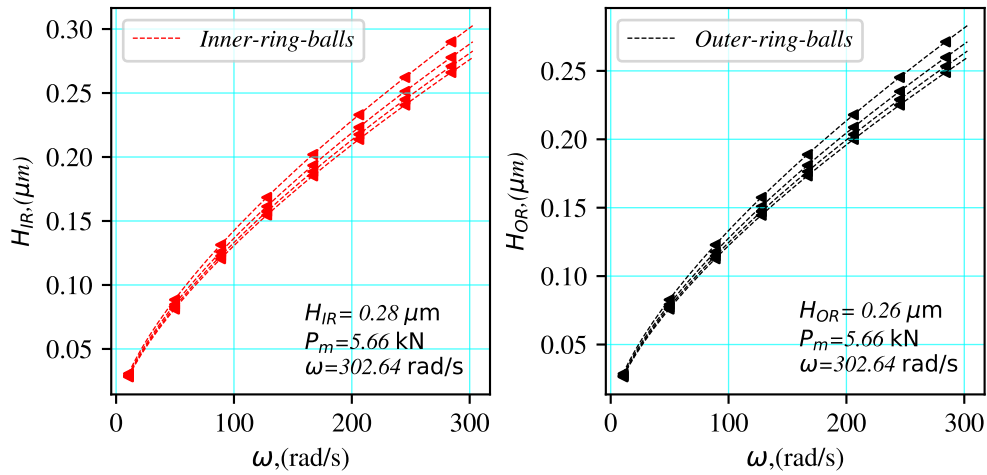


Figure 9: Minimum lubricant film thickness  $H_{IR}$ ,  $H_{OR}$ .

### 3.5.3 Determination of the convective coefficient of the lubricant film

Heat transfer by convection occurs between the oil-film and the inner-ring, the oil-film and the balls, the oil-film and the outer ring. Many investigations [3],[75],[100] have assumed that the heat convection coefficient of the oil-film  $h_{lub}$  is constant. The assumption simplifies the calculations in the thermal models; nevertheless it cannot be assumed as constant for all components, given that fluid parameters, including the Nusselt number  $Nu$  and the Reynolds number  $Re$  are direct functions of the geometry of the components of the bearing, and the angular speed  $\omega$ . To improve the accuracy of the models, we have decided to implement the method derived in [8]. The Prandtl number is determined as the ratio between the kinematic viscosity of the lubricant  $\nu$  to the thermal diffusivity of the lubricant  $\alpha_D$  and it is given in Eq. (15).

$$Pr = \frac{\nu}{\alpha_D} \quad (15)$$

The Reynolds number for the inner-ring  $Re_i$ , is determined as a function of the inner diameter of the shoulder of the bearing in the smallest front surface,  $d_2$ . The Reynolds number for the balls  $Re_b$ , is determined as a function of the ball diameter,  $D_w$ , and the Reynolds number of the outer-ring  $Re_o$ , is determined as a function of the outer-ring shoulder diameter,  $D_2$ . The three functions are given in Eq. (16).

$$\begin{aligned} Re_i &= \frac{\omega \cdot d_2}{\nu} \\ Re_b &= \frac{\omega \cdot D_w}{\nu} \\ Re_o &= \frac{\omega \cdot D_2}{\nu} \end{aligned} \quad (16)$$

The Nusselt number  $Nu_b$  of the balls was calculated using Eq. (17).

$$Nu_b = (1.2 + 0.53 \cdot Re_b^{0.64}) \cdot Pr^{0.3} \quad (17)$$

For the inner-ring and outer-ring, the Nusselt number  $Nu$  is a function of the Taylor number  $Ta$ , which is calculated using Eq. (18).

$$\begin{aligned} Ta_i &= Re_i \cdot \sqrt{\frac{2 \cdot \epsilon_r}{r_i}} \\ Ta_o &= Re_o \cdot \sqrt{\frac{2 \cdot \epsilon_r}{r_o}} \end{aligned} \quad (18)$$

Subsequently, the Nusselt number for the inner and outer-ring is obtained by Eq. (19).

$$\begin{aligned} Nu_{i,o} &= 2 & Ta_{i,o} &\leq 41 \\ Nu_{i,o} &= 0.167 \cdot Ta_{i,o}^{0.69} \cdot Pr^{0.4} & 41 &< Ta_{i,o} \leq 100 \\ Nu_{i,o} &= 0.401 \cdot Ta_{i,o}^{0.50} \cdot Pr^{0.4} & 100 &< Ta_{i,o} \end{aligned} \quad (19)$$

After determining the Nusselt numbers corresponding to each component of the rolling bearing, the heat convection coefficients for the inner-ring  $h_i$ , the balls  $h_b$ , and the outer-ring  $h_o$  are calculated using Eq. (20).

$$\begin{aligned} h_i &= \frac{k_{oil} \cdot Nu_i}{d_2} \\ h_b &= \frac{k_{oil} \cdot Nu_b}{D_w} \\ h_o &= \frac{k_{oil} \cdot Nu_o}{D_1} \end{aligned} \quad (20)$$

To enhance the predictability of the thermal models, the heat convection coefficients  $h_i$ ,  $h_b$ , and  $h_o$  are calculated for each variation in the dynamic equivalent radial load  $P_m$ , rotational speed  $\omega$ , and kinematic viscosity  $\nu$ , according to the operating temperature. Figure (10) illustrates the different values of the heat convection coefficients considering a maximum load equal to  $P_m = 5.5\text{kN}$ , under the maximum limit of angular speed  $\omega = 2100\frac{\text{rad}}{\text{s}}$ , and a kinematic viscosity equals to  $\nu = 5.43\frac{\text{mm}^2}{\text{s}}$ .

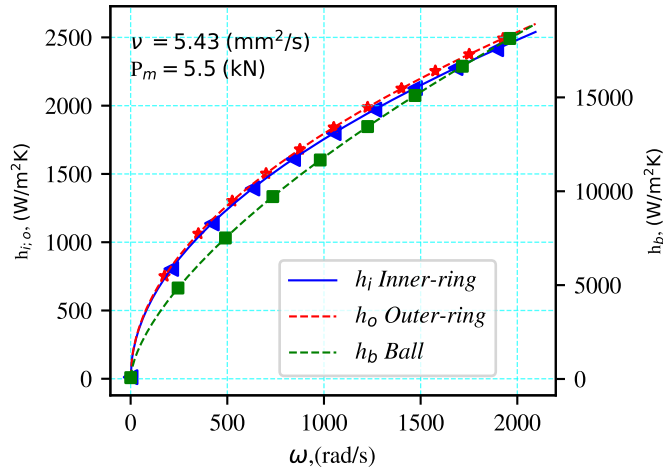


Figure 10: Heat convection coefficients  $h_i$ ,  $h_b$ , and  $h_o$

It is remarkable to observe the difference in the values of the convective coefficients of the lubricant. Specifically, the heat convection coefficients  $h_i$  for the inner-ring, and  $h_o$  for the outer-ring, do not vary noticeably. However, the heat convection coefficient of the balls  $h_b$ , is significantly larger. Therefore, assuming a constant heat convection coefficient for the creation of the thermal models may introduce errors in the calculation.

### 3.6 Convective coefficients of air surrounding the housing

The surroundings of a spindle system play an important role in heat transfer analysis. Mainly, spindles are exposed to ambient air that flows at very low speeds. Through convection, the air dissipates heat transferred from the housing. The housing absorbs heat through the angular contact ball bearings [6]. Therefore, a lumped heat capacity model can be applied to determine the heat transfer between the spindle and the surroundings. Although the external geometry of the spindle housing is complex, it can be approximated as a cylinder with an equivalent external hydraulic diameter [99]. It is assumed that machines are not exposed to significant air current flows, therefore, a low speed air

flow analysis is conducted to determine the heat transfer coefficients of air, which are crucial for the lumped parameter thermal networks. The main factor to find the heat convection coefficients for this configurations is the Nusselt number  $Nu_{air}$ . It is determined based as a function of the Reynolds number  $Re_{air}$ , and the Prandtl number  $Pr$ . The Reynolds number for the air  $Re_{air}$  was determined using Eq. (21).

$$Re_{air} = \frac{v_{air} \cdot \phi_{housing}}{\nu_{air}} \quad (21)$$

The Nusselt number of the environment  $Nu_{air}$  was obtained using three correlations given by Zukauskas, Churchill, and Hilpert [99]. The equations for the three correlations are given in Eq. (22), Eq. (23), and Eq. (24), respectively. The air velocities were considered within the range of  $v_{air} = 0.25 - 4.0 \left(\frac{m}{s}\right)$ .

$$Nu_{air} = c \cdot (Re_{air})^m \cdot (Pr_f)^{0.37} \cdot \left(\frac{Pr_f}{Pr_w}\right)^{\frac{1}{4}} \quad (22)$$

$$Nu_{air} = 0.3 + \frac{0.62 \cdot (Re_{air})^{\frac{1}{2}} \cdot (Pr_f)^{\frac{1}{3}}}{\left[1 + \left(\frac{0.4}{Pr_f}\right)^{\frac{2}{3}}\right]^{\frac{1}{4}}} \cdot \left[1 + \left(\frac{Re_{air}}{282000}\right)^{\frac{5}{8}}\right]^{\frac{4}{5}} \quad (23)$$

$$Nu_{air} = c \cdot (Re_{air})^m \cdot (Pr_f)^{\frac{1}{3}} \quad (24)$$

Figure (11) illustrates the relation between the Nusselt number  $Nu_{air}$  as a function of the Reynolds number  $Re_{air}$ . It is observed that two functions Zukauskas and Churchill tend to be similar within the range of Reynolds number  $0 \leq Re_{air} \leq 5000$ . After that, the trend is similar but the Churchill C. has lower values as compared to Zukauskas C.

The heat convection coefficient of the environment  $h_{air}$  was determined using Eq.(25) for the three correlations within the range of air flow  $v_{air} = 0.1 - 4.0 \frac{m}{s}$ . The values are given in Table 2.

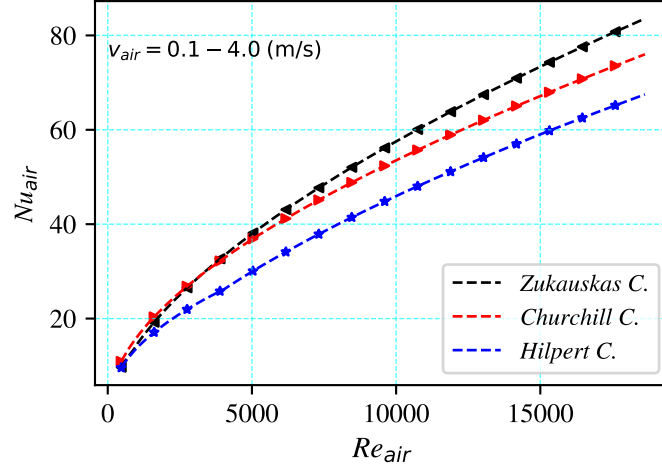


Figure 11: Nusselt number  $Nu_{air}$  as a function of the Reynolds number  $Re_{air}$  for air speeds between  $v_{air} = 0.1 - 4.0 \frac{m}{s}$ .

$$h_{air} = Nu_{air} \cdot \frac{k_{air}}{\phi_{housing}} \quad (25)$$

Table 2: Heat convection coefficients of the environment  $h_{air}$

$v_{air} \left( \frac{m}{s} \right)$	$h_{air} \left( \frac{W}{m^2K} \right)$ Zukauskas C.	$h_{air} \left( \frac{W}{m^2K} \right)$ Churchill C.	$h_{air} \left( \frac{W}{m^2K} \right)$ Hilpert C.
0.10	3.60	4.05	3.56
0.36	7.31	7.72	6.47
0.62	10.14	10.22	8.33
0.88	12.51	12.28	9.83
1.14	14.61	14.09	11.53
1.40	16.53	15.74	13.10
1.66	18.30	17.26	14.55
1.92	19.98	18.69	15.92
2.18	21.56	20.04	17.22
2.44	23.07	21.34	18.46
2.70	24.51	22.58	19.66
2.96	25.90	23.77	20.81
3.22	27.24	24.93	21.92
3.48	28.54	26.06	22.99
3.74	29.80	27.15	24.04
4.00	31.03	28.22	25.06

Figure (12) depicts the heat convection coefficient of the environment  $h_{air}$ , which will be implemented in the thermal models.

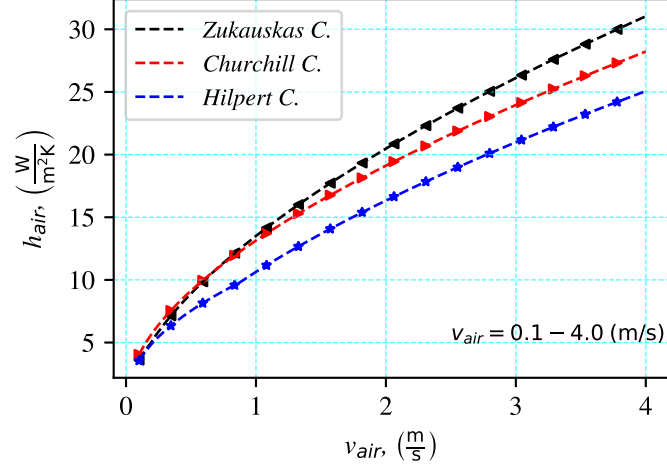


Figure 12: Convection coefficient of air  $h_{air}$  as a function of the air flow speed  $v_{air} \frac{m}{s}$ .

### 3.7 Determination of the frictional moments

Based on Palgrem's empirical model given in Eq. (1) [36], the frictional moments can be calculated. It has been discussed in the previous sections that the present investigation considers the rolling friction  $M_{rr}$  and sliding friction  $M_{sl}$  for the determination of the total frictional moment  $M_f$ . For the representative model an ACBB 7203BEP is used as sample; therefore, it can be possible to use the own formulation proposed for the determination of frictional moments. The mathematical formulation is given in Eq. (26) [101].

$$\begin{aligned}
 M_{sl} &= 1.82 \cdot 10^{-12} \cdot d_m^{0.26} \cdot \left[ (F_r + 2.44 \cdot 10^{-12} \cdot d_m^4 \cdot n^2)^{\frac{4}{3}} + 0.71 \cdot F_a^{\frac{4}{3}} \right] \cdot \mu_{sl} \\
 M_{rr} &= \Phi_{isl} \cdot \Phi_{rs} \cdot 4.33 \cdot 10^{-7} \cdot d_m^{1.97} \cdot (F_r + 2.44 \cdot 10^{-12} \cdot d_m^4 \cdot n^2 + 2.02 \cdot F_a)^{0.54} \cdot (\nu \cdot n)^{0.6} \\
 M_f &= M_{sl} + M_{rr}
 \end{aligned} \tag{26}$$

Equation (26), is an empirical function with multiple variables, including the sliding friction coefficient  $\mu_{sl}$ , the kinematic replenishment factor  $\Phi_{rs}$ , and the inlet shear heating reduction factor  $\Phi_{isl}$ . The mathematical formulations can be found in [101]. The sliding friction  $M_{sl}$  and rolling friction  $M_{rr}$  depend on the geometrical characteristics of the bearing, the axial  $F_a$  and radial forces  $F_r$ , the rotational speed  $n$  and the kinematic viscosity of the lubricant  $\nu$ . This investigation shows that a slight variation of the kinematic viscosity significantly influences the determination of the frictional moments.

The kinematic viscosity  $\nu$  influences the determination of the frictional moments. This can be observed in Figure (13), where, under loads equal to the dynamic equivalent ra-

dial load  $P_m$ , the behavior and values of the frictional moments change as the kinematic viscosity varies. Figure (13a) shows that the total frictional moment  $M_f$  is equivalent to the sliding frictional moment  $M_{sl}$  under load rotational speeds  $\omega$ . As the rotational speed increases, the total frictional moment decreases, along with the sliding frictional moment, and it is influenced by the rolling frictional moment  $M_{rr}$ . Similar behavior is observed in Fig.(13b), (13c), and (13d).

It is also noted that the rolling friction  $M_{rr}$  is significantly lower than the sliding friction  $M_{sl}$ . For this reason, many researchers neglect the effect of rolling friction and consider only the effects due to sliding friction. In this study both factors are considered for the development of the thermal models.

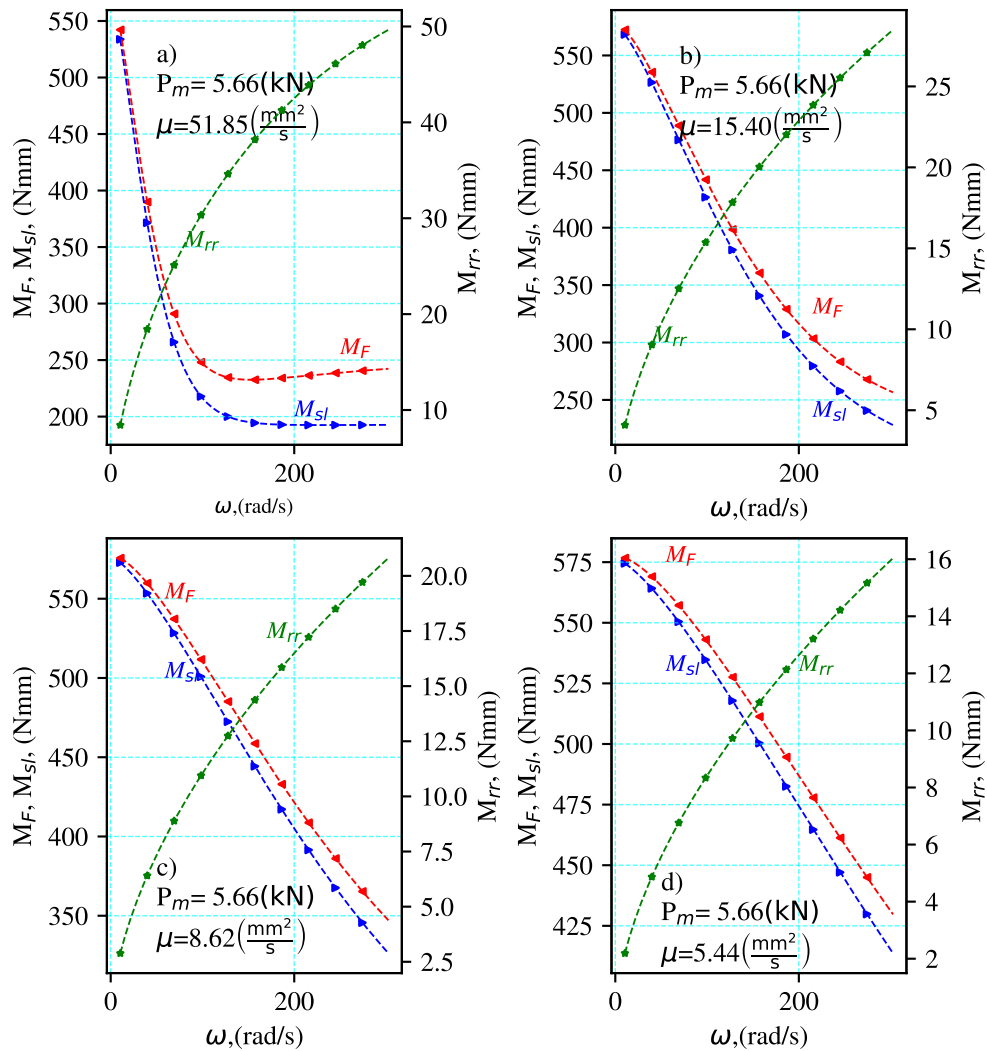


Figure 13: Frictional moments  $M_f$ ,  $M_{sl}$ , and  $M_{rr}$  under the maximum equivalent radial load and different kinematic viscosity  $\nu$ .

To ensure that the total frictional moment  $M_f$  primarily depends on the sliding friction

$M_{sl}$ , calculations were performed with loads below the maximum allowable limit of  $P_m$ . Specifically, the value of kinematic viscosity was kept assuming an operational temperature of  $T_{op} = 80^\circ\text{C}$ . The rotational speed varied within the range of  $10 \leq \omega \leq 305 \left(\frac{\text{rad}}{\text{s}}\right)$ . The bar chart in Fig. (14) shows the frictional moments as a function of the rotational speed  $\omega$  under a load of  $P_m = 1.45\text{kN}$ . It is notable that sliding friction  $M_{sl}$ , primarily determines the frictional behavior of the rolling bearings. The rolling frictional moment  $M_{rr}$  does not represent significance.

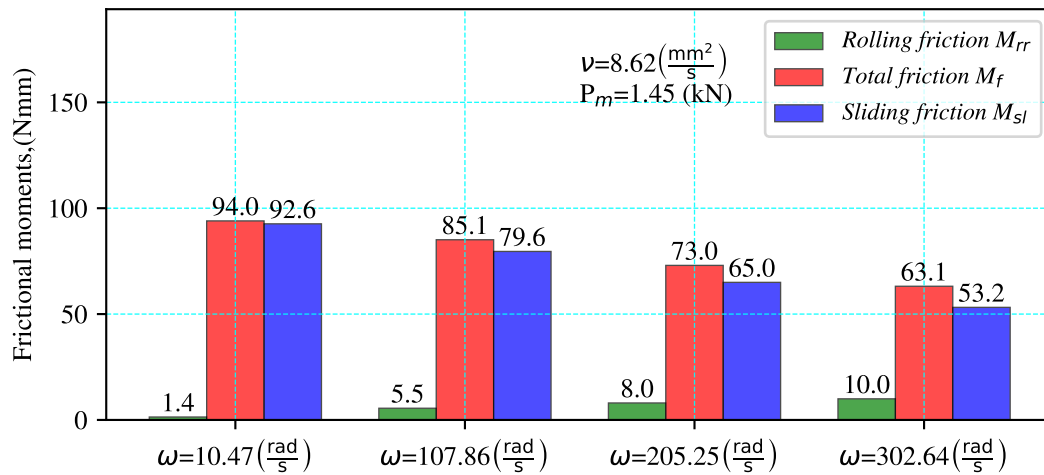


Figure 14: Frictional moments  $M_f$ ,  $M_{sl}$ , and  $M_{rr}$  under a load of  $P_m = 1.45\text{kN}$ .

Similar calculations were performed with varying loads of  $P_m = 2.58\text{ kN}$ ,  $P_m = 3.65\text{ kN}$ , and  $P_m = 4.67\text{ kN}$ . The results are shown in figures Fig. (15), Fig. (16), and Fig. (17), respectively.

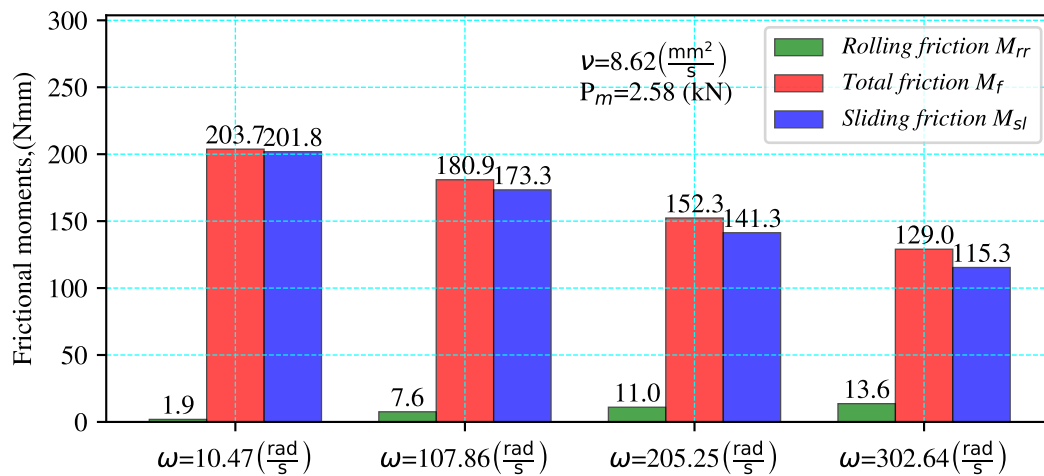


Figure 15: Frictional moments  $M_f$ ,  $M_{sl}$ , and  $M_{rr}$  under a load of  $P_m = 2.58\text{kN}$ .

It can be seen that when the load increases approximately 1 kN, the frictional moments

tend to be almost double as depicted in Fig. (15).

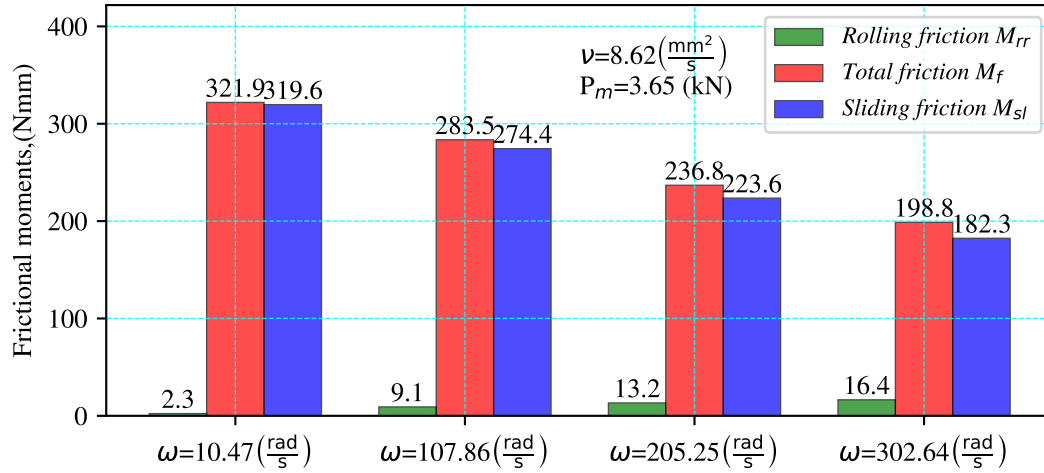


Figure 16: Frictional moments  $M_f$ ,  $M_{sl}$ , and  $M_{rr}$  under a load of  $P_m = 3.65\text{kN}$ .

When the force tends to increase, the sliding frictional moment  $M_{sl}$ , predominates in determining the total friction as shown in Fig. (16), and Fig. (17).

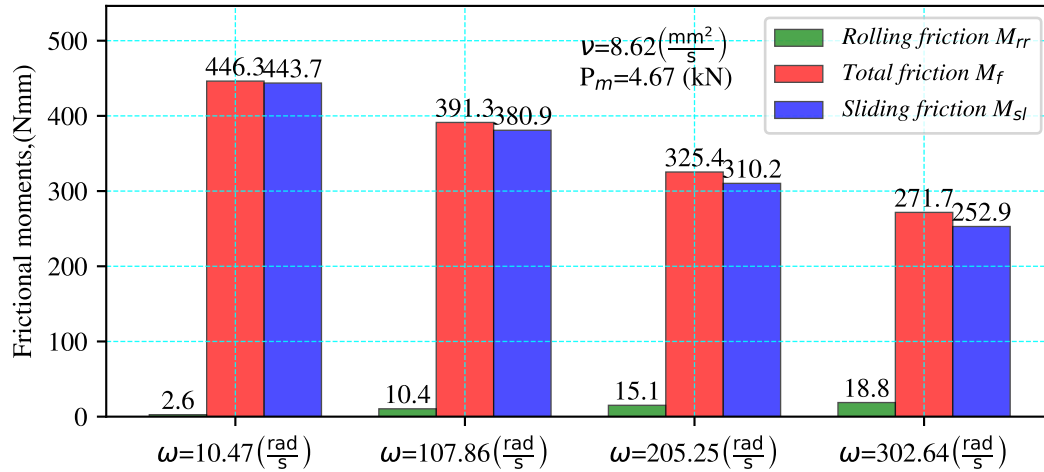


Figure 17: Frictional moments  $M_f$ ,  $M_{sl}$ , and  $M_{rr}$  under a load of  $P_m = 4.67\text{kN}$ .

### 3.8 Determination of the heat generation

The temperature of the surfaces of the components of the angular contact ball bearing can be considered as the sum of two components: the bulk temperature and the transient flash temperature due to the contact of the surfaces at high speeds. The temperatures observed at the contact surfaces, specifically, the inner-ring and balls, and the outer-ring and balls depend on the way in which heat is partitioned between them [63]. Many researchers have

developed methods for calculating the flash temperature assuming dry contact. These approaches cannot be suitable for lubricated surfaces. Between the lubricated surfaces, the dominant heat transfer mechanism is that of conduction, which is perpendicular to the film. These heat transfer mechanism is influenced by the rotational movement: at slower speeds, more heat will be transferred to the surfaces, while at higher speeds, the lubricant absorbs more heat [102]. Based on the studies conducted by [63] and [64], it is understood that the components are not in thermal equilibrium, and the heat generation is not constant. Therefore, heat must be distributed accordingly. For the heat partitioning established in this work, the proposal given by [90] is implemented. The inner-ring is considered to absorb 25 % of the total heat generation, as in the outer-ring. The balls are considered to absorb 50 % of the total heat generated. The total heat generation was determined as a function of the total frictional moment  $M_f$ , and is given in Eq. (27). Furthermore, the total heat generation  $\dot{Q}$ , is not considered as a constant function, but as a function depending on time  $t$ .

$$\begin{aligned}
\dot{Q}_f &= \frac{2 \cdot \pi \cdot n}{60} \cdot 10^{-3} \cdot M_f \\
\dot{Q}_b &= 0.50 \cdot \dot{Q}_f \\
\dot{Q}_i &= 0.25 \cdot \dot{Q}_f \\
\dot{Q}_o &= 0.25 \cdot \dot{Q}_f
\end{aligned} \tag{27}$$

Figure (18) illustrates the heat distribution of the rolling bearing under the maximum dynamic equivalent radial load  $P_m$  for different values of kinematic viscosity  $\nu$  of the lubricant.

According to the behavior shown in Fig. (17a) and Fig. (17b), it is observable that for values of kinematic viscosity  $51.85 \frac{\text{mm}^2}{\text{s}} \leq \nu \leq 15.40 \frac{\text{mm}^2}{\text{s}}$ , the heat generated by the inner-ring and outer-ring does not exceed 20W. When the kinematic viscosity is lower than  $\nu = 10 \frac{\text{mm}^2}{\text{s}}$ , there is a slight increase in heat generation. This increase does not necessarily occur due to the contact of the surfaces of the balls and the inner-ring and outer-ring, but rather due to the heat carried by the lubricant. At this point, the lubricant will transfer heat to the components by convection. The elements that generate more heat are the balls, due to the elastohydrodynamic lubrication will dissipate heat to the inner and outer-ring. Subsequently, the outer-ring will transfer heat to the housing by conduction, considering these elements static, while the inner-ring will transfer heat to the shaft and adjacent components by conduction, but under rotational movement. The

heat partition that is applied in this research was experimentally tested. The experiments will be discussed in the next chapter.

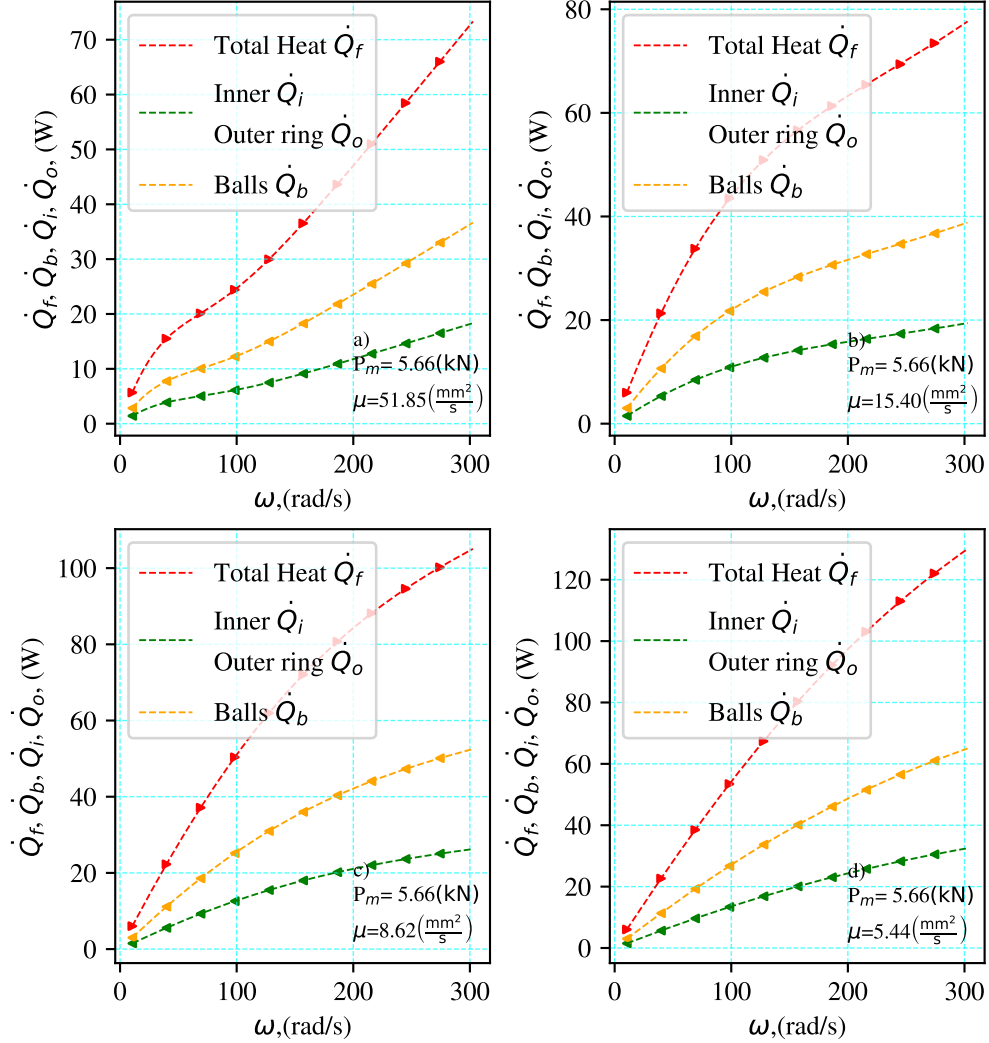


Figure 18: Heat generation  $\dot{Q}$  at the maximum dynamic equivalent radial load  $P_m$  at different rotational speeds  $\omega$  and different kinematic viscosity  $\nu$ .

To foresee the range of heat generation  $\dot{Q}_f$ , Eq. (27) was evaluated at the lowest dynamic equivalent radial load  $P_m = 1.1$  kN implemented in the experimental analysis. At a kinematic viscosity of  $\nu = 51.85$   $\frac{\text{mm}^2}{\text{s}}$ , the total heat generation was  $\dot{Q}_f = 16.70$  W. In the case of  $\nu = 15.40$   $\frac{\text{mm}^2}{\text{s}}$ , the total heat generation was  $\dot{Q}_f = 15.37$  W. For  $\nu = 8.62$   $\frac{\text{mm}^2}{\text{s}}$ , the total heat generation was  $\dot{Q}_f = 19.10$  W, and for  $\nu = 5.44$   $\frac{\text{mm}^2}{\text{s}}$ , the total heat generation was  $\dot{Q}_f = 22.72$  W. Therefore, under the established conditions and considering rotational speeds below  $n = 3000$  rpm, the range of heat is within  $15 \leq \dot{Q}_f \leq 130$  W. Furthermore, the evaluation was performed considering a range

up to the maximum allowable rotational speed  $n = 20000$  rpm under the maximum dynamic equivalent radial load  $P_m = 5.6$  kN. The maximum heat generation was equal to  $\dot{Q} = 554.29$  W. For experimental purposes, the maximum rotational speed for evaluation of the thermal models was  $0 \leq n \leq 2890$  rpm.

The maximum heat generation for rotational speeds within the range of  $0 \leq n \leq 2890$  rpm, is summarized in Table 3.

Table 3: Maximum heat generation  $\dot{Q}_f$  (W) at  $n = 2890$ rpm

$\dot{Q}_f$ (W)				
$P_m$ (kN)	$\nu = 51.85 \frac{\text{mm}^2}{\text{s}}$	$\nu = 15.40 \frac{\text{mm}^2}{\text{s}}$	$\nu = 8.62 \frac{\text{mm}^2}{\text{s}}$	$\nu = 5.44 \frac{\text{mm}^2}{\text{s}}$
1.10	16.70	15.37	19.10	22.72
2.58	30.46	30.05	39.04	47.44
3.65	44.45	45.38	60.15	73.80
4.67	58.73	61.27	82.21	101.40
5.66	73.33	77.65	105.04	130.04

For rotational speeds within  $0 \leq n \leq 20000$  rpm, the maximum heat generation  $\dot{Q}_f$  is given in Table 4.

Table 4: Maximum heat generation  $\dot{Q}_f$  (W) at  $n = 20000$ rpm

$\dot{Q}_f$ (W)				
$P_m$ (kN)	$\nu = 51.85 \frac{\text{mm}^2}{\text{s}}$	$\nu = 15.40 \frac{\text{mm}^2}{\text{s}}$	$\nu = 8.62 \frac{\text{mm}^2}{\text{s}}$	$\nu = 5.44 \frac{\text{mm}^2}{\text{s}}$
1.10	140.81	156.16	151.66	145.09
2.58	236.34	256.47	250.57	241.97
3.65	333.29	357.13	350.14	339.99
4.67	432.27	459.24	451.32	439.87
5.66	533.28	563.01	554.29	541.69

### 3.9 Thermal contact resistances

As described in Section 2.7, the intention of modeling the components of the angular contact ball bearing in the spindle unit as a thermal network, depends on the correct conceptualization of the thermal resistances and the appropriate selection of the nodes that compound the thermal network. The angular contact ball bearing will be modeled as a control volume that can be subdivided into finite sub-volumes (nodes). The effectiveness of the thermal network will depend on the capacity of each node to carry information, such as temperature  $T$ , and heat generation  $Q$ . This can be achieved if the connections of the nodes (thermal resistances), are sufficient to describe the heat transfer

phenomena accurately.

According to the bearing arrangement shown in Fig. (3), the representative model consists of a housing, the outer-ring, the balls, the inner-ring, and the shaft. The housing encapsulates the bearing arrangement, and it is attached to the outer-ring of the angular contact ball bearing. These two elements are considered static elements. The balls roll inside and touch the surfaces of the inner-ring and outer-ring. In this research, the balls were analyzed in two ways: as a moving heat source, and as a thermal node. The inner-ring rotates attached to the shaft. It reassembles a cylindrical union, which is analyzed as a moving thermal resistance. The inner-ring and shaft are not considered as a unique sub-volume, but are separated. The thermal resistance between the surfaces of the bore diameter and the shaft are analyzed separately.

In this section, the general formulations utilized for the determination of the thermal resistances are provided. This formulations are later implemented in each of the the three thermal models that are proposed in this investigation.

### 3.9.1 Thermal resistance formulation for static cylindrical components

The most commonly utilized formulation for cylindrical bodies in spindle units is implemented in this investigation to model the housing and the outer- ring of the bearing given in Eq. (28).

$$R_{th} = \frac{\ln\left(\frac{r_{ext}}{r_{int}}\right)}{2\pi \cdot k \cdot L} \quad (28)$$

### 3.9.2 Thermal resistances of the Mellor thermal network

Mellor developed a complex model to identify temperature variations in most parts of electric machines. The advantage of the Mellor formulation is that it is formulated based on purely dimensional information, along with the thermal properties of the components. This technique has yielded good results in determining the thermal fields of components of cylindrical geometry [76],[94]. However, until now, no studies have implemented this formulation in rolling bearings of spindle units. Considering that the inner-ring and outer-ring of the bearing are cylindrical hollow cylinders, the thermal model based on the lumped parameter method developed by Mellor [94], can be implemented. The purpose of implementing the Mellor formulation in the inner-ring and outer-ring of the bearing is the

possibility of analyzing these components in two-dimensions. Therefore, axial and radial heat fluxes can be analyzed minimizing the complexity of solving the two-dimensional heat transfer equation. In this research, I implement this new concept in rolling bearings, within the Light Gray-Box LPTN and White-Box LPTN. It is important to mention that this model implemented in this work is suitable for temperature monitoring and duty-cycle evaluation.

Figure (19), shows the structure of the Mellor formulation for the inner-ring and outer-ring of the angular contact ball bearing.

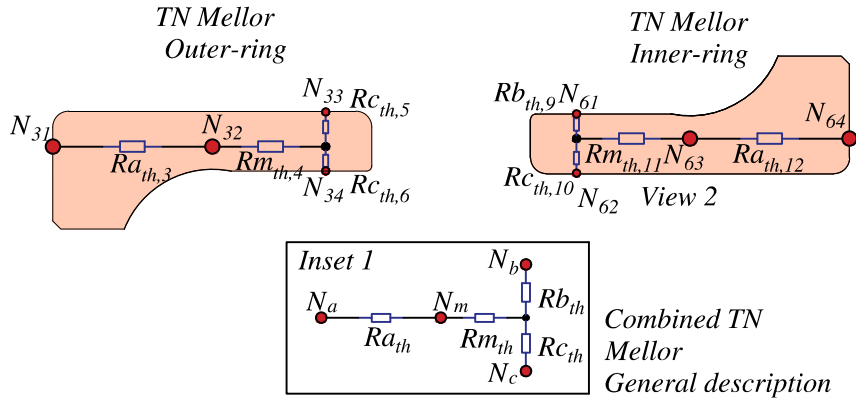


Figure 19: Structure of the Mellor formulation for the inner and outer-ring.

The inset shown in Fig. (18), illustrates the general description of the thermal contact resistances for the Mellor formulation in the inner and outer-ring of the angular contact ball bearing. Equation (29) represent the mathematical formulations for the thermal resistances  $Ra_{th}$ ,  $Rb_{th}$ ,  $Rc_{th}$ , and  $Rm_{th}$ , which form the Mellor thermal network.

$$\begin{aligned}
 Ra_{th,IR;OR} &= \frac{L}{6\pi k (r_{ext.}^2 - r_{int.}^2)} \\
 Rb_{th,IR;OR} &= \frac{1}{2\pi k L} \left[ 1 - \frac{2r_{int.}^2 \ln \left( \frac{r_{ext.}}{r_{int.}} \right)}{(r_{ext.}^2 - r_{int.}^2)} \right] \\
 Rc_{th,IR;OR} &= \frac{1}{2\pi k L} \left[ \frac{2r_{ext.}^2 \ln \left( \frac{r_{ext.}}{r_{int.}} \right)}{(r_{ext.}^2 - r_{int.}^2)} - 1 \right] \\
 Rm_{th,IR;OR} &= \frac{-1}{4\pi k L (r_{ext.}^2 - r_{int.}^2)} \left[ r_{ext.}^2 + r_{int.}^2 - \frac{4r_{ext.}^2 r_{int.}^2 \ln \frac{r_{ext.}}{r_{int.}}}{(r_{ext.}^2 - r_{int.}^2)} \right]
 \end{aligned} \tag{29}$$

### 3.9.3 Thermal contact resistances for static, moving, and combined heat sources

The analysis of heat transfer from sliding in rolling bearings of spindle units has not been extensively developed. Recent studies have modelled the the thermal contact as a stationary heat source [61], [75], [77]. These results have been numerically and experimentally validated, showing good agreement. However, sliding friction in rolling bearings occurs due to the movement of components, implying moving heat sources. To address this issue, this study includes the concept of moving heat sources, considering elliptical contact. For real sliding contacts, Y. S. Muzychka et al. [93] developed models for predicting average and maximum flash temperatures. The formulations implemented in this study are divided into three categories: moving heat sources, due to the sliding contact between the inner-ring and the balls; stationary heat sources, due to the sliding contact between the outer-ring and the balls for the Dark Gray-Box LPTN and Light Gray-Box LPTN; and combined heat sources for the White Box LPTN.

The study assumes an iso-flux heat distribution, meaning that in the elliptical contact, the heat is constant across the entire area of the ellipse.

#### 3.9.3.1 Thermal contact resistances for stationary heat sources

The general expressions for the thermal contact resistance for static heat sources are given in Eq. (30) for the average and maximum iso-flux heat distribution.

$$\begin{aligned}\overline{R}^{sth} &= \frac{16}{3\pi^3 k \sqrt{A_{OR}}} \cdot \sqrt{\pi \epsilon_s} K_1(\epsilon'_s) \\ \hat{R}^{sth} &= \frac{2}{\pi^2 k \sqrt{A_{OR}}} \cdot \sqrt{\pi \epsilon_s} K_1(\epsilon'_s),\end{aligned}\tag{30}$$

where  $\epsilon'_s = \sqrt{1 - \epsilon_s^2}$ .

It can be observed that stationary thermal resistances depend on the force generated during machining operations. Fig. (20), depicts the behavior of the thermal resistances for stationary heat sources for the inner-ring and outer-ring of the bearing.

#### 3.9.3.2 Thermal contact resistances for moving heat sources

The expressions for the moving heat sources depend on the Peclet number. For real contact, I have implemented a modified Peclet number  $Pe^*_{\sqrt{A_{IR,OR}}}$ , which is calculated using Eq. (31).

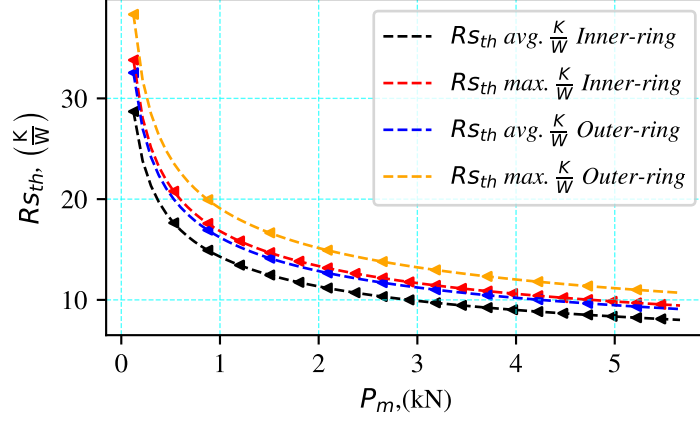


Figure 20: Thermal contact resistances for stationary heat sources.

$$Pe^*_{\sqrt{A_{IR;OR}}} = (\epsilon_m)^{\frac{1}{2}} \frac{v_x \cdot \sqrt{A_{IR;OR}}}{\alpha_D} \quad (31)$$

For moving heat sources in iso-flux heat distribution the average and maximum thermal resistances are given in Eq. (32)

$$\begin{aligned} \overline{Rm}_{oth} &= \frac{0.750}{k\sqrt{A_{IR;OR}}Pe^*_{\sqrt{A_{IR;OR}}}} \\ \hat{Rm}_{oth} &= \frac{1.20}{k\sqrt{A_{IR;OR}}Pe^*_{\sqrt{A_{IR;OR}}}} \end{aligned} \quad (32)$$

### 3.9.3.3 Thermal contact resistances for combined heat sources

For combined heat sources in iso-flux heat distribution the average and maximum thermal resistances were calculated using Eq. (33).

$$\begin{aligned} \overline{Rco}_{th} &= \frac{0.750}{k\sqrt{A_{IR;OR}} \left( Pe^*_{\sqrt{A_{IR;OR}}} + \frac{6.05}{\epsilon_s K_1^2 (\epsilon'_s)} \right)} \\ \hat{Rco}_{th} &= \frac{1.20}{k\sqrt{A_{IR;OR}} \left( Pe^*_{\sqrt{A_{IR;OR}}} + \frac{11.16}{\epsilon_s K_1^2 (\epsilon'_s)} \right)} \end{aligned} \quad (33)$$

Fig. (22) illustrates the behavior of the thermal contact resistances for combined heat sources as a function of the rotational speed and the dynamic load  $P_m$ . This behavior is observed only between the outer-ring, representing the static element, and the balls, representing the moving element.

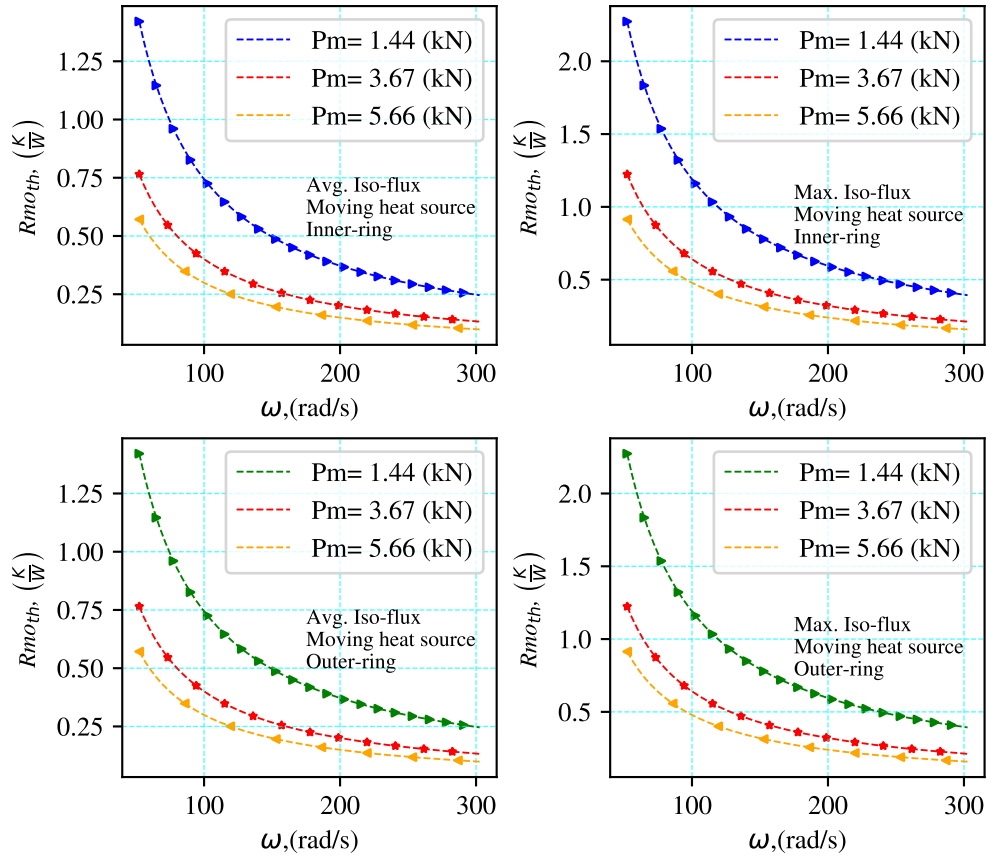


Figure 21: Thermal contact resistances  $R_{mth}$  for moving heat sources.

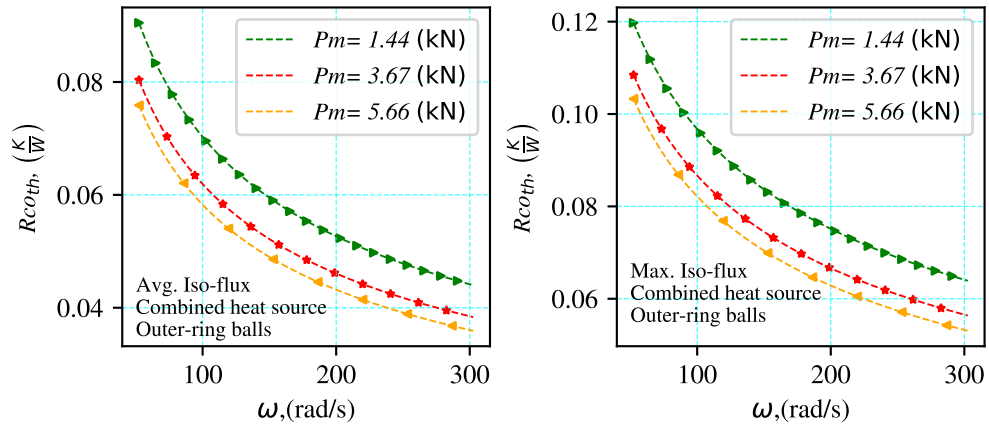


Figure 22: Thermal contact resistances  $R_{coth}$  for combined heat sources.

In comparison with the behavior depicted in Fig. (21) for moving heat sources of the outer-ring, it is evident that the thermal resistances are significantly lower implying a major heat flux  $\dot{Q}$  from one element to another.

### 3.9.4 Thermal constriction resistance

The contact interface between the inner-ring and the shaft consists of a multiple contact spots and gaps that cannot be precisely determined due to their microscopic nature. Heat by conduction will be transferred through the small spots in contact between these two elements, which act as a conducting medium [103]. The constriction resistance allows for a mathematical formulation to analyze the resistance of heat that flows through the inner-ring and the shaft. This resistance is determined as a function of the alleviation factor, which is the ratio between the small radius contact spot and the major radius contact spot in an idealized contact plane between the inner-ring and the shaft. Many authors including, Roess, Gibson, and Negus and Yovanovich have proposed algebraic expressions for the determination of the alleviation factor [103], which are given in Eq. (34) considering the four terms of the series of expansions. In my research, I considered an idealized contact plane between the external surface of the shaft and the inner surface of the bearing's inner-ring. The alleviation factor is represented by the ratio between the radio of an idealized contact spot  $l_a$ , and the length of the contact surface  $l_b$ , which characterises the diameter of the shaft, as shown in Fig. (23).

$$\begin{aligned}
 F_{Roess} &= 1 - 1.4093 \cdot \left(\frac{l_a}{l_b}\right) + 0.2959 \cdot \left(\frac{l_a}{l_b}\right)^3 + 0.0524 \cdot \left(\frac{l_a}{l_b}\right)^5 \\
 F_{Gibson} &= 1 - 1.4092 \cdot \left(\frac{l_a}{l_b}\right) + 0.3380 \cdot \left(\frac{l_a}{l_b}\right)^3 + 0.0679 \cdot \left(\frac{l_a}{l_b}\right)^5 \\
 F_{N.Y.} &= 1 - 1.4098 \cdot \left(\frac{l_a}{l_b}\right) + 0.3441 \cdot \left(\frac{l_a}{l_b}\right)^3 + 0.0435 \cdot \left(\frac{l_a}{l_b}\right)^5
 \end{aligned} \tag{34}$$

The alleviation factors determined by Eq. (34) do not vary significantly from each other. For that reason, the thermal constriction resistance in this research is calculated using the latest formulation given by Negus et al. [104], which is based on superposing Neumann specified solution for the Laplace equation according to the least square criterion.

The radio of the contact spot was varied from 0.0001 – 0.1mm. The results of the alleviation factors using the three formulations of Eq. (34), are given in Table 5.

The results show no variation in the constriction alleviation factor, which can be approximated to 1. The thermal constriction resistance is determined using Eq. (35).

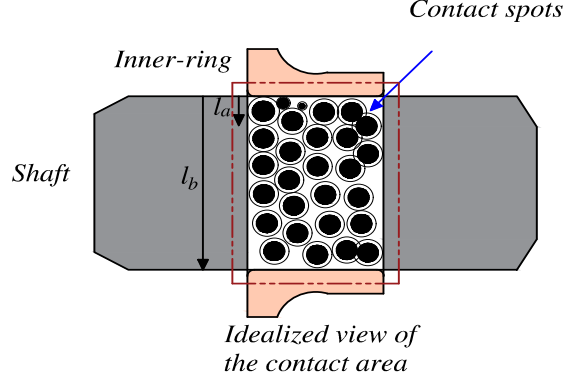


Figure 23: Constriction alleviation factor

Table 5: Constriction alleviation factors

$l_a$	$\frac{l_a}{l_b}$	$F_{Roess}$	$F_{Gibson}$	$F_{N.Y.}$
0.0001	$5.88 \cdot 10^{-6}$	0.99999	0.99999	0.99999
0.01	$5.88 \cdot 10^{-4}$	0.99917	0.99917	0.99917
0.1	$5.88 \cdot 10^{-3}$	0.99917	0.99917	0.99917

$$R_{consth} = \frac{F_{Roess}}{4 \cdot l_a \cdot k} = \frac{F_{Gibson}}{4 \cdot l_a \cdot k} = \frac{F_{N.Y.}}{4 \cdot l_a \cdot k} \quad (35)$$

### 3.9.5 Thermal resistances by convection

The general expressions for the thermal contact resistances by convection are calculated as functions of the surface area in contact with the fluids (oil lubricant and air), and the heat convection coefficient of air  $h_{air}$ , the inner-ring  $h_i$ , outer-ring  $h_o$ , and the balls  $h_b$ , and are given in Eq. (36).

$$\begin{aligned} R_{th,h} &= \frac{1}{A_h \cdot h_{air}} \\ R_{th,or} &= \frac{1}{A_o \cdot h_o} \\ R_{th,b} &= \frac{1}{A_b \cdot h_b} \\ R_{th,ir} &= \frac{1}{A_i \cdot h_i} \end{aligned} \quad (36)$$

### 3.10 State Space Method for monitoring thermal fields in rolling bearings of spindle systems

This methodology has wide applications in control systems with two primary focuses: control and monitoring. Due to its advantages, including the analysis of multi-variable

systems, non-linear and time variant systems, and the capabilities of monitoring design approaches, I have considered this technique applicable for the determination of the thermal fields in my research. Some authors have implemented this technique for the determination of the induced pre-loads, which will cause thermal changes in the spindle system [90]. However, it has been observed that the method has not yet been implemented to predict the temperature distribution in rolling bearings of spindle units.

In the angular contact ball bearing, I have set a number of variables that define the thermal system of the rolling bearing, these are the thermal fields analyzed for each of the three thermal models (Dark Gray-Box, Light Gray-Box, and White Box LPTN), which will be described at detail in the results. The input variables were simplified to the environmental temperatures and the heat generation  $\dot{Q}$ .

The state equation is defined as a matrix function of the state vector differential equation, and is given in Eq. (37).

$$\dot{x} = Ax + Bu, \quad (37)$$

where  $x$ , represents the state of the system, which are the temperature of the housing  $T_h$ , outer-ring  $T_o$ , balls  $T_b$ , and inner-ring  $T_i$ . The  $A$  matrix, defines how the state variables evolve over time. This matrix contains the thermal properties, as well as geometrical properties of the control volumes where the state variables are analyzed. The  $B$  matrix determine how the input variables of the system affect the state variables.

The output vector of the system is given in Eq. (38).

$$y = Cx + Du, \quad (38)$$

where  $y$  represents the output of the system at time  $t$ .

Equation (37) and Eq. (38) show the generalized view of the state space approach which is applied in the development of the thermal models in Chapters 4 Dark Gray-Box LPTN, and Chapter 5 Light Gray-Box LPTN and White-Box LPTN.

### 3.11 Conclusion of the chapter

The complete formulations and conceptualizations necessary for the development of the thermal models were discussed and analyzed in this chapter. The type of bearing arrangement was determined in this application as DB-Bearing arrangement. The external and internal parameters were studied, including the determination of the dynamic equivalent radial load  $P_m$  and the axial  $F_a$  and radial loads  $F_r$  were investigated. The lubrication effects and the methods for determining the kinematic viscosity of the systems were defined. The environmental conditions were established for the representative model, and the values of the convective coefficient of air  $h_{air}$  for low speeds were calculated. The rolling contact analysis was discussed in detail, establishing the determination of the semi-major  $a$  and semi-minor  $b$  axes of the ellipse contact. Considering that the rolling bearing implemented in the representative model is manufactured by SKF, its own frictional model was implemented. After that, the heat partition concept was applied to calculate the heat generation in the components of the angular contact ball bearing. The thermal contact resistances that will be implemented in each thermal model were discussed and formulated considering static, moving, combined heat sources, the Mellor formulation, the thermal constriction resistance and the thermal resistances by convection. Finally the State-space approach was established for monitoring the thermal fields of the bearing.

## 4 Dark Gray-Box LPTN

After an extensive investigation, I have observed that many researchers have proposed different thermal models for spindle units, in a vast majority based on FEA simulations. Apart from this application, it was observed that several investigations have involved the development of thermal networks, considering the bearings as heat sources and not investigating their inner parts separately. An important motivation to create a straightforward thermal network of the angular contact ball bearings was the possibility to determine the thermal fields of the different components of this element (housing/ outer-ring, balls, inner-ring). This Chapter presents the development of the Dark Gray-Box LPTN and the application in the determination of the thermal fields for the housing and outer-ring  $T_{ho}$ , the balls  $T_b$ , and the inner-ring  $T_i$ . The new model is compared with FEA simulations and experimental measurements for its validation.

### 4.1 Definition of the DGB Lumped parameter thermal network

Monitoring critical temperatures in the bearings of a spindle system prevents failures of the system, along with the correct performance of the system during machining operations. The global identification of Lumped parameter thermal networks was first introduced for the analysis of electric machines [16]. The models proved to be efficient in predicting thermal fields without the necessity of conducting physical measurements, which imply the implementation of sophisticated measurements systems and high costs. Furthermore, it was observed that it is not convenient to implement numerous sensors, which are not practical from the perspective of design [105]. The investigation showed me that due to the comparable geometries and similar thermal behavior, the Dark Gray-Box LPTN implemented in electrical machines can be applied in angular contact ball bearings.

This type of thermal network, represents an abstract design because its elements are not divided into multiple nodes. Despite its abstraction, it serves as a primary tool, which

can be applied to estimate average temperatures on the elements. The method requires basic knowledge of the theory of heat transfer, demands little computational resources, and can provide temperature estimations in short time. However, the drawbacks of this thermal network include, the minimum information output. It is more suited for providing results about steady state rather than transient state. Moreover, certain parameters cannot vary [16], [105], namely, thermal contact resistances for moving heat sources.

## 4.2 Development of the DGB thermal network

The Dark Gray-Box LPTN was conceived as a low order thermal network consisting of five nodes, which are necessary to describe the thermal fields of the housing and outer-ring  $T_{ho}$ , the balls  $T_b$ , and the inner-ring  $T_i$ . The housing and the outer-ring were established as a unique body, considering that these two elements are static and possess equivalent thermal properties, including thermal conductivity  $k$  and specific heat  $c_p$ . Similar consideration was established for the inner-ring and shaft, which are coupled components rotating at equal movement. The thermal nodes are:  $N_1$ , which represents the surroundings of the housing;  $N_2$ , which represents the housing and outer-ring;  $N_3$ , which represents the lubricant film;  $N_4$ , which represents the ball; and  $N_5$ , which represents the inner-ring and shaft.

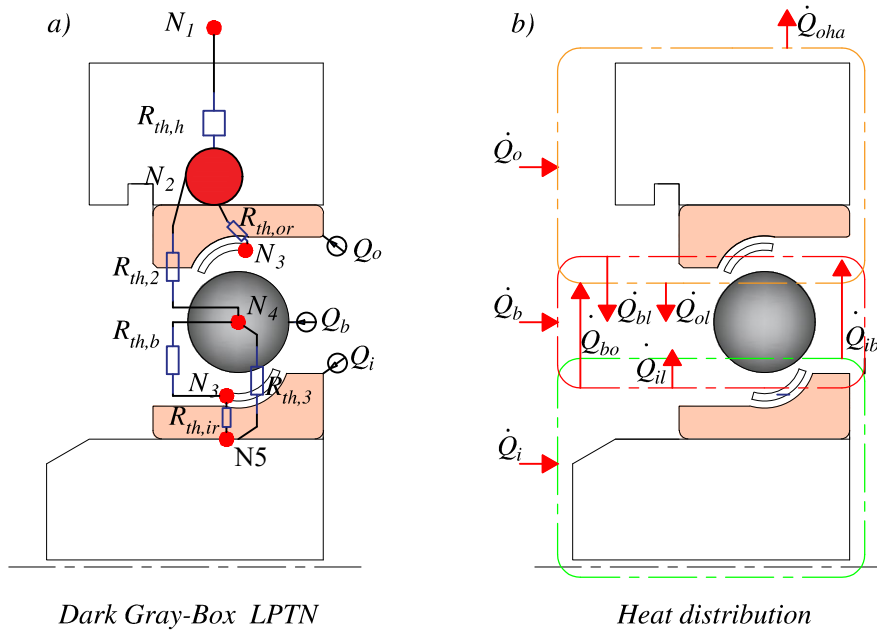


Figure 24: a) Dark Gray-Box LPTN. b) Energy distribution through the bearing

The thermal model is composed of six thermal resistances:  $R_{th,1}$ , which represents the thermal contact resistance for cylindrical elements;  $R_{th,or}$ , which represents the thermal resistance by convection between the internal surface of the outer-ring and the lubricant film;  $R_{th,2}$ , which represents the thermal resistance by conduction between the outer-ring and the ball and is described as a static heat source;  $R_{th,ir}$ , which represents the thermal resistance by convection between the inner-ring and the lubricant film;  $R_{th,b}$ , which represents the thermal resistance by convection between the ball and the lubricant film; and  $R_{th,3}$ , which represents the thermal resistance between the coupled inner-ring / shaft and ball.

The thermal network is characterized by three heat sources calculated using the heat partitioning concept given in Eq. (27). The heat sources are the outer-ring  $\dot{Q}_o$ , the balls  $\dot{Q}_b$ , and the inner-ring  $\dot{Q}_i$ .

The graphical representation of the Dark Gray-Box LPTN is illustrated in Fig. (24 a). The nodal description of the thermal model is given in Table 6.

Table 6: Nodal description of the thermal network

Dark Gray-Box LPTN					
Node	$N_1$	$N_2$	$N_3$	$N_4$	$N_5$
Source	<i>Ambient</i>	<i>Outer-ring/housing</i>	<i>Oil-film</i>	<i>Ball</i>	<i>Inner-ring/shaft</i>

The thermal resistances are calculated based on the mathematical formulations provided in Section 3.9. The Equations are summarized in Table 7.

Table 7: Thermal resistances of the Dark Gray-Box LPTN

Designation	Description	Type	Equation	Formula
$R_{th,or}$	outer-ring and oil film	Conv.	Eq. (36)	$R_{th,or} = \frac{1}{A_o \cdot h_o}$
$R_{th,2}$	outer-ring and ball	Cond.	Eq. (30)	$\hat{R}s_{th} = \frac{2}{\pi^2 k \sqrt{A_{OR}}} \cdot \sqrt{\pi \epsilon_s} K_1 \left( \epsilon'_s \right)$
$R_{th,ir}$	inner-ring and oil film	Conv.	Eq. (36)	
$R_{th,b}$	ball and oil film	Conv.	Eq. (36)	$R_{th,b} = \frac{1}{A_b \cdot h_b}$
$R_{th,3}$	inner-ring/ shaft and ball	Avg. Mov.	Eq. (32)	$\hat{R}m_{oth} = \frac{1.20}{k \sqrt{A_{IR:OR}} P e^* \sqrt{A_{IR:OR}}}$
$R_{th,h}$	housing/ air	Conv.	Eq. (36)	$R_{th,h} = \frac{1}{A_{hou} \cdot h_{air}}$

Having determined the elements that comprise the thermal network, including nodes, thermal resistances, and heat paths, the heat transfer of energy that is governed by both the conservation of energy (First law of Thermodynamics), and constitutive laws, including Fourier's Law of heat transfer, which describe the material-dependent nature of heat conduction, were implemented to create the systems of equations that describe mathematically the proposed thermal model.

### 4.3 Results and new contributions

#### 4.3.1 Mathematical model of the Dark Gray-Box LPTN

To develop the thermal network, algebraic operations following Kirchoff's law (Heat balance) were implemented to define the correct heat path and heat distribution depicted in Fig. (24b). The system of equations relates the physical characteristics of the elements, including the masses, the thermal properties, nodal positions, heat paths, and thermal resistances. Having said that, the system of equations presented in Eq. (39) represents the new low order lumped parameter thermal network. Considering that these system is a low order lumped parameter system, the expected results should be reasonable if the standard deviation calculated between FEA simulations and experimental measurements do not exceed 5 %.

$$\begin{aligned}
 m_{oh}c_p \frac{dT_{oh}}{dt} &= \dot{Q}_o - T_{oh} \left( \frac{1}{R_{th,2}} + \frac{1}{R_{th,or}} + \frac{1}{R_{th,h}} \right) + \frac{T_b}{R_{th,2}} + \frac{T_{N_3}}{R_{th,or}} \\
 Nm_b c_p \frac{dT_b}{dt} &= \dot{Q}_b + \frac{T_{oh}}{R_{th,2}} - T_b \left( \frac{1}{R_{th,2}} + \frac{1}{R_{th,b}} + \frac{1}{R_{th,3}} \right) + \frac{T_i}{R_{th,3}} + \frac{T_{N_3}}{R_{th,ir}} \\
 m_i c_p \frac{dT_i}{dt} &= \dot{Q}_i + \frac{T_b}{R_{th,3}} - T_i \left( \frac{1}{R_{th,3}} + \frac{1}{R_{th,ir}} \right) + \frac{T_{N_3}}{R_{th,ir}}
 \end{aligned} \tag{39}$$

The heat distribution shown in Fig. (24b) is detailed in Table 8.

Table 8: Heat transfer in the Dark Gray-Box LPTN

Type of heat	Description
$\dot{Q}_{ha}$	Heat dissipated from the housing/outer-ring to the surroundings (W).
$\dot{Q}_o$	Heat generated by friction of the outer ring (W).
$\dot{Q}_b$	Heat generated by friction of the balls (W).
$\dot{Q}_i$	Heat generated by friction of the inner-ring (W).
$\dot{Q}_{ib}$	Heat dissipated from the inner-ring to the balls (W).
$\dot{Q}_{bl}$	Heat dissipated from the balls to the lubricant film (W).
$\dot{Q}_{ol}$	Heat dissipated from the outer-ring to the lubricant film (W).
$\dot{Q}_{il}$	Heat dissipated from the inner-ring to the lubricant film (W).
$\dot{Q}_{bo}$	Heat dissipated from the ball to the outer-ring (W).

#### 4.3.2 Solutions in stationary state using the State-Space approach

The mathematical model was developed as an observer, meaning that the model has the capacity to predict the thermal behavior of the system. The observability characteristic of the system was evaluated according to [91]. To achieve this, the State-Space approach is applied. The system is considered as a multiple-input and multiple-output system,

in which the state variables are determined as a step response of a first order dynamic system  $(T_{oh}, T_b, T_i)$ . The inputs of the system are the rotational speed, the external forces, and the frictional moments. However, this variables are represented in the system as the heat generation  $\dot{Q}$ , the inner temperature of the lubricant  $T_{N_3}$  in Eq. (10), and the heat by convection from the surroundings expressed by the temperature  $T_{air}$ . The final system equation of the Dark Gray-Box LPTN, expressed in state-space response is given in Eq. (40).

$$\begin{bmatrix} m_{oh}c_p\dot{T}_{oh} \\ Nm_b c_p\dot{T}_b \\ m_i c_p\dot{T}_i \end{bmatrix} = \begin{bmatrix} -\left(\frac{1}{R_{th,2}} + \frac{1}{R_{th,or}} + \frac{1}{R_{th,h}}\right) & \frac{1}{R_{th,2}} & 0 \\ \frac{1}{R_{th,2}} & -\left(\frac{1}{R_{th,2}} + \frac{1}{R_{th,or}} + \frac{1}{R_{th,h}}\right) & \frac{1}{R_{th,3}} \\ 0 & \frac{1}{R_{th,3}} & -\left(\frac{1}{R_{th,3}} + \frac{1}{R_{th,ir}}\right) \end{bmatrix} \begin{bmatrix} T_{oh} \\ T_b \\ T_i \end{bmatrix} + \begin{bmatrix} 0.25 & \frac{1}{R_{th,h}} & \frac{1}{R_{th,or}} \\ 0.5 & 0 & \frac{1}{R_{th,ir}} \\ 0.25 & 0 & \frac{1}{R_{th,ir}} \end{bmatrix} \begin{bmatrix} \dot{Q} \\ T_{air} \\ T_{N_3} \end{bmatrix}$$

$$y = \begin{bmatrix} 1 & 0 & 0 \\ 0 & 1 & 0 \\ 0 & 0 & 1 \end{bmatrix} \begin{bmatrix} T_{oh} \\ T_b \\ T_i \end{bmatrix} \quad (40)$$

#### 4.3.2.1 Experimental validation of the Dark Gray-Box LPTN

To validate the solution of the system under steady state conditions, FEA simulations were performed, along with experimental measurements. The experimental measurements were carried out using an experimental rig on which the representative model was mounted. The forces were exerted by a hydraulic piston emulating the dynamic equivalent radial load  $P_m$ , which was measured using a force transducer, and the rotational speed was changed using a variable frequency driver. Thermocouples type J were connected to the static parts of the system, these are: the outer-ring and the housing. Figure (25) shows the experimental rig used for validation.

The force exerted by the hydraulic piston varied from  $0.5 \leq P_m \leq 5.6$  kN. The rotational speed was varied from  $600 \leq n \leq 2890$  rpm, which is the maximum capacity of the electrical motor from the experimental jig. Measurements were taken until the sensors 1S, 2S, 3S, 4S shown in Fig. (25), exhibited no temperature variation, indicating that steady state conditions have been reached.

The temperature of the surrounding is given by the thermal conditions of the workshop, where the experiments were carried out. In this case the temperature fluctuation inside the workshop varies from  $25 \leq T_{air} \leq 27^\circ\text{C}$ . Following, many experiments that were

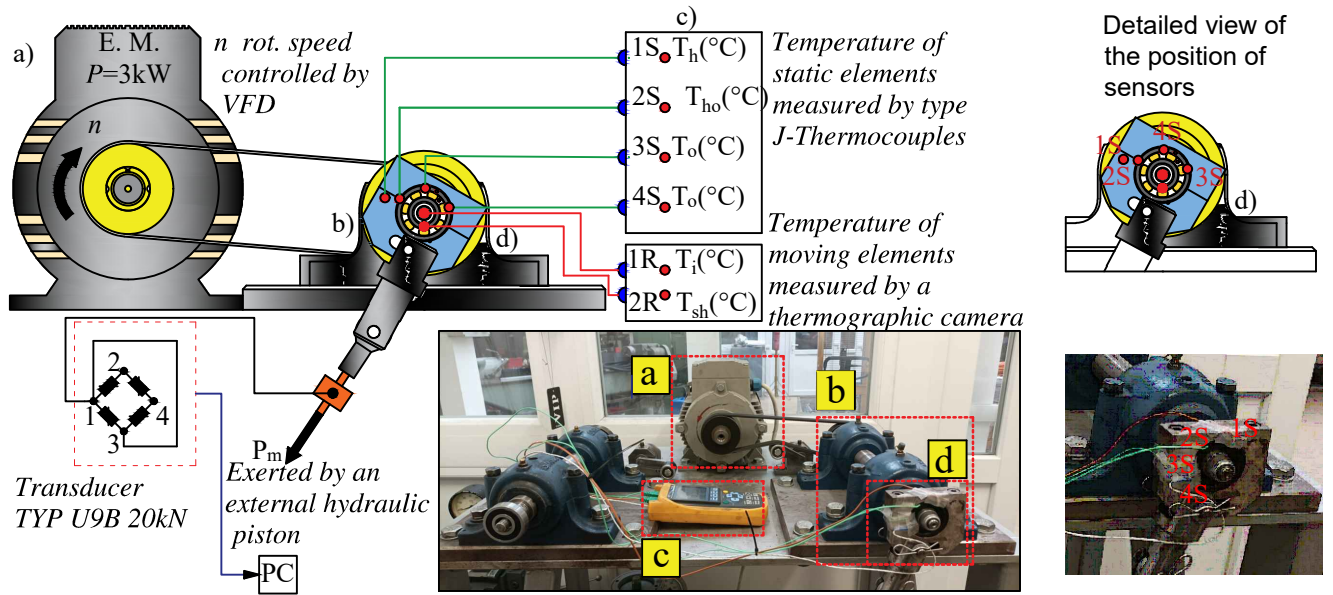


Figure 25: Experimental testing rig

carried out will be presented, and the results will be illustrated showing the thermal model of the Dark Gray-Box LPTN, the experimental measurements for the outer-ring and housing, and FEA simulations, for the housing/outer-ring, balls and inner ring.

#### 4.3.2.2 Finite Element Analysis Simulation

Finite Element Analysis (FEA) was implemented to compare the results obtained by the thermal networks for all components. Since it is not possible to experimentally measure the temperature in the moving elements (balls and inner-ring), FEA simulations provide a suitable method for comparing the solutions obtained from the thermal networks. Two types of analysis were carried out: Steady-State Thermal and Transient Thermal analysis, both based on Ansys Wokbench. To begin with, the elements of the thermal network are treated as control volumes. For the Dark Gray-Box LPTN, the control volumes include the housing/ outer-ring, balls, and inner-ring. The second important parameter is the definition of the geometry and the thermal properties of the material, including thermal conductivity and specific heat. After that, the creation of the mesh is a crucial step. It is important to identify the contact zones, which are defined by the elliptical contact areas formed in the outer-ring, the balls, and the inner-ring. These zones were meshed as surfaces with a refinement of 0.0001 m per element. The rest of the control volumes were meshed as volumes (tetrahedral elements), with a refinement of 0.002. The meshing algorithm technique implemented was the Patch-Conforming Algorithm. The next step

was to define the initial and boundary conditions. The boundary conditions for the analysis were boundary conditions of the first kind (Dirichlet). The simulation time was established when the sensors in the experimental analysis showed no variation, indicating steady-state conditions.

The procedure of the FEA analysis is given in the scheme shown in Fig. (26), similar to other research investigations involving FEA simulations .

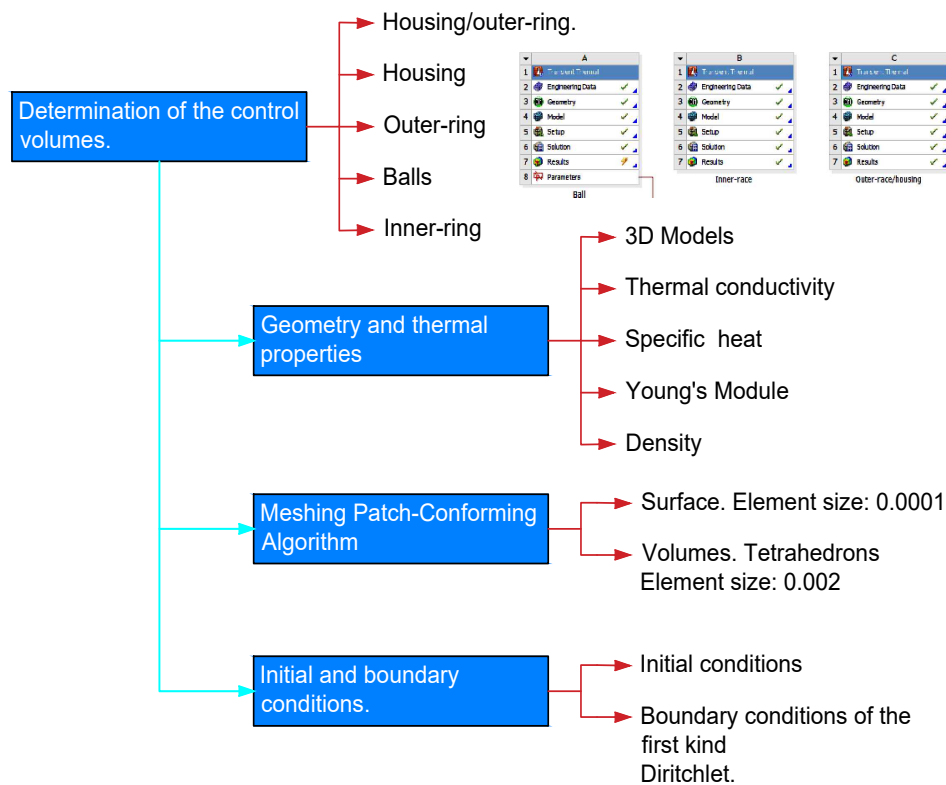


Figure 26: FEA simulations procedure for the Drak Gray-Box LPTN

Figure (27) illustrates the meshing type and the FEA simulations related to experiment 2. It is important to remark that all the experiments follow the same pattern.

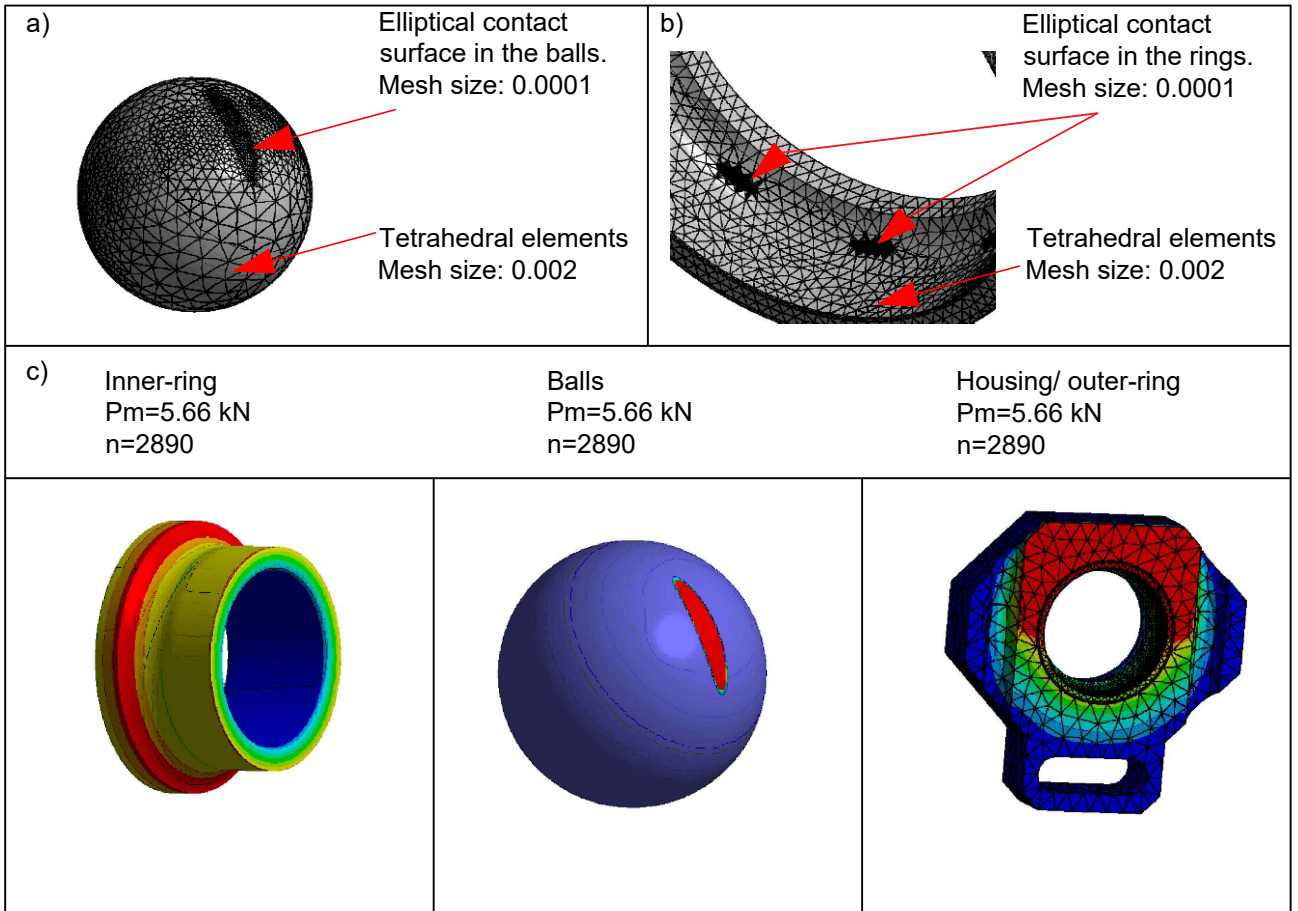


Figure 27: FEA Simulation for experiment 2) at  $P_m = 5.66$  kN at  $n = 2890$  rpm.

#### 4.3.2.3 Dark Gray-Box LPTN model validation for stationary conditions

As described in Section 4.3.2.1, several experiments were conducted, along with the Dark Gray-Box LPTN model, and FEA simulations. For illustration, three experiments will be shown in the graphics and the rest of the experiments will be tabulated. The experiments consist of varying the force  $P_m$  in combination with the rotational speed  $n$ , which are the input parameters.

##### Experiment 1)

In the first experiment, the equivalent dynamic radial load  $P_m = 0.578$  kN and the rotational speed  $n = 625$  rpm were established, enabling the rotation of the representative model depicted in Fig. (24). Under these conditions, it was observed that steady-state conditions were reached at  $t = 200$  s, when sensors 1S, and 3S connected to the housing and outer-ring showed no variation. The thermal model given in Eq. (40), was calculated considering  $t = 200$  s. FEA simulations were performed and compared with the experimental results and the thermal model for the subassembly housing/outer-ring. For the

balls and the inner-ring, FEA simulations, along with the thermal model, were compared. These results are depicted in Fig. (28).

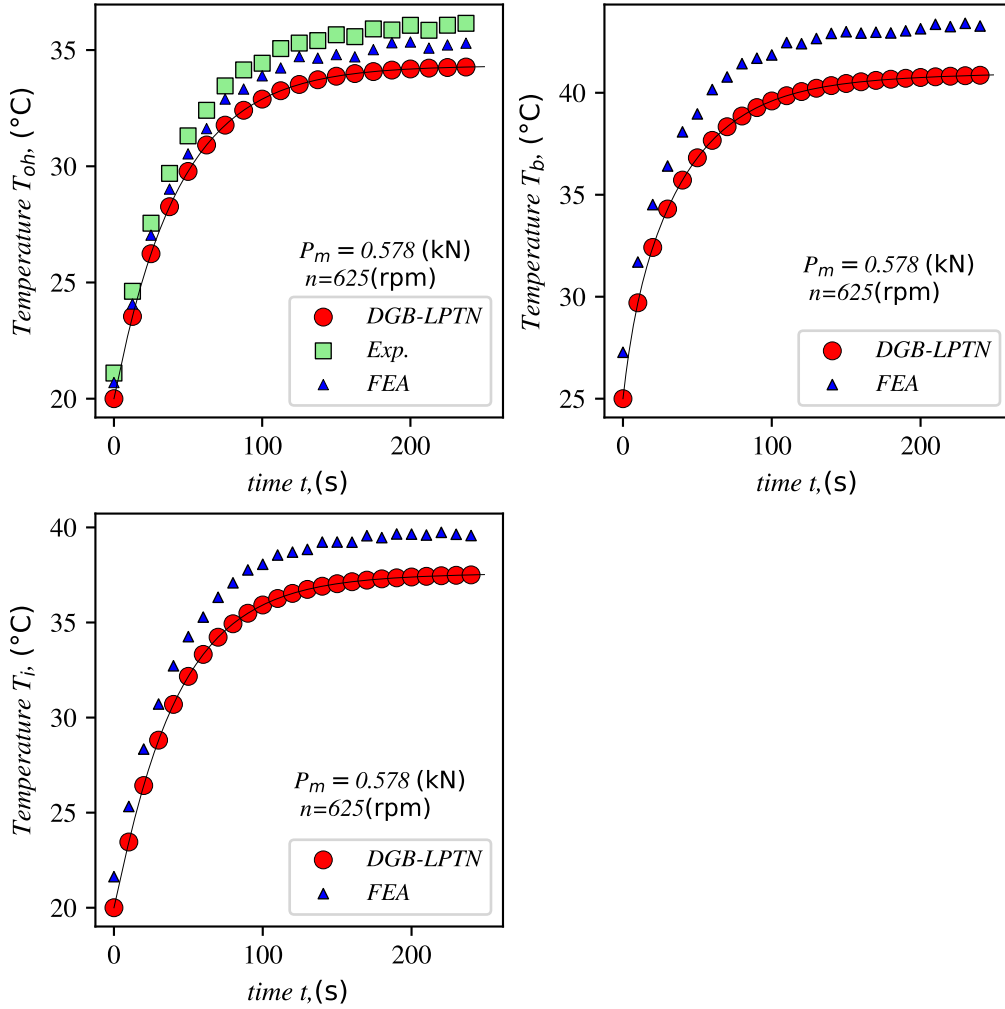


Figure 28: Dark Gray-Box LPTN  $P_m = 0.578$  kN,  $n = 625$  rpm.

The experimental measurements obtained by sensors 1S and 3S were considered as the reference values for comparison. The experimental temperature at  $t = 200$  s was equal to  $T_{oh} = 36.00$   $^{\circ}\text{C}$ . The value obtained through FEA simulations was equal to  $T_{oh} = 35.35$   $^{\circ}\text{C}$ . The value obtained by the Dark Gray-Box LPTN model was equal to  $T_{oh} = 34.28$   $^{\circ}\text{C}$ . The same procedure was followed for the determination of the temperature in the balls, where the FEA simulation was equal to  $T_b = 43.19$   $^{\circ}\text{C}$ , and the Dark Gray-Box LPTN model was equal to  $T_b = 40.87$   $^{\circ}\text{C}$ . Finally, the temperature of the inner-ring obtained by FEA simulations was equal to  $T_i = 39.87$   $^{\circ}\text{C}$ , and the Dark Gray-box LPTN was equal to  $T_b = 37.51$   $^{\circ}\text{C}$ . It is also observable from the three models depicted in Fig. (28).

## Experiment 2)

In this experiment, the maximum value of  $P_m = 5.66$  kN, allowed by the bearing manufacturer, and the maximum value of rotational speed  $n = 2890$  rpm that can be achieved in the experimental testing jig, were established. The main objective of this experimental analysis was to determine the thermal fields under limit conditions. Steady state conditions were reached at  $t = 150$  s. It is evident that the temperature increase under these conditions is excessive, as depicted in Fig. (29). However, the model can predict the temperature behavior accordingly.

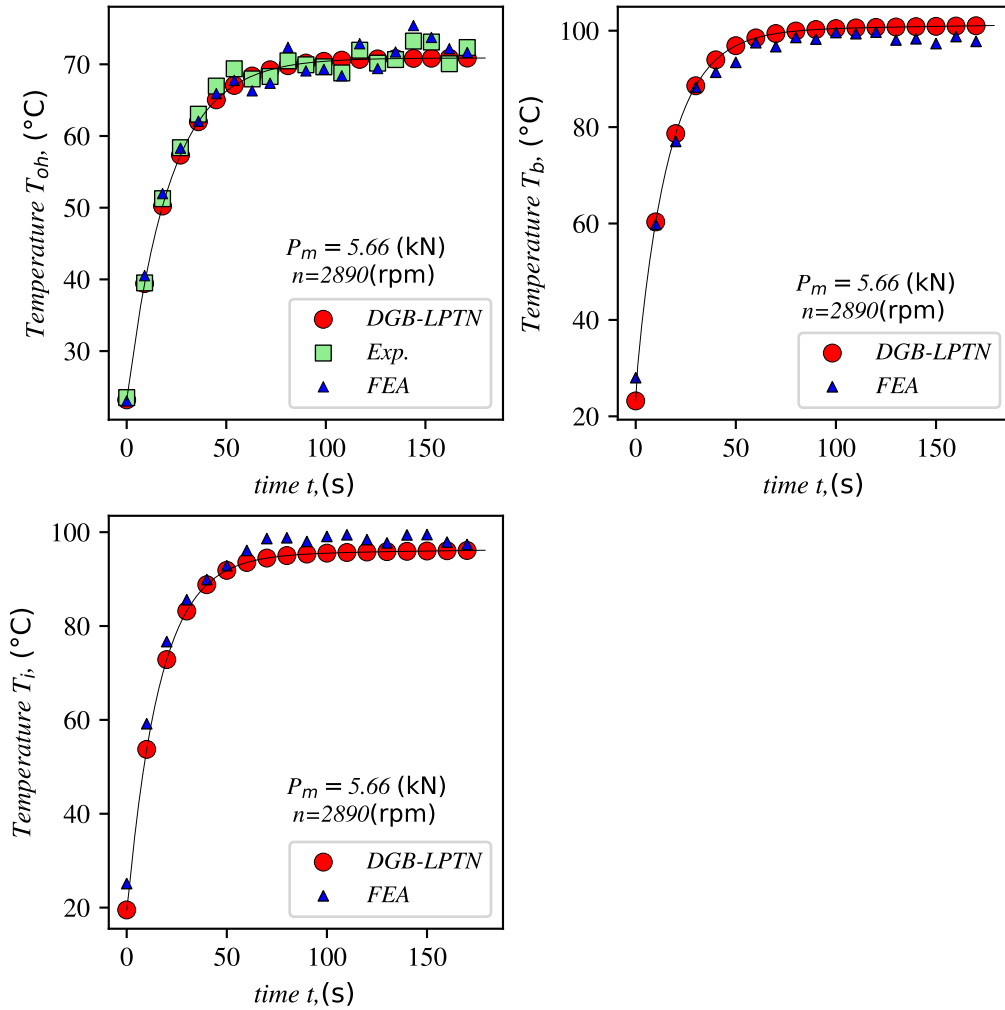


Figure 29: Dark Gray-Box LPTN  $P_m = 5.66$  kN,  $n = 2890$  rpm.

Under these conditions, it was observed that the values obtained by the Dark Gray-Box LPTN tend to be closer to the experimental and FEA results. For the housing/outer-ring subassembly, the experimental temperature measured by sensors 3S and 4S, was  $T_{oh} = 70.87$  °C, the Dark Gray-Box LPTN model temperature was equal to  $T_{oh} = 70.80$  °C, and the FEA simulation was equal to  $T_{oh} = 71.82$  °C. For the balls, the FEA simulation

yielded  $T_b = 97.98$  °C, while the Dark Gray-Box LPTN model gave  $T_{oh} = 101.07$  °C. For the inner-ring, the FEA simulation was equal to  $T_i = 98.86$  °C, and the Dark Gray-Box LPTN model yielded  $T_i = 96.15$  °C.

### Experiment 3)

In this experiment, the values of  $P_m = 3.99$  kN, and  $n = 2135$  rpm were set under normal conditions of operation, not exceeding the limit values. It was observed that the steady state conditions were reached at  $t = 720$  s, when there was not significant variation measured by the sensors 3S and 4S. The results are depicted in Fig. (30).

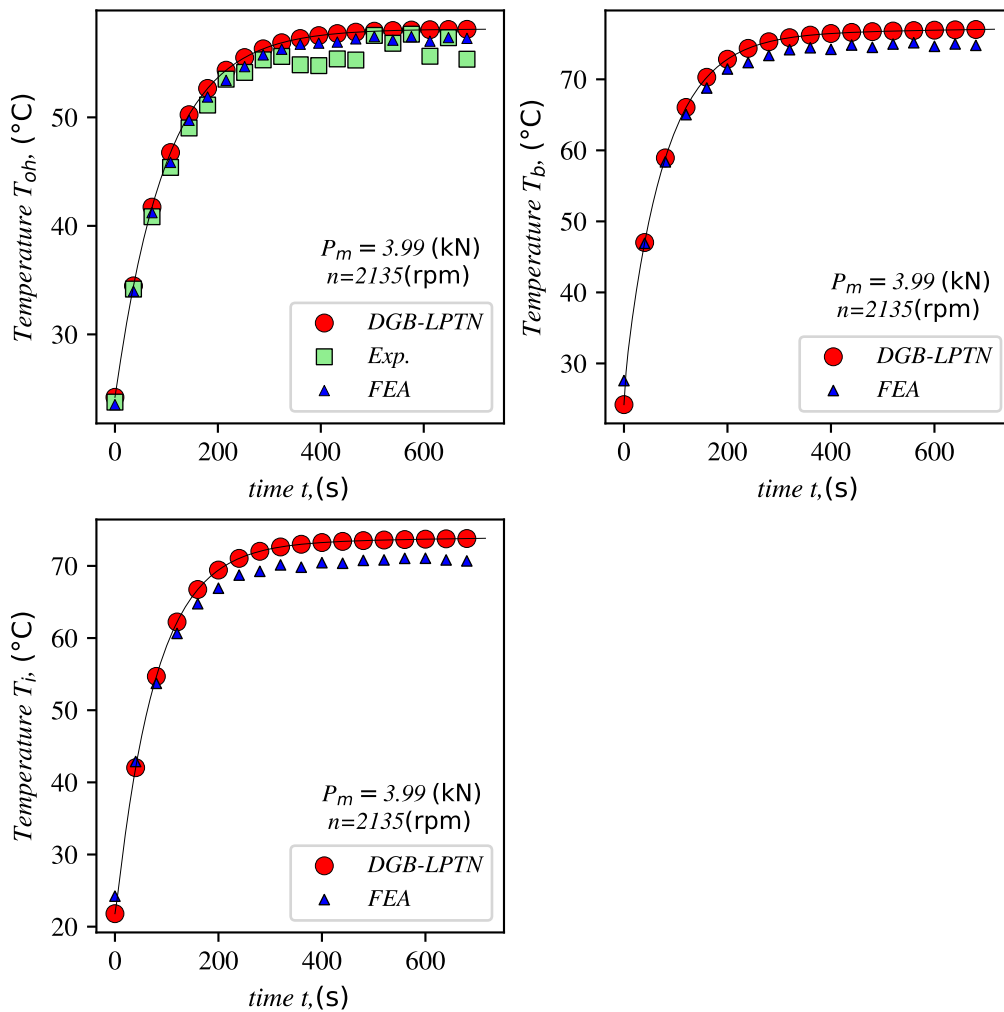


Figure 30: Dark Gray-Box LPTN  $P_m = 3.99$  kN,  $n = 2135$  rpm.

For the housing/outer-ring subassembly, the experimental temperature measured by sensors 3S and 4S, was  $T_{oh} = 55.41$  °C, the Dark Gray-Box LPTN model temperature was equal to  $T_{oh} = 58.11$  °C, and the FEA simulation was equal to  $T_{oh} = 57.15$  °C. For the balls, the FEA simulation yielded  $T_b = 74.97$  °C, while the Dark Gray-Box LPTN model

gave  $T_{oh} = 77.05$  °C. For the inner-ring, the FEA simulation was equal to  $T_i = 70.65$  °C, and the Dark Gray-Box LPTN model yielded  $T_i = 73.82$  °C.

To ensure that the Dark Gray-Box LPTN solved using the state space approach, can yield roughly accurate results, numerous experiments were conducted under different combinations of force  $P_m$  and rotational speed  $n$ . The dispersion and variability of the results are presented in Table 9.

Table 9: Dark Gray-Box LPTN in steady state conditions

Experiment	Force $P_m$ , (N)	Speed $n$ , (rpm)	time $t$ , (s)	EXP. °C	FEA °C	DGB-LPTN °C	Avg. °C	$s$	% $s$	% $SE$
Housing/Outer-ring										
1	578	625	200	36.0	35.35	34.28	35.21	0.71	2.02	1.16
2	5660	2890	200	70.87	71.82	70.8	71.16	0.47	0.66	0.38
3	3990	2135	720	55.41	57.15	58.11	56.89	1.12	1.97	1.14
4	1140	2764	120	35.86	35.94	35.05	35.62	0.4	1.12	0.65
5	3306	1757	600	48.7	49.85	51.1	49.88	0.98	1.96	1.13
6	2220	2010	360	47.5	46.65	46.25	46.8	0.52	1.11	0.64
7	4675	877	240	57.93	54.58	55.83	56.11	1.38	2.46	1.42
Balls										
1	578	625	200	-	43.19	40.88	42.04	1.15	2.74	1.93
2	5660	2890	200	-	97.99	101.075	99.53	1.54	1.55	1.09
3	3990	2135	720	-	74.98	77.05	76.02	1.03	1.35	0.96
4	1140	2764	120	-	41.58	43.16	42.37	0.79	1.86	1.32
5	3306	1757	600	-	61.1	63.6	62.35	1.25	2.0	1.42
6	2220	2010	360	-	51.59	53.94	52.76	1.17	2.22	1.57
7	4675	877	240	-	68.79	71.19	69.99	1.2	1.71	1.21
Inner-ring										
1	578	625	200	-	39.87	37.52	38.7	1.17	3.02	2.14
2	5660	2890	200	-	98.87	96.15	97.51	1.36	1.39	0.99
3	3990	2135	720	-	70.66	73.83	72.24	1.59	2.2	1.56
4	1140	2764	120	-	41.53	39.076	40.3	1.23	3.05	2.16
5	3306	1757	600	-	58.16	60.56	59.36	1.2	2.02	1.43
6	2220	2010	360	-	48.6	51.1	49.85	1.25	2.51	1.77
7	4675	877	240	-	70.29	67.89	69.09	1.2	1.74	1.23

### 4.3.3 Dark Gray-Box LPTN. Solutions in continuous time.

The model given in Eq.(39), was able to predict continuous-time solutions when the applied force  $P_m$  and the rotational speed  $n$  were not constant, thereby simulating real-time operations. These solutions were compared with experimental measurements, as well as with FEA simulations for the housing and outer-ring subassembly  $T_{oh}$ , and FEA simulations for the balls  $T_b$ , and inner ring  $T_i$ . To validate the model, the rotational speed  $n$  in the testing jig shown in Fig. (25) was held constant over a period of  $t = 42$  min. for each experiment. The forces were varied within the range of  $0.5 \leq P_m \leq 5.6$  kN. Each force was kept within a time of  $t = 2$  min.. For high accuracy in the analysis of the model,

the step time for the simulation was equal to  $\Delta t = 1$  s. To avoid pre-loading issues, the experiments began with a force  $P_m = 3.5$  kN kept during two minutes before starting the tests, so that misalignment effect in the jig could be neglected [16], [105]. The experiment was repeated changing the rotational speed  $n$ . To illustrate, three experiments will be shown, and the rest of the four experiments, due to the extent data information were statistically evaluated.

### Experiment 1)

In this experiment, the rotational speed was kept constant at  $n = 898$  rpm, and the dynamic radial load  $P_m$  was varied every two minutes, as illustrated in the inset of Fig. (31), to simulate real time operations. Temperature values were measured and recorded for the housing/ outer-ring assembly  $T_{oh}$ , the balls  $T_b$  and the inner-ring  $T_i$ , were compared with FEA simulations. The results of the thermal behavior are depicted in Fig. (31).

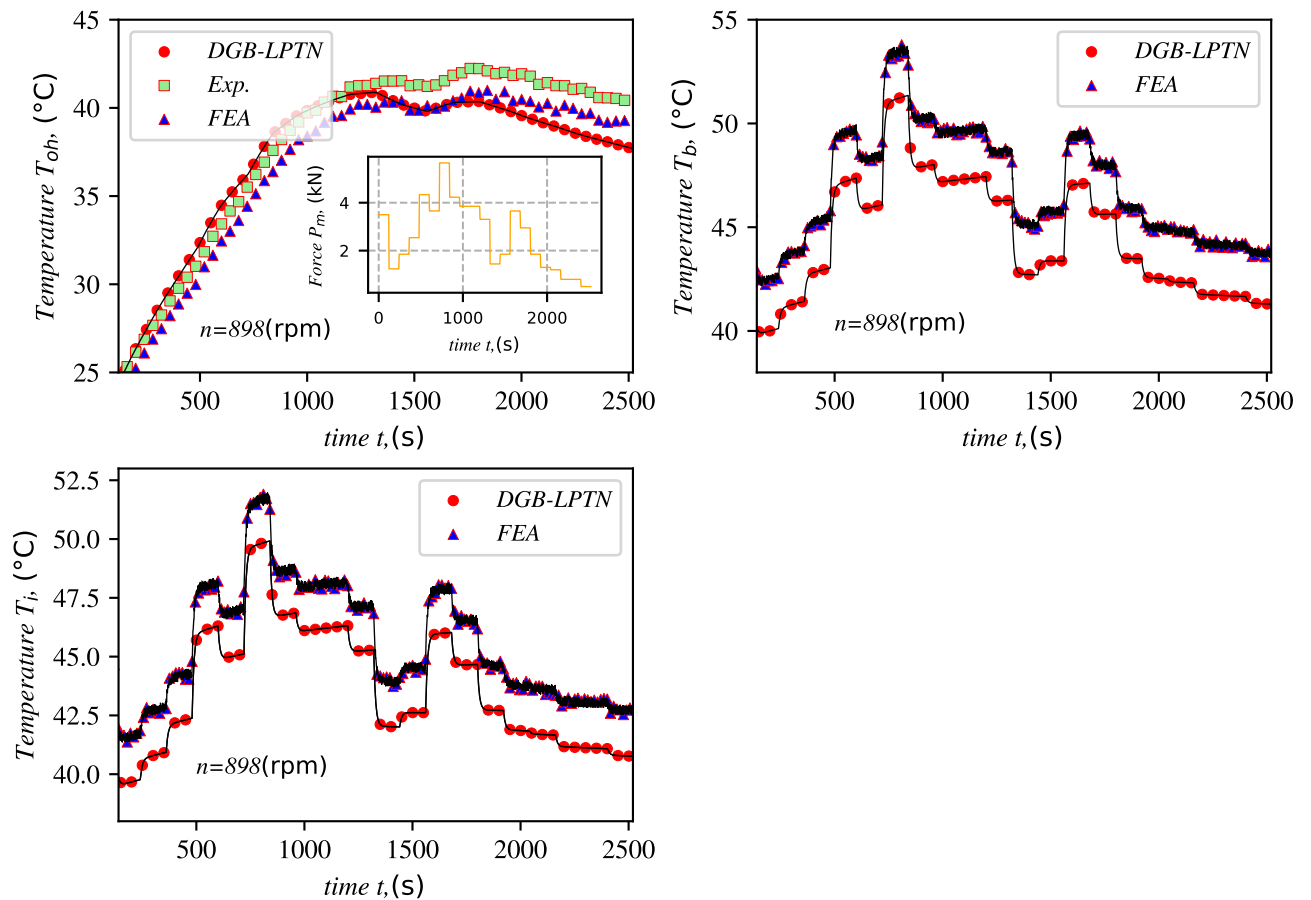


Figure 31: Dark Gray-Box LPTN. Continuous time solution  $n = 898$  rpm.

### Experiment 2)

In this experiment, the rotational speed was set to the maximum achievable speed in the test jig  $n = 2890$  rpm. As in the previous experiment, the force was varied following the same pattern. The thermal behavior is shown in Fig. (32).

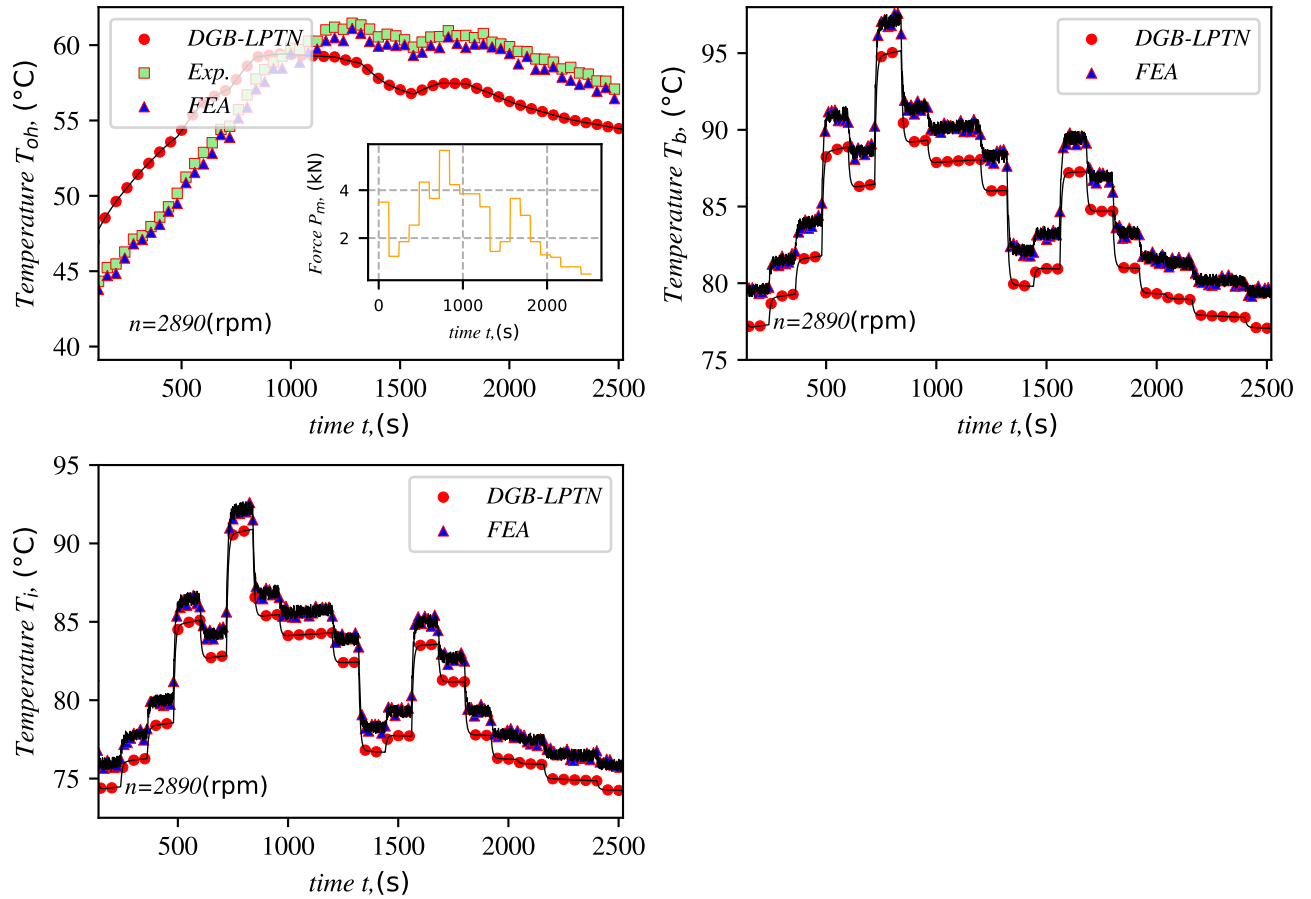


Figure 32: Dark Gray-Box LPTN. Continuous time solution  $n = 2890$  rpm.

### Experiment 3)

In this experiment, the rotational speed was set to an average working speed in the test jig,  $n = 1300$  rpm, the force  $P_m$  follows the same pattern as in Experiment 1 and Experiment 2. The thermal behavior is shown in Fig. (33).

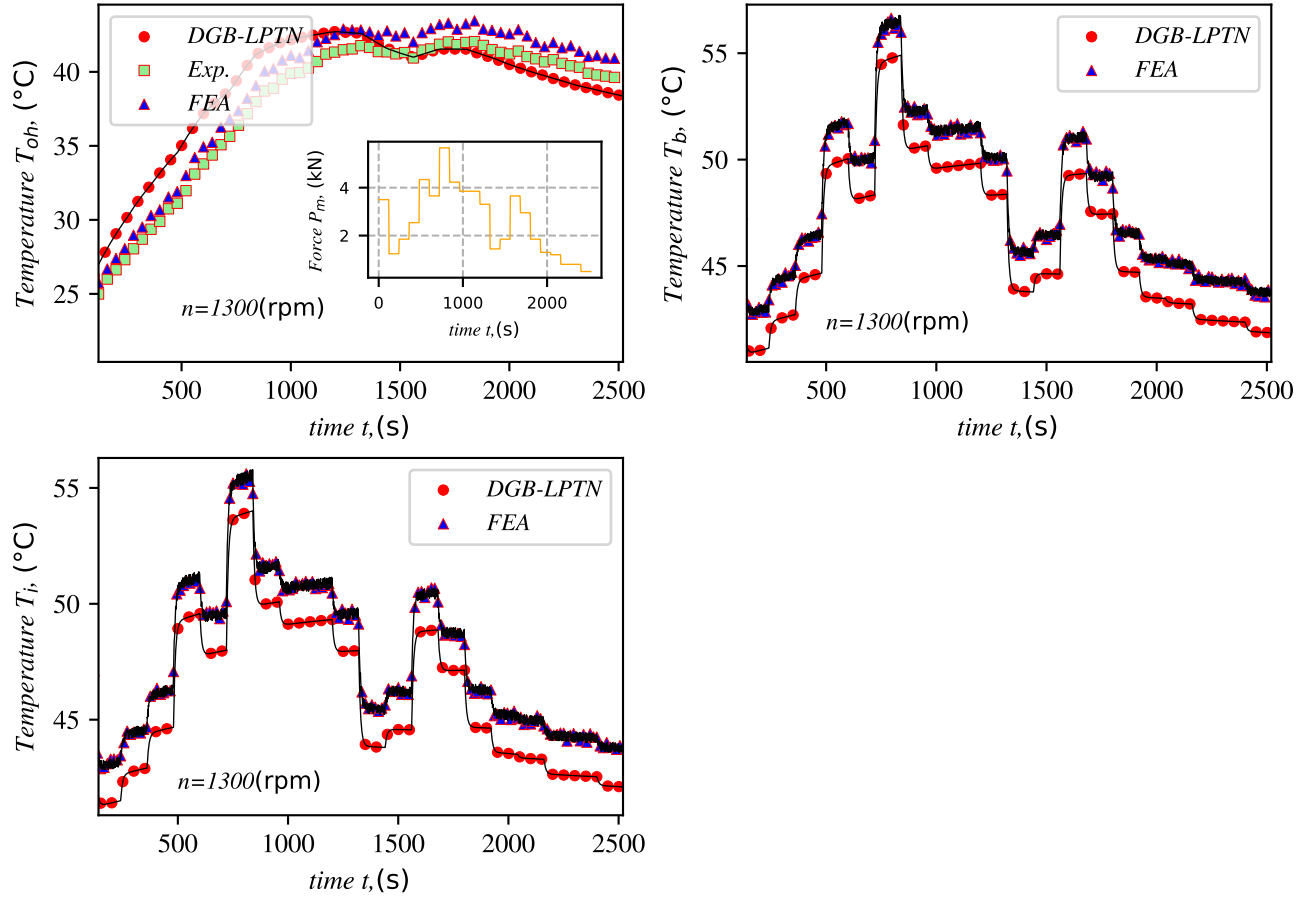


Figure 33: Dark Gray-Box LPTN. Continuous time solution  $n = 1300$  rpm.

Many experiments were evaluated in the same way as depicted in Figures Fig. (29), Fig. (30) and Fig. (31), using different values of rotational speed:  $n = 500$  rpm,  $n = 898$  rpm,  $n = 1300$  rpm,  $n = 1695$  rpm,  $n = 2491$  rpm, and  $n = 2890$  rpm. The tests were performed during the same time range, and the standard deviation was evaluated at each second  $s$ . The purpose of this statistical evaluation was to analyze the accuracy of the new model compared to experimental measurements and the FEA simulations. The dispersion results are illustrated in Fig. (34).

The maximum dispersion, equal to 2.28, was found when the rotational was equal to  $n = 2490$  rpm for the housing / outer-ring. The remaining values were found to range between 2.28 and 0.25, representing the maximum and minimum dispersion values. For the balls, the maximum dispersion, equal to 1.78, was observed at a rotational speed of  $n = 2093$  rpm. The dispersion ranged between 1.78 and 0.50 as the maximum and minimum dispersion values. For the inner-ring, the maximum dispersion, equal to 1.40,

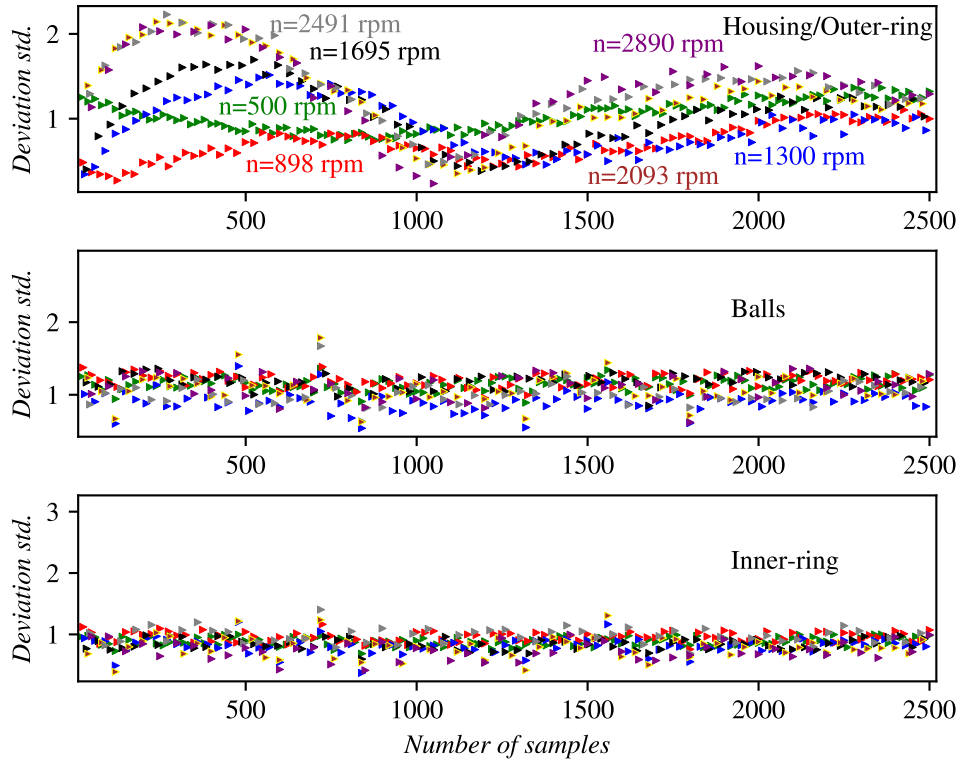


Figure 34: dispersion analysis for the components of the rolling bearing using the Dark Gray-Box LPTN model.

was found at a rotational speed of  $n = 2490$  rpm. The remaining values ranged between 1.40 and 0.37 as the maximum and minimum dispersion values.

#### 4.3.4 Conclusion of the chapter

I have introduced a new model based on the global identification of lumped parameter thermal networks, referred to as the Dark Gray-Box LPTN. The model comprises only five nodes, each representing a different part of the angular contact ball bearing and housing assembly. The development of the thermal network was based on the theory of heat transfer. The thermal model is capable of providing solutions under steady-state conditions and in continuous time. To solve the system in steady-state conditions, I chose to apply the state-space approach considering that the system is a multiple-input, multiple-output system. Numerous experiments were performed and the maximum standard deviation was equal to 2.34. The error was equal to 2.56 %. Continuous time operations were evaluated during 42 min. varying the force  $P_m$  and the rotational speed  $n$ . In this case the maximum dispersion was equal to 2.28.

## 5 Light Gray-Box and White-Box LPTN

This chapter presents the development of the Light Gray-Box LPTN and White-Box LPTN. By applying these models, the thermal fields for the housing  $T_h$ , outer-ring  $T_o$ , balls  $T_b$ , and inner-ring  $T_i$  can be determined. The Light Gray-Box LPTN incorporates the application of thermal contact resistances for static, moving, and combined heat sources based on the thermal resistance models for non-circular heat sources, proposed by Y.S. Muzychka et al. [93]. The White-Box LPTN offers a more versatile solution. In addition to using thermal resistances for moving heat sources, axial and radial flow analysis was incorporated in the cylindrical geometries using the Mellor formulation [94]. Both models are solved for steady-state conditions and continuous time.

### 5.1 Development of the LGB and WB thermal networks

The Light Gray-Box LPTN is a low-order thermal network (Low number of nodes), requiring low local discretization. However, the elements of the thermal network can be reliably divided (see Fig. 35), to ensure the independent analysis of each element in the representative model. The thermal material properties, geometrical characteristics, contact between the surfaces of the elements, and the formulation of the heat transfer theory form the basis for creating this thermal network. Furthermore, it enables the application of moving heat sources for the analysis of the thermal contact resistances between the inner ring and the balls and the outer ring and the balls. The Light Gray-Box LPTN was conceived as follows: 9 diffusion nodes, 10 thermal resistances and 3 heat sources.

The White-Box LPTN is a low order thermal network, with an accurate level of discretization. It enables the division of the inner elements into small nodes, hence enhancing the prediction of the thermal fields of the inner component of the bearing (see Fig. 36). This type of thermal network is built upon principles of heat transfer theory, the thermal properties of the materials, the geometrical constraints, thermal contact resistances for stationary, moving, and combined heat sources. Additionally, the thermal resistances

of the inner ring, outer ring and shaft were determined by the Mellor formulation [94] to ensure a more precise prediction of the thermal fields. The White Box LPTN was conceived as follows: 17 diffusion nodes, 20 thermal resistances and 3 heat sources.

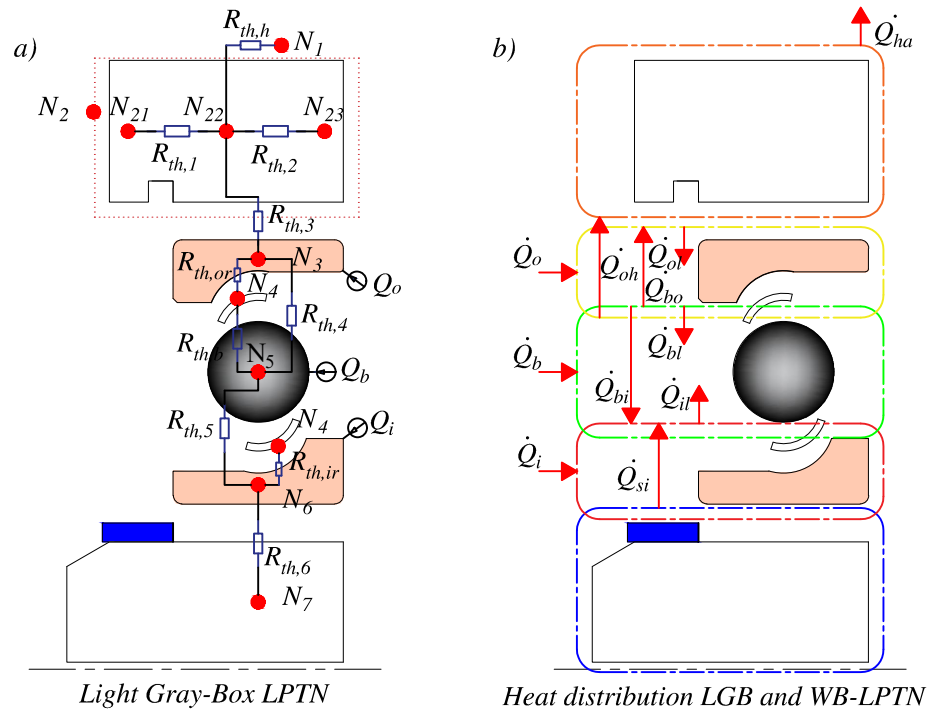


Figure 35: a) Light Gray-Box LPTN. b) Energy distribution through the bearing for the Light Gray-Box and White-Box LPTN.

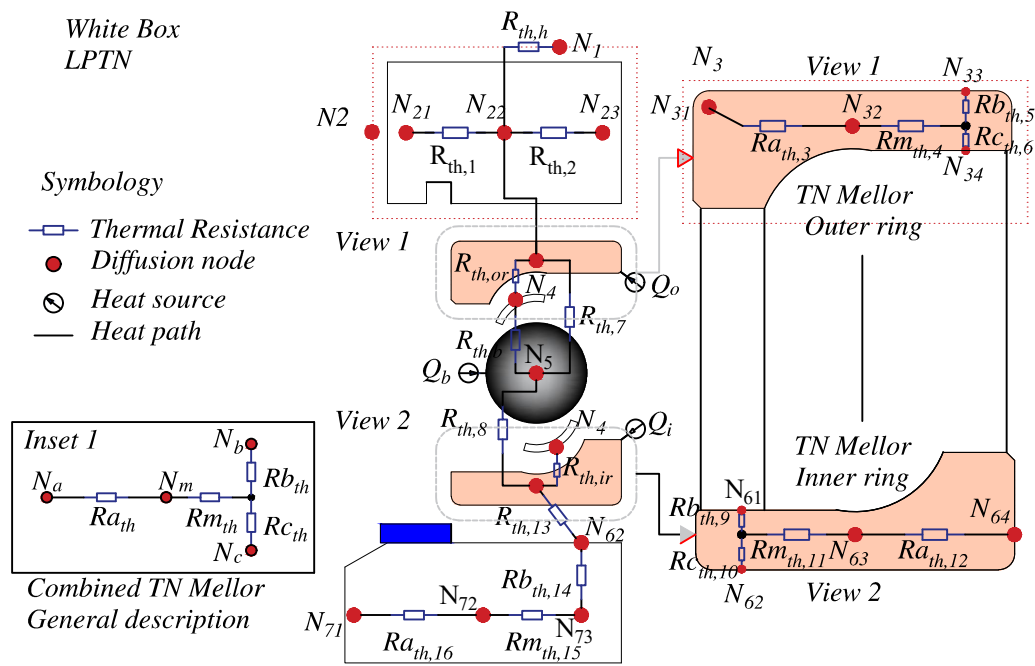


Figure 36: a) White-Box LPTN.

The nodal description of the Light Gray-Box LPTN and White-Box LPTN are given in

table 10.

Table 10: Nodal description of the Light Gray-Box and White-Box LPTN

Light Gray-Box LPTN							
Node	$N_1$	$N_{21}, N_{22}, N_{23}$	$N_3$	$N_4$	$N_5$	$N_6$	$N_7$
Source	<i>Ambient</i>	<i>housing</i>	<i>Outer-ring</i>	<i>Oil-film</i>	<i>Ball</i>	<i>Inner-ring</i>	<i>Shaft</i>
White-Box LPTN							
Node	$N_1$	$N_{21}, N_{22},$ $N_{23}$	$N_{31}, N_{32},$ $N_{33}, N_{34}$	$N_4$	$N_5$	$N_{61}, N_{62},$ $N_{63}, N_{64}$	$N_{71}, N_{72},$ $N_{73}$
Source	<i>Ambient</i>	<i>housing</i>	<i>Outer-ring</i>	<i>Oil-film</i>	<i>Ball</i>	<i>Inner-ring</i>	<i>shaft</i>

The thermal resistances are calculated based on the mathematical formulations provided in Section 3.9. The Equations are summarized in Table 11 .

Table 11: Thermal resistances of the Light Gray-Box and White-Box LPTN

Light Gray-Box LPTN			
Designation	Description	Type	Equation
$R_{th,h}$	housing and air	convection	Eq. (36)
$R_{th,1}, R_{th,2}$	housing	conduction	Eq. (28)
$R_{th,3}$	outer-ring	conduction	Eq. (28)
$R_{th,or}$	outer-ring and oil film	convection	Eq. (36)
$R_{th,b}$	ball and oil film	convection	Eq. (36)
$R_{th,4}$	outer-ring and ball	static	Eq. (30)
$R_{th,5}$	ball and inner-ring	moving real	Eq. (32)
$R_{th,ir}$	inner-ring and oil film	convection	Eq. (36)
$R_{th,6}$	inner-ring and shaft	conduction	Eq. (35)
White-Box LPTN			
Designation	Description	Type	Equation
$R_{th,h}$	housing and air	convection	Eq. (36)
$R_{th,1}, R_{th,2}$	housing	conduction	Eq. (28)
$R_{ath,3}, R_{mth,4}, R_{bth,5}, R_{cth,6}$	outer-ring	Mellor	Eq. (29)
$R_{th,or}$	outer-ring and oil film	convection	Eq. (36)
$R_{th,7}$	outer-ring and ball	static	Eq. (30)
$R_{th,b}$	ball and oil film	convection	Eq. (36)
$R_{th,8}$	ball and inner-ring	moving real	Eq. (32)
$R_{th,ir}$	inner-ring and oil film	convection	Eq. (36)
$R_{bth,9}, R_{cth,10}, R_{mth,11}, R_{ath,12}$	inner-ring	Mellor	Eq. (29)
$R_{th,13}$	inner-ring and shaft	conduction	Eq. (35)
$R_{bth,14}, R_{mth,15}, R_{ath,16}$	shaft	Mellor	Eq. (29)

## 5.2 Results and new contributions

### 5.2.1 Mathematical model of the Light Gray-Box LPTN

The thermal network was developed following the Kirchoff's law as explained in Section 4.3.1. The heat distribution was calculated following the heat path in Fig. (35b). The system of equation describing the Light Gray-Box LPTN is given in Eq. (41).

$$\begin{aligned}
m_h c_p \frac{dT_h}{dt} &= \frac{T_o - T_h}{\frac{1}{(R_{th,1} + R_{th,2})} + \frac{1}{R_{th,3}}} - \frac{T_h - T_a}{R_{th,h}} \\
m_o c_p \frac{dT_o}{dt} &= \dot{Q}_o - \frac{T_o - T_h}{\frac{1}{(R_{th,1} + R_{th,2})} + \frac{1}{R_{th,3}}} - \frac{T_o - T_b}{R_{th,4}} - \frac{T_o - T_l}{R_{th,or}} \\
Nm_b c_p \frac{dT_b}{dt} &= \dot{Q}_b + \frac{T_o - T_b}{R_{th,4}} - \frac{T_o - T_b}{R_{th,4}} - \frac{T_b - T_i}{R_{th,5}} - \frac{T_b - T_l}{R_{th,b}} \\
m_i c_p \frac{dT_i}{dt} &= \dot{Q}_i + \frac{T_b - T_i}{R_{th,5}} - \frac{T_i - T_s}{R_{th,6}} - \frac{T_i - T_l}{R_{th,ir}}
\end{aligned} \tag{41}$$

### 5.2.2 Mathematical model of the White-Box LPTN

Using the same procedure outlined in Section 5.2.1, the thermal model for the White-Box LPTN was developed following the heat path in Fig. (36b). The thermal network incorporates thermal resistances for static, moving, and combined heat sources. Additionally, the Mellor formulation was applied to determine the axial and radial heat distribution in the inner and outer-ring. The system of equation describing the White-Box LPTN is given in Eq. (42).

The heat distribution shown in Fig. (35b) for the Light Gray-Box and White-Box LPTN is detailed in Table 12.

$$\begin{aligned}
m_h c_p \frac{dT_h}{dt} &= \frac{T_o - T_h}{\frac{1}{(R_{th,1} + R_{th,2})} + \frac{1}{R_{th,mellor(or)}}} - \frac{T_h - T_a}{R_{th,h}} \\
m_o c_p \frac{dT_o}{dt} &= \dot{Q}_o - \frac{T_o - T_h}{\frac{1}{(R_{th,1} + R_{th,2})} + \frac{1}{R_{th,mellor(or)}}} - \frac{T_o - T_b}{R_{th,7}} - \frac{T_o - T_l}{R_{th,or}} \\
Nm_b c_p \frac{dT_b}{dt} &= \dot{Q}_b + \frac{T_o - T_b}{R_{th,7}} - \frac{T_b - T_i}{R_{th,8}} - \frac{T_b - T_l}{R_{th,b}} \\
m_i c_p \frac{dT_i}{dt} &= \dot{Q}_i + \frac{T_b - T_i}{R_{th,8}} - \frac{T_i - T_s}{\frac{1}{R_{th,13}} + \frac{1}{R_{th,mellor(ir)}}} - \frac{T_i - T_l}{R_{th,ir}} \\
m_s c_p \frac{dT_s}{dt} &= \frac{T_i - T_s}{\frac{1}{R_{th,13}} + \frac{1}{R_{th,mellor(ir)}}} - \frac{T_s}{\frac{1}{R_{th,mellor(is)}}}
\end{aligned} \tag{42}$$

where  $R_{th,mellor(or)} = \left( \frac{1}{R_{b_{th,5}}} + \frac{1}{R_{c_{th,6}}} + R_{m_{th,4}} \right) + \frac{1}{R_{b_{th,3}}}$ , is the Mellor thermal network for the outer-ring, and  $R_{th,mellor(ir)} = \left( \frac{1}{R_{b_{th,9}}} + \frac{1}{R_{c_{th,10}}} + R_{m_{th,11}} \right) + \frac{1}{R_{a_{th,12}}}$ , is the Mellor thermal network for the inner-ring, and  $R_{th,mellor(is)} = (R_{m_{th,15}} + R_{b_{th,14}} + R_{a_{th,16}})$ , is the Mellor thermal network of the shaft.

Table 12: Heat distribution in the Light Gray-Box and White-Box LPTN

Type of heat	Description
$\dot{Q}_{ha}$	Heat dissipated from the housing to the surroundings (W).
$\dot{Q}_o$	Heat generated by friction of the outer ring (W).
$\dot{Q}_{oh}$	Heat dissipated from the outer-ring to the housing (W).
$\dot{Q}_{ol}$	Heat dissipated from the outer-ring to the lubricant (W).
$\dot{Q}_b$	Heat generated by friction of the balls (W).
$\dot{Q}_{bo}$	Heat dissipated from the balls to the outer-ring (W).
$\dot{Q}_{bl}$	Heat dissipated from the balls to the lubricant (W).
$\dot{Q}_i$	Heat generated by friction of the inner-ring (W).
$\dot{Q}_{ib}$	Heat dissipated from the inner-ring to the balls (W).
$\dot{Q}_{il}$	Heat dissipated from the inner-ring to the lubricant film (W).
$\dot{Q}_{si}$	Heat dissipated from the shaft to the inner-ring (W).

### 5.2.2.1 Light Gray-Box LPTN model validation for stationary conditions

To validate the thermal model, the experimental measurements described in Section 4.3.2.1 were used for the housing  $T_h$  and outer-ring  $T_o$ . The FEA simulations described in Section 4.3.2.2 were used to compare the results of the thermal distribution along the moving elements: the balls  $T_b$  and inner-ring  $T_i$ . For illustration, I present two experiments which consist of varying the force  $P_m$  and the rotational speed  $n$ .

#### Experiment 1)

In this experiment, the rotational speed was kept constant at  $n = 625$  rpm, and the dynamic radial load at  $P_m = 0.578$  kN until steady state conditions were reached at  $t = 200$  s. The thermal behavior is illustrated in Fig. (37).

It is observable that for the housing, the thermal model reaches a maximum value of  $T_h = 32.90$  °C, meanwhile, the experimental measurements obtained by the sensors 1S and 2S and the FEA simulations gave a maximum value of approximately  $T_h = 31.50$  °C. For the outer-ring, the maximum temperature was  $T_o = 37.31$  °C, meanwhile the experimental measurements obtained by sensors 3S and 4S along with FEA simulations were approximately  $T_o = 36.15$  °C. For the balls, the FEA simulations and the thermal model shown almost no variation in the results reaching a temperature of  $T_b = 43.19$  °C. For the inner-ring, the maximum temperature of the thermal model was equal to  $T_i = 38.58$  °C, and the FEA simulation result was equal to  $T_i = 37.90$  °C.

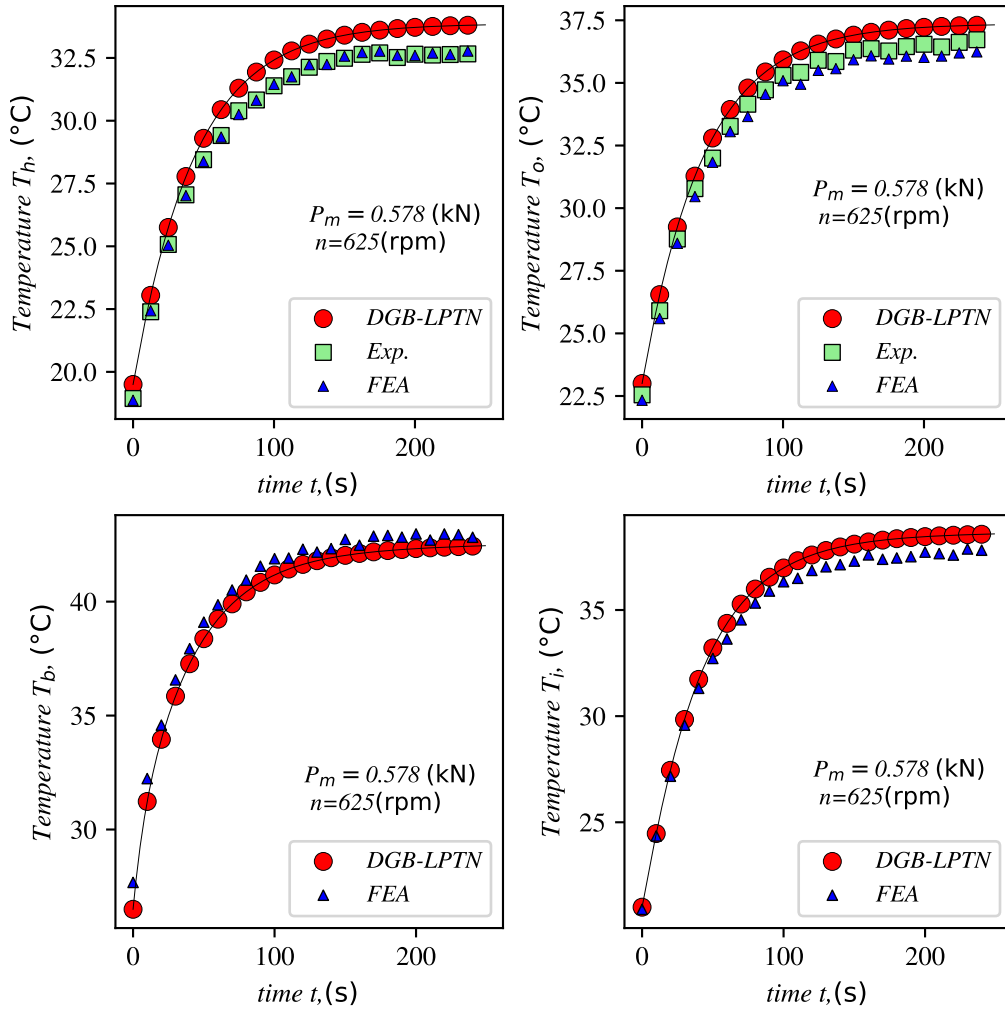


Figure 37: Light Gray-Box LPTN  $P_m = 0.578$  kN,  $n = 625$  rpm.

## Experiment 2)

In this experiment, the applied force was equal to  $P_m = 5.66$  kN, and the rotational speed was set at  $n = 2890$  rpm. It is observable that the thermal behavior for all the components are almost the same as the obtained by the experimental measurements and by the FEA simulations. The results are depicted in Fig. (38).

To ensure that the Light Gray-Box LPTN solved using the state space approach, can yield roughly accurate results, numerous experiments were conducted under different combinations of force  $P_m$  and rotational speed  $n$ . The dispersion and variability of the results are presented in Table 13.

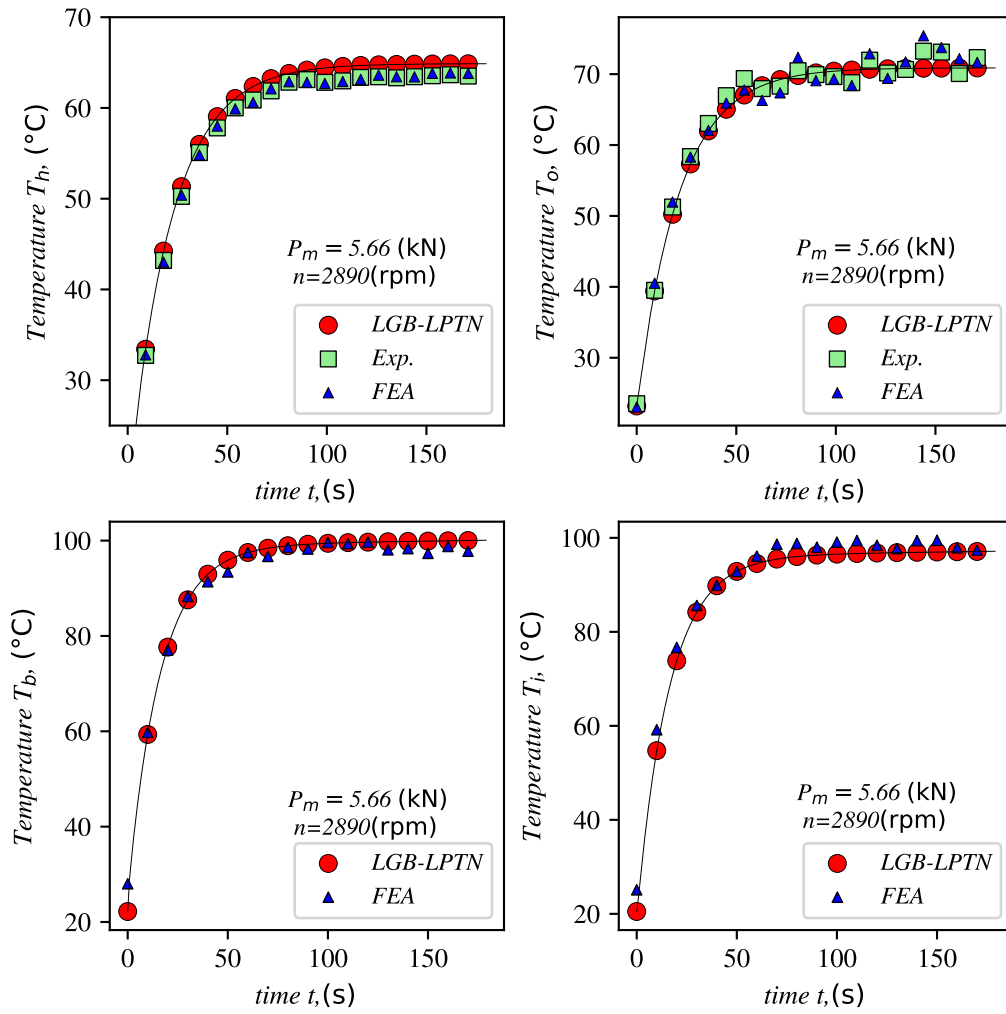


Figure 38: Light Gray-Box LPTN  $P_m = 5.66$  kN,  $n = 2890$  rpm.

Table 13: Light Gray-Box LPTN in steady state conditions

Experiment	Force $P_m$ , (N)	Speed $n$ , (rpm)	time $t$ , (s)	EXP. $^{\circ}\text{C}$	FEA $^{\circ}\text{C}$	DGB-LPTN $^{\circ}\text{C}$	Avg. $^{\circ}\text{C}$	$s$	% $s$	% $SE$
Housing										
1	578	625	200	32.9	33.01	33.82	33.24	0.41	1.23	0.71
2	5660	2890	200	70.87	71.82	70.87	71.19	0.45	0.63	0.36
3	3990	2135	720	49.86	49.13	50.26	49.75	0.47	0.94	0.55
4	1140	2764	120	35.79	35.74	35.06	35.53	0.33	0.93	0.54
5	3306	1757	600	48.7	46.62	48.2	47.84	0.89	1.86	1.07
6	2220	2010	360	47.5	45.6	47.05	46.72	0.81	1.73	1.0
7	4675	877	240	57.93	58.53	57.08	57.85	0.59	1.02	0.59
Outer-ring										
1	578	625	200	36.68	36.16	37.32	36.72	0.47	1.28	0.74
2	5660	2890	200	70.87	71.82	70.87	71.19	0.45	0.63	0.36
3	3990	2135	720	57.15	55.41	58.12	56.89	1.12	1.97	1.14
4	1140	2764	120	40.45	40.96	39.33	40.25	0.68	1.69	0.98
5	3306	1757	600	50.5	51.58	50.0	50.69	0.66	1.3	0.75
6	2220	2010	360	49.2	49.98	48.7	49.29	0.53	1.08	0.62
7	4675	877	240	59.5	57.72	59.0	58.74	0.75	1.28	0.74
Balls										
1	578	625	200	-	42.8	42.45	42.62	0.17	0.4	0.28
2	5660	2890	200	-	98.75	100.08	99.42	0.66	0.66	0.47
3	3990	2135	720	-	74.98	77.05	76.02	1.03	1.35	0.96
4	1140	2764	120	-	43.16	41.58	42.37	0.79	1.86	1.32
5	3306	1757	600	-	63.9	62.4	63.15	0.75	1.19	0.84
6	2220	2010	360	-	53.07	54.5	53.78	0.71	1.32	0.93
7	4675	877	240	-	69.22	70.8	70.01	0.79	1.13	0.8
Inner-ring										
1	578	625	200	-	37.97	38.59	38.28	0.31	0.81	0.57
2	5660	2890	200	-	98.07	97.15	97.61	0.46	0.47	0.33
3	3990	2135	720	-	70.66	73.83	72.24	1.59	2.2	1.56
4	1140	2764	120	-	41.53	39.08	40.3	1.23	3.05	2.16
5	3306	1757	600	-	60.51	61.81	61.16	0.65	1.06	0.75
6	2220	2010	360	-	51.05	52.35	51.7	0.65	1.26	0.89
7	4675	877	240	-	67.84	69.14	68.49	0.65	0.95	0.67

### 5.2.2.2 White-Box LPTN model validation for stationary conditions

As in the previous section, the same procedure was applied to validate the White-Box LPTN. In this case, I will present the results obtained when the force and the rotational speed were set to their maximum values,  $P_m = 5.66$  kN and  $n = 2890$  rpm, respectively.

#### Experiment 1)

It is observable in Fig. (39) that the thermal behavior predicted by the White-Box LPTN aligns closely with the results obtained by the experimental measurements and FEA simulations. For the housing, the thermal behavior  $T_h$  has a dispersion of 0.08 in comparison between the experimental measurements and the FEA simulations. For the outer-ring  $T_o$  the dispersion was 0.39. In the case of the balls  $T_b$ , the dispersion was 0.16. Finally, for the inner-ring  $T_i$ , the dispersion was 0.71.

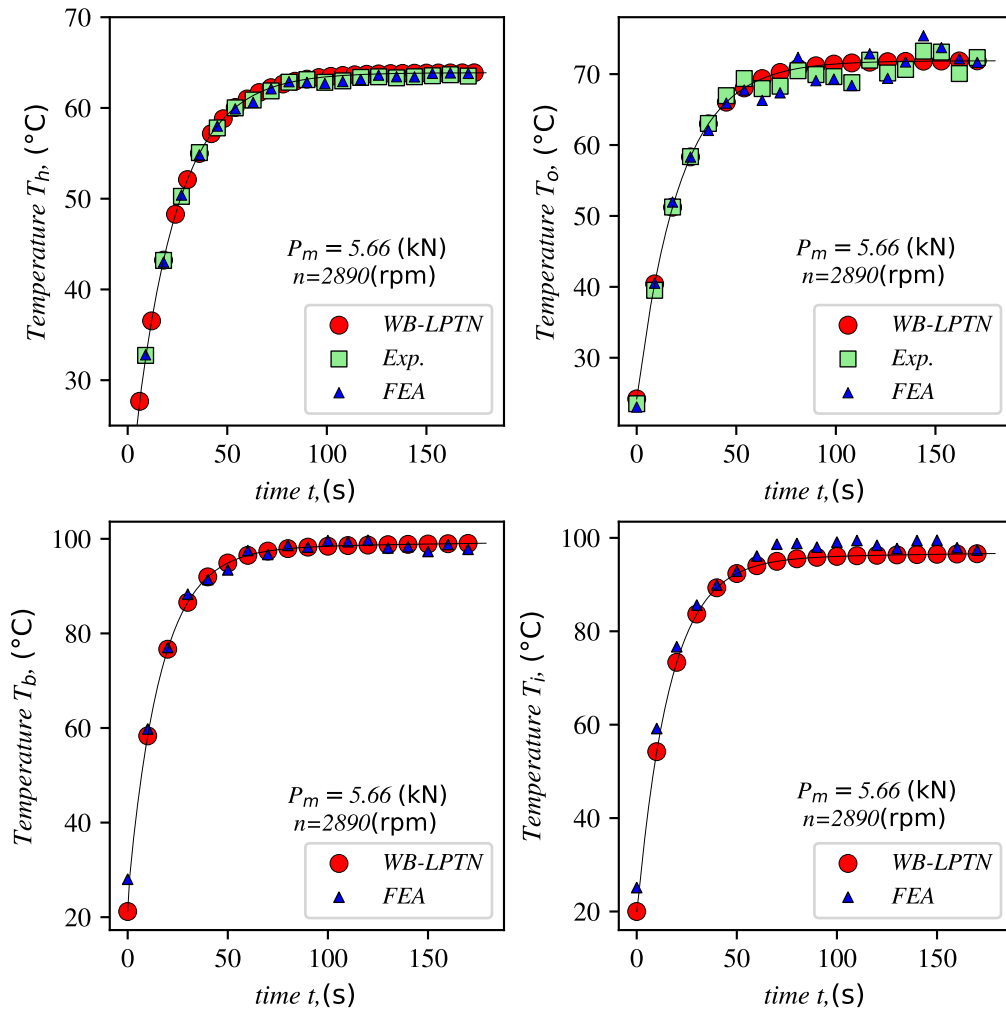


Figure 39: White Gray-Box LPTN  $P_m = 5.66$  kN,  $n = 2890$  rpm.

For all the experiments given in Table 14, it is observable that the dispersion is less than 0.71, giving an error of 0.52 % for the inner-ring.

Table 14: White-Box LPTN in steady state conditions

Experiment	Force $P_m$ , (N)	Speed $n$ , (rpm)	time $t$ , (s)	EXP. °C	FEA °C	DGB-LPTN °C	Avg. °C	$s$	% $s$	% $SE$
Housing										
1	578	625	200	32.9	33.01	32.81	32.91	0.08	0.24	0.14
2	5660	2890	200	63.5	63.78	63.87	63.72	0.16	0.25	0.14
3	3990	2135	720	50.59	50.15	50.12	50.29	0.21	0.42	0.24
4	1140	2764	120	35.84	35.87	35.81	35.84	0.02	0.06	0.03
5	3306	1757	600	48.7	48.9	48.7	48.77	0.09	0.18	0.11
6	2220	2010	360	47.5	47.2	47.0	47.23	0.21	0.44	0.26
7	4675	877	240	57.93	58.1	57.5	57.84	0.25	0.43	0.25
Outer-ring										
1	578	625	200	36.16	36.85	36.57	36.53	0.28	0.77	0.44
2	5660	2890	200	72.8	72.53	71.87	72.4	0.39	0.54	0.31
3	3990	2135	720	57.15	55.41	56.12	56.23	0.71	1.26	0.73
4	1140	2764	120	40.45	40.96	40.33	40.58	0.27	0.67	0.38
5	3306	1757	600	51.0	51.58	50.95	51.18	0.29	0.57	0.33
6	2220	2010	360	49.6	49.98	49.3	49.63	0.28	0.56	0.33
7	4675	877	240	57.5	57.72	57.2	57.47	0.21	0.37	0.21
Balls										
1	578	625	200	-	42.8	42.95	42.88	0.08	0.19	0.13
2	5660	2890	200	-	98.75	99.08	98.92	0.16	0.16	0.11
3	3990	2135	720	-	74.98	75.05	75.02	0.03	0.04	0.03
4	1140	2764	120	-	43.2	43.33	43.26	0.06	0.14	0.1
5	3306	1757	600	-	64.1	63.9	64.0	0.1	0.16	0.11
6	2220	2010	360	-	52.5	52.1	52.3	0.2	0.38	0.27
7	4675	877	240	-	70.5	70.1	70.3	0.2	0.28	0.2
Inner-ring										
1	578	625	200	-	37.97	38.59	38.28	0.31	0.81	0.57
2	5660	2890	200	-	98.07	96.65	97.36	0.71	0.73	0.52
3	3990	2135	720	-	70.66	70.73	70.69	0.04	0.06	0.04
4	1140	2764	120	-	41.26	41.33	41.3	0.04	0.1	0.07
5	3306	1757	600	-	60.51	60.2	60.36	0.15	0.25	0.18
6	2220	2010	360	-	51.05	50.85	50.95	0.1	0.2	0.14
7	4675	877	240	-	67.84	67.5	67.67	0.17	0.25	0.18

### 5.2.3 Light Gray-Box LPTN. Solutions in continuous time.

To validate the thermal models simulating real-time operations, the procedure described in Section 4.3.3 was applied. The rotational speed  $n$  was kept constant, while the force  $P_m$  was varied within the range  $0.5 \leq P_m \leq 5.6$  kN. The thermal model includes the concept of moving heat sources that occur between the inner-ring of the bearing and the balls using Eq.(32). The shaft and the inner-ring were considered as a cylindrical set of layers, which transfer heat by conduction described using Eq. (35). Experiments were performed, prove that the model can describe the thermal behavior of the bearing, and in comparison with the Dark-Gray Box LPTN is more accurate. To illustrate, I depict in Fig. (40), the thermal behavior under the maximum rotational speed that can be

performed by the testing JIG described in Fig. (25).

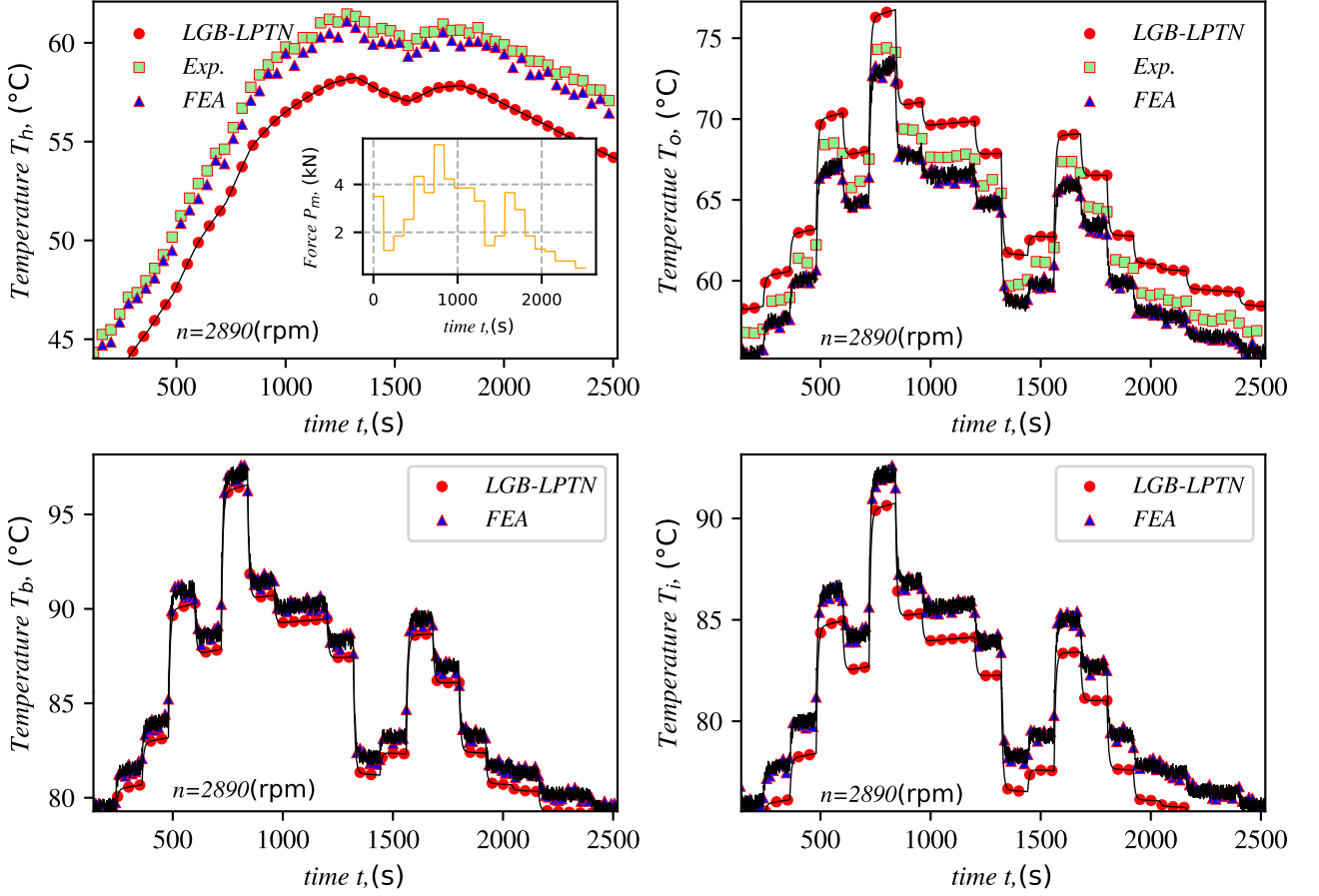


Figure 40: Light Gray-Box LPTN. Continuous time solution  $n = 2890$  rpm.

The Light Gray-Box LPTN model was validated performing several experiments. Given the vast amount of information, not all the experiments are depicted in this document. Instead, statistical analysis was implemented to show and demonstrate the accuracy of the model, as shown in Fig (41).

For the housing  $T_h$  the maximum dispersion was 1.52, with the remaining values within the range 0.73 – 1.52. For the outer-ring  $T_o$ , the maximum dispersion was equal to 2.56, while the remaining values are within the range 0.25 – 2.56. For the balls  $T_b$ , the maximum dispersion value was equal to 2.97. Although, the value is higher than the maximum dispersion obtained by the Dark Gray-Box LPTN. However, the rest of the values are minimal in comparison to those obtained by the Dark Gray-Box LPTN. Finally, for the inner-ring  $T_i$ , the maximum value of dispersion was equal to 1.34, with the remaining values within the range 0.37 – 1.34.

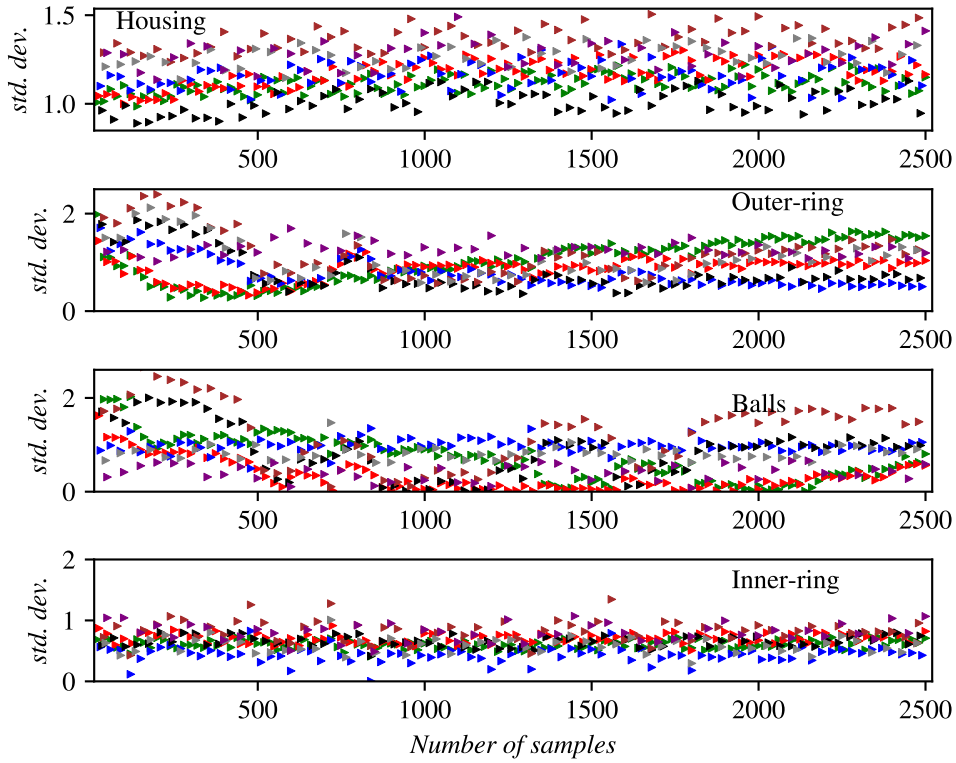


Figure 41: dispersion analysis for the components of the rolling bearing using the Light Gray-Box LPTN model.

#### 5.2.4 White-Box. Solutions in continuous time

To validate the White-Box LPTN simulating real time operations in continuous time, the procedure described in Section 5.2.3 was performed. The thermal network is complete, including static, moving and combined heat sources. Furthermore, the implementation of the Mellor's formulation for cylindrical surfaces has allowed the calculation of heat flow in radial and axial directions for the outer-ring, inner-ring, and shaft. Several experiments have been performed, showing good agreement with the experimental and FEA simulations. The thermal network showed a remarkable improvement in the prediction of the thermal behavior of the angular contact ball bearing, in comparison with the Dark Gray-Box and Light Gray-Box LPTN. I will present two experiments at the lowest speed and maximum speed, to show the validity of the model.

##### Experiment 1)

The experiment present the results of the White-Box LPTN at a rotational speed  $n = 898$  rpm. For the housing  $T_h$ , it is observable that the curve follows the same pattern as those obtained by the experimental and FEA simulations. Furthermore, the FEA simulations and the White-Box show significant overlap, indicating good agreement. For the outer-ring  $T_o$ , the measurements closely match with the White-Box LPTN. Additionally,

there is an overlap between the FEA simulations and the model itself. For the balls  $T_b$ , the pattern aligns with the FEA simulations with a slight difference of less than  $1^\circ\text{C}$ . Finally for the inner-ring, the model overlaps with the FEA simulations in most cases. The difference is less than  $1^\circ\text{C}$ . The results are shown in Fig. (42).

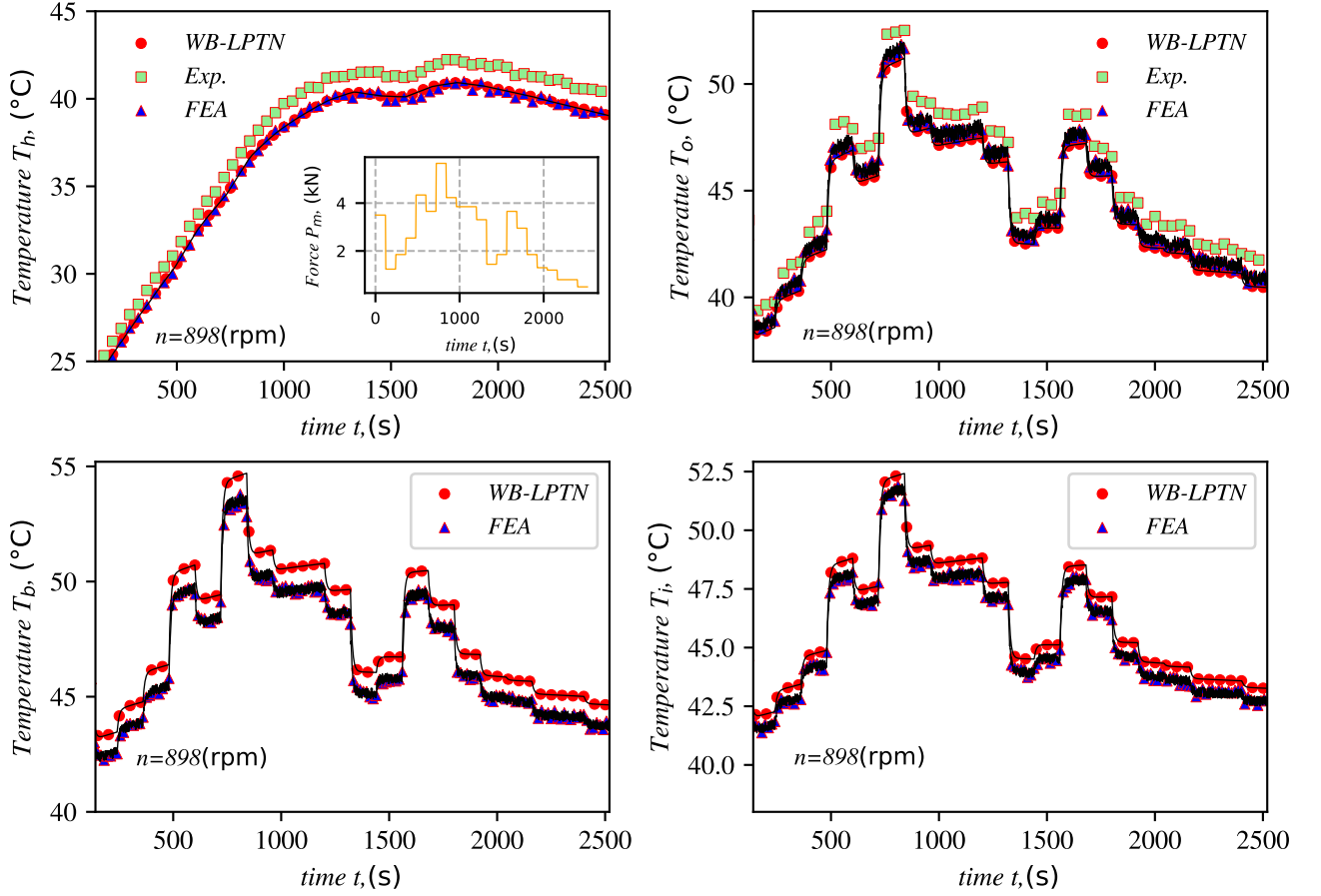


Figure 42: White-Box LPTN. Continuous time solution  $n = 890$  rpm.

## Experiment 2)

The experiment presents the results of the White-Box LPTN at a rotational speed  $n = 2890$  rpm. For the housing  $T_h$ , the model aligns more closely with the experimental measurements. However, the overall pattern consistent across the FEA, experimental and the model results. For the outer-ring  $T_o$ , the model is more aligned to the experimental measurements than with the FEA simulations. However the difference is not significant. For the balls  $T_b$ , and for the inner-ring  $T_i$ , the pattern between the FEA simulations and the model are the same, with a slightly higher values observed for the White-Box LPTN. The results are shown in Fig. (43).

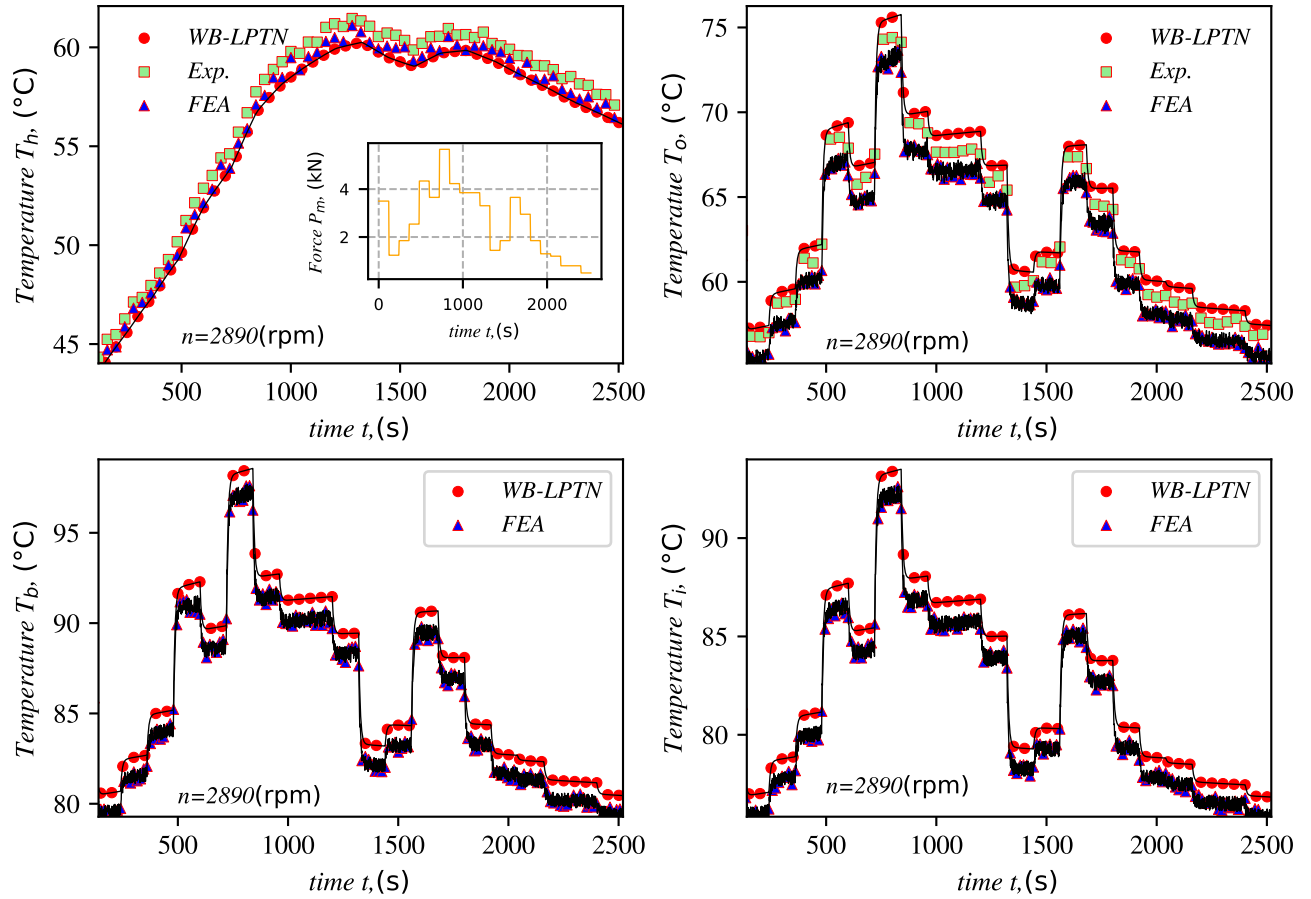


Figure 43: White-Box LPTN. Continuous time solution  $n = 2890$  rpm.

Statistical analysis was performed to show the dispersion of the thermal model in comparison to the FEA, and experimental measurements. In comparison to the Dark Gray-Box LPTN, and the Light Gray-Box LPTN, the White-Box LPTN shows more accurate results. For the housing  $T_h$ , the maximum dispersion was 0.67, the remaining values are within the range 0.21 – 0.68. For the outer-ring  $T_o$ , the maximum dispersion was 1.33, the remaining values are within the range 0.29 – 1.33. For the balls  $T_b$ , the maximum dispersion was 1.04, the remaining values are within the range 0.0 – 1.04. Finally, for the inner-ring  $T_i$ , the maximum dispersion was 0.99, the remaining values are within the range 0.0 – 0.99. The graphic of dispersion is given in Fig. (44).

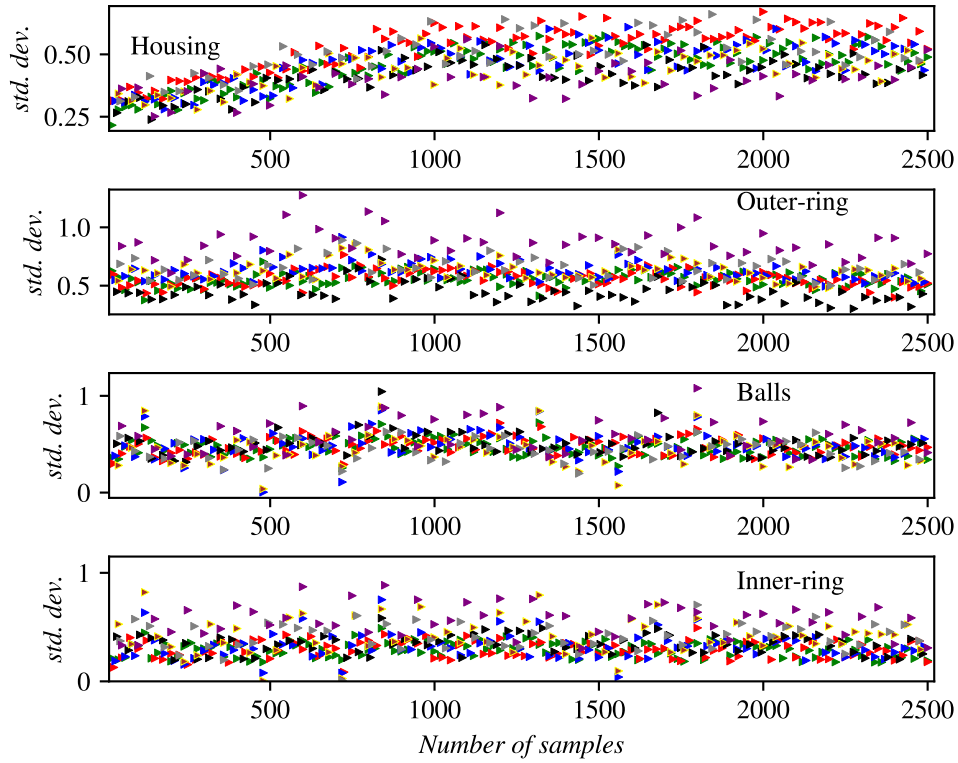


Figure 44: Dispersion analysis for the components of the rolling bearing using the White-Box LPTN model.

### 5.2.5 Conclusion of the Chapter

I have introduced two thermal models, referred as the Light Gray-Box LPTN and White-Box LPTN. The light Gray-Box LPTN, comprises nine diffusion nodes. This thermal network incorporates the contact resistances of elliptical contact for stationary, moving, and combined heat sources, based on the investigation by Y. S. Muzychka et al. [93]. The White-Box LPTN is a more complex thermal model, which comprises 17 diffusion nodes. This thermal Network utilizes the concept of contact resistances described by [93]. Furthermore, the model incorporates the Mellor's formulation [76], [94]. Both models were solved for steady-state and continuous-time operations. Under steady-state conditions, the maximum percentage deviation was 2.2 % and 1.26 %, for the Light Gray-Box and White-Box LPTN, respectively. In continuous-time, the maximum dispersion was 2.97 for the Light Gray-Box LPTN, and 1.33 for the White-Box LPTN. Both thermal networks exhibit improved performance compared to the Dark Gray-Box LPTN. Among the models, the White-Box LPTN demonstrates the highest accuracy.

## 6 New scientific results and contributions

The following chapter presents the new contributions derived throughout this research process. The dissertation is divided into six chapters to facilitate readability and comprehension for the reader, beginning from the introduction of the topic, followed by the research review. Subsequently, the description of the concepts and mathematical formulations necessary to implement in the thermal models are detailed. After this extensive process, the thermal models presented in Chapters Five and Six were developed.

Based on the content of this document, the following theses are derived:

### 6.1 Theses

**T1.** I have modeled the thermal losses and the heat transfer of an angular contact ball bearing, specifically for spindle units. The heat transfer was based on the analysis of frictional moments resulting from the dynamic equivalent radial load. I separated the bearing elements housing, outer-ring, balls, and inner-ring into individual control volumes and applied the concept of heat partition for rolling and sliding elastohydrodynamic contacts [63]. This methodology enabled the treatment of the bearing elements as individual heat sources. I observed that the thermal losses and the heat transfer govern the steady conditions of the system. To solve the thermal system, I employed an analogy between electrical and thermal systems. Based on this analogy, I implemented the state-space approach, considering the thermal model of the bearing as a MIMO (multiple-input - multiple-output) system. The system showed the following features:

- a) The thermal model was controllable and observable. However, for this research, the model's importance lies in its observability, as the thermal behavior can be predicted.
- b) The State-space approach was applied to the thermal models: Dark Gray-Box, Light Gray-Box, and White-Box LPTN. I found that the steady state solutions closely match with the experimental and FEA simulations. For the Dark Gray-Box, and Light Gray-Box LPTN, the maximum percentage of dispersion was 3.05 %. For the White-Box

LPTN, the maximum percentage of dispersion was 1.26 %.

Related publications: [P1].

**T2.** I have implemented the formulations for thermal resistance models for non-circular moving heat sources [93]. I found that more accurate results are obtained when the contact between the elements of the angular contact ball bearing are realistic. Specifically, the contact between the outer-ring and the balls must be considered as a combined heat source, comprising both, stationary and moving heat sources. For the contact between the balls and the inner-ring, I found that the best approach is to treat the thermal contact as a moving heat source. When these considerations were implemented, the results improved drastically, closely matching with the experimental and FEA simulations with a dispersion of less than 1.04. Throughout this research, it was seen that, due to the small contact areas between the elements of the bearing (analyzed using the Hertzian contact theory), the models remain consistent and yield accurate results when assuming iso-flux distribution.

Related publications: [P2], [P3].

**T3.** I have created a new thermal model based on the global identification of Lumped parameter thermal networks, called Dark Gray-Box LPTN. I found that the model yields good thermal solutions if the conceptualizations of diffusion nodes and heat paths are clearly grounded in heat transfer theory. The model is efficient for both, steady and continuous-time solutions, considering that the number of nodes are no more than five. To improve the model's accuracy, I observed that implementing Walther's approach for the elastohydrodynamic lubrication, enhances the results by 5 %. The Dark Gray-Box LPTN model is designed to assist engineering of spindle systems in the early stage of development, without relying on complicated, costly, and time-consuming methods.

Related publications: [P3].

**T4.** I have created a thermal model called Light Gray-Box LPTN. The model consists of nine diffusion nodes. The nodes and heat paths implemented in the thermal network, allowed me to account for static thermal resistances for the housing, combined thermal contact resistances for the outer-ring and balls and moving heat sources for the balls and inner-ring. The thermal contact resistances were calculated for isoflux heat distribution.

The heat transfer by convection was analyzed between the housing and the surroundings as a solid cylinder in air cross-flow at low speeds. I found that the discrepancy between the thermal model and the experimental and FEA simulations was less than 2.97 for continuous-time solutions. The model yields accurate results compared to experimental and FEA simulations.

Related publications: [P2], [P4], [P5] .

**T5.** I have created a thermal model called White-Box LPTN. The thermal network incorporates the concept of thermal resistances for static, moving, and combined heat sources, similar to the Light Gray-Box LPTN. Additionally, the thermal network incorporates the Mellor's formulation. I have found that through the application of the Mellor's formulation for cylindrical shapes (inner-ring, outer-ring and shaft), the axial and radial flow can be included in the mathematical formulation, enhancing the accuracy of the thermal model. Based on the statistical analysis, it is evident that the levels of discrepancy decreased significantly. For the housing  $T_h$ , the maximum dispersion was 0.67. For the outer-ring  $T_o$ , was 1.33. For the balls  $T_b$ , the dispersion was 1.04, and for the inner-ring  $T_i$ , the maximum dispersion was 0.99. The model matches closely to the experimental and FEA results.

Related publications: [P1], [P2], [P5], [P6] .

## 6.2 Related publications

**P1.** Sebastian Cabezas, György Hegedűs, Péter Bencs, "A New Thermal Model of an Angular Contact Ball Bearings, in a Standard Arrangement, subjected to Radial Loads, based on State Variables and Control Volumes", Acta Polytechnica Hungarica, 2024, Vol. 21 (4).

Index: **Scopus**, Rank (**Q2**)

**P2.** Sebastian Cabezas, György Hegedűs, Péter Bencs, "Thermal contact resistance for stationary and moving heat sources in angular contact ball bearings", Tribology and Materials, 2023, Vol. 21 (3).

Index: **Scopus**.

**P3.** Sebastian Cabezas, György Hegedűs, Péter Bencs, "Dark Gray Box Lumped Parameter Thermal Network for High Speed Spindle Rolling Bearings", IEEE 21st Jubilee International Symposium on Intelligent Systems and Informatics, 2023.

Index: **Scopus**.

**P4.** Sebastian Cabezas, György Hegedűs, Péter Bencs, "Transient heat convection analysis of a single rod in air cross-flow", Pollack Periodica, 2023, Vol. 18 (2).

Index: **Scopus**, Rank (**Q3**)

**P5.** Sebastian Cabezas, Dániel Tóth, György Hegedűs, Péter Bencs, "Thermal Model of a Ball Bearing using the State-Space approach and Light Gray-Box Lumped Parameter Thermal Network", Power System Engineering 2023, 2023, Vol. 5 (383).

**P6.** Sebastian Cabezas, György Hegedűs, Péter Bencs, "Thermal Experimental and Numerical Heat Transfer Analysis of a Solid Cylinder in Longitudinal Direction", Analecta Technica Szegedinensia, 2023, Vol. 17 (1).

**P7.** Mohammad Alzghoul, Sebastian Cabezas, Attila Szilágyi "Dynamic modeling of a simply supported beam with an overhang mass", Pollack Periodica, 2022, Vol. 17 (2).

Index: **Scopus**, Rank (**Q3**)

**P8.** Sebastian Cabezas, Attila Szilágyi "Thermal Behavior in Cnc Machine-Tools", Design of Machines and Structures, 2020, Vol. 10 (2).

**P9.** Sebastian Cabezas, Attila Szilágyi "Thermal and Structural Simulations of a Cnc Turning Center", Design of Machines and Structures, 2020, Vol. 10 (2).

## References

- [1] Jin Cheng et al., “Thermo mechanical coupling analysis of a high speed actuating mechanism based on a new thermal contact resistance model”, *Applied Thermal Engineering*, 140, (Jul. 2018), pp. 487–497, DOI: <https://doi.org/10.1016/j.applthermaleng.2018.05.063>.
- [2] Igor Alexeevich Zverev et al., “Thermal model of High Speed Spindle Units”, *KSME International Journal*, 117(5), (May. 2003), pp. 668–678, DOI: <https://doi.org/10.1007/BF02983862>.
- [3] Jin-Huang Huang et al., “An inverse method for estimating heat sources in a high speed spindle”, *Applied Thermal Engineering*, 105, (Jul. 2016), pp. 65–76, DOI: <http://dx.doi.org/10.1016/j.applthermaleng.2016.05.123>.
- [4] Jialan Liu et al., “Thermal structure interaction characteristics of a high speed spindle bearing system”, *International Journal of Machine Tools and Manufacture*, 137, (Feb. 2019), pp. 42–57, DOI: <https://doi.org/10.1016/j.ijmachtools.2018.10.004>.
- [5] Teng Liu et al., “Analytical modeling for thermal errors of motorized spindle unit”, *International Journal of Machine Tools and Manufacture*, 112, (Jan. 2017), pp. 53–70, DOI: <https://doi.org/10.1016/j.ijmachtools.2016.09.008>.
- [6] Srinivas N. Grama and Ashvarya Mathur and Ashok N. Badhe, “A model based cooling strategy for motorized spindle to reduce thermal errors”, *International Journal of Machine Tools and Manufacture*, 132, (Sep. 2018), pp. 3–16, DOI: <https://doi.org/10.1016/j.ijmachtools.2018.04.00>.
- [7] X. Li et al., “Study on the influence of thermal characteristics of rolling bearings and spindle resulted in condition of improper assembly”, *Applied Thermal Engineering*, 114, (Mar. 2017), pp. 221–233, DOI: <https://doi.org/10.1016/j.applthermaleng.2016.11.194>.
- [8] D. Zheng and W. Chen, “Thermal performances on angular contact ball bearing of high speed spindle considering structural constraints under oil air lubrication”, *Tribology International*, 109, (May 2017), pp. 593–601, DOI: <https://doi.org/10.1016/j.triboint.2017.01.035>.
- [9] D. Sy Truong, B. Sub-Kim, and S. Kook Ro, “An analysis of thermally affected High speed spindle with angular contact ball bearings”, *Tribology International*, 157, (May 2021), DOI: <https://doi.org/10.1016/j.triboint.2021.106881>.
- [10] C. Wei Lin, J. F. Tu, and J. Kamman, “An intergrated thermo mechanical dynamic model to characterize motorized machine tool spindles during very high speed rotations”, *International Journal of Machine Tools and Manufacture*, 43 (10), (Aug.

- 2003), pp. 1035–1050, DOI: <https://doi.org/10.1016/j.triboint.2018.09.031>.
- [11] Jafar Takabi and M.M. Khonsari, “Experimental testing and thermal analysis of ball bearings”, *Tribology International*, 60, (Apr. 2013), pp. 93–103, DOI: <https://doi.org/10.1016/j.triboint.2012.10.009>.
- [12] X. Zhou et al., “Investigation on thermal behavior and temperature distribution of bearing inner and outer rings”, *Tribology International*, 130, (Feb. 2019), pp. 289–298, DOI: <https://doi.org/10.1016/j.triboint.2018.09.031>.
- [13] S. Scott; A. Kovacs; L. Gupta; J. Katz; F. Sadeghi; D. Peroulis, “Wireless temperature microsensors integrated on bearings for health monitoring applications”, *IEEE International Conference on Micro Electro Mechanical Systems*, (2011), pp. 660–663, DOI: 10.1109/MEMSYS.2011.5734511.
- [14] Prashant K. Jain, Suneet Singh, and Rizwan-uddin, “Analytical Solution to Transient Asymmetric Heat Conduction in a Multilayer Annulus”, *Journal of Heat and Mass Transfer*, 131(1), (Jan. 2009), DOI: <https://doi.org/10.1115/1.2977553>.
- [15] K K Associates and Developers of thermal analysis, “Thermal Network Modelling Handbook”, *National Aeronautics and Space Administration*, 97(3), (2000), DOI: .
- [16] Oliver Walschied and Joachim Bcker, “Global Identification of a Low Order Lumped Parameter Thermal Network for Permanent Magnet Synchronous Motors”, *IEEE Transactions on Energy Conversion*, 31(1), (Mar. 2016), pp. 354–365, DOI: 10.1109/TEC.2015.2473673.
- [17] B. Fang et al., “An improved thermal performance modeling for high speed spindle of machine tool based on thermal contact resistance analysis”, *The International Journal of Advanced Manufacturing Technology*, 120, (Mar. 2022), pp. 5259–5268, DOI: <https://doi.org/10.1007/s00170-022-09085-4>.
- [18] J. Liu et al., “Thermal Structure Interaction Characteristics of a High Speed Spindle Bearing System”, *International Journal of Machine Tools and Manufacture*, 137, (Feb. 2019), pp. 42–57, DOI: <https://doi.org/10.1016/j.ijmachtools.2018.10.004>.
- [19] Chi Ma et al., “Simulation and experimental study on the thermally induced deformations of high speed spindle system”, *International Journal of Machine Tools and Manufacture*, 132, (Sep. 2018), pp. 3–16, DOI: <https://doi.org/10.1016/j.ijmachtools.2018.04.004>.
- [20] Ting-Yu Chen, Wei-Jiunn Wei, and Jhy-Cherng Tsai, “Optimum design of headstocks of precision lathes”, *International Journal of Machine Tools and Manufacture*, 39 (12), (Dec. 1999), pp. 1961–1977, DOI: [https://doi.org/10.1016/S0890-6955\(99\)00034-6](https://doi.org/10.1016/S0890-6955(99)00034-6).
- [21] L et al., “Thermal error reduction based on thermodynamics structure optimization method for an ultra precision machine tool”, *International Journal of Machine Tools and Manufacture*, 88, (May 2016), pp. 1267–1277, DOI: <https://doi.org/10.1007/s00170-016-8868-x>.
- [22] S. Cabezas, G. Hegedus, and P. Bencs, “A new Thermal Model of an Angular Contact Ball Bearing in Standard Arrangement subjected to Radial Loads based on State Variables and Control Volumes”, *Acta Polytechnica Hungarica*, 21(4), (2024), pp. 147–164, DOI: 10.12700/APH.21.4.2024.4.8.

- [23] Zheng De-xing, Chen Weifang, and Li Miaomiao, “An optimized thermal network model to estimate thermal performances on a pair of angular contact ball bearings under oil air lubrication”, *Applied Thermal Engineering*, 131, (Feb. 2018), pp. 328–339, DOI: <https://doi.org/10.1016/j.applthermaleng.2017.12.019>.
- [24] Jinhua Zhang et al., “Effect of preload on ball raceway contact state and fatigue life of angular contact ball bearing”, *Tribology International*, 114, (Oct. 2017), pp. 365–372, DOI: <https://doi.org/10.1016/j.triboint.2017.04.029>.
- [25] T. A. Harris and M. N. Kotzalas, “Rolling Bearing Analysis. Advanced Concepts of Bearing Technology”, *Taylor and Francis Group*, 5th Edition, (2006), DOI: .
- [26] Tao Xu et al., “A preload analytical method for ball bearings utilising bearing skidding criterion”, *Tribology International*, 67, (Nov. 2013), pp. 44–50, DOI: <https://doi.org/10.1016/j.triboint.2013.06.017>.
- [27] B. Bossmanns and Jay F. Tu, “A thermal model for high speed motorized spindles”, *International Journal of Machine Tools Manufacture*, 39, (Sep. 1999), pp. 1345–1366, DOI: [https://doi.org/10.1016/S0890-6955\(99\)00005-X](https://doi.org/10.1016/S0890-6955(99)00005-X).
- [28] Jenq-Shyong Chen and Kwan-Wen Chen, “Bearing load analysis and control of a motorized high speed spindle”, *International Journal of Machine Tools Manufacture*, 45 (12-13), (Oct. 2005), pp. 1487–1493, DOI: <https://doi.org/10.1016/j.ijmachtools.2005.01.024>.
- [29] A. B. Jones, “A General Theory for Elastically Constrained Ball and Radial Roller Bearings Under Arbitrary Load and Speed Conditions”, *Journal of Fluids Engineering*, 82(2), (Jun. 1960), pp. 309–320, DOI: <https://doi.org/10.1115/1.3662587>.
- [30] A. B. Jones, “Ball Motion and Sliding Friction”, *Journal of Fluids Engineering*, 81(1), (Mar. 1959), pp. 1–12, DOI: <https://doi.org/10.1115/1.4008346>.
- [31] H. Nguyen-Sch fer, “Computational design of rolling bearings”, *Springer*, First Edition, (Apr. 2016), DOI: <https://doi.org/10.1007/978-3-319-27131-6>.
- [32] Neng Tung Liao and Jen Fin Lin, “Ball bearing skidding under radial and axial loads”, *Mechanism and Machine Theory*, 37, (Jan. 2002), pp. 91–113, DOI: [https://doi.org/10.1016/S0094-114X\(01\)00066-0](https://doi.org/10.1016/S0094-114X(01)00066-0).
- [33] W. Bian et al., “Thermo mechanical analysis of angular contact ball bearing”, *Journal of Mechanical Science and Technology*, 30(1), (Jan. 2016), pp. 297–306, DOI: <https://doi.org/10.1007/s12206-015-1233-4>.
- [34] T. A. Harris and, “An Analytical Method to Predict Skidding in Thrust Loaded, Angular Contact Ball Bearings”, *Journal of Lubrication Technology*, 93(1), (Jan. 1971), pp. 17–23, DOI: <https://doi.org/10.1115/1.3451511>.
- [35] Neng Tung Liao and Jen Fin Lin, “A New Method for the Analysis of Deformation and Load in a Ball Bearing With Variable Contact Angle”, *Journal of Mechanical Design*, 123 (2), (Jun. 2001), pp. 304–312, DOI: <https://doi.org/10.1115/1.1357163>.
- [36] Palgrem A., “Ball and Roller Bearing Engineering”, *SKF Industries*, 3rd Edition, (1945), pp. 34–41, DOI: .
- [37] P. L. Wu et al., “Theoretical calculation models and measurement of friction torque for rolling bearings: state of the art”, *Journal of the Brazilian Society of Mechanical*

- Sciences and Engineering*, 44(435), (Aug. 2022), pp. 1–24, DOI: <https://doi.org/10.1007/s40430-022-03726-1>.
- [38] Pradeep. K. Gupta, Fred. B. Oswald, and Erwin V. Zaretsky, “Comparisson of Models for Ball Bearing Dynamic Capacity and Life”, *National Aeronautics and Space Administration*, (Jun. 2015), DOI: 10.1080/10402004.2015.1038860.
- [39] M. R. Lovell, M. M. Khonsari, and R. D. Marangoni, “Frictional Analysis of MoS2 Coated Ball Bearings: A Three Dimensional Finite Element Analysis”, *Journal of Tribology*, 119(44), (Oct. 1997), pp. 754–763, DOI: <https://doi.org/10.1115/1.2833881>.
- [40] Gentle et al., “Measurement of Cage and Pocket Friction in a Ball Bearing for Use in a Simulation Program”, *ASLE Transactions*, 28(4), (Mar. 2008), pp. 536–541, DOI: <https://doi.org/10.1080/05698198508981652>.
- [41] Kosmol Jan, “Analytical Determination of Rolling Friction Coefficient of Angular Bearings”, *Journal of manufacturing Science and Engineering*, 140(2), (Feb. 2018), DOI: <https://doi.org/10.1115/1.4037230>.
- [42] Iker Heras et al., “Friction torque in four point contact slewing bearings: Applicability and limitations of current analytical formulations”, *Tribology International*, 115, (Nov. 2017), pp. 59–69, DOI: <https://doi.org/10.1016/j.triboint.2017.05.011>.
- [43] Van-Canh Tong and Seong-Wook Hong, “Study on the running torque of angular contact ball bearings subjected to angular misalignment”, *Journal of Engineering Tribology*, 232 (7), (Sep. 2017), DOI: <https://doi.org/10.1177/1350650117732921>.
- [44] Tiago Cousseau et al., “Experimental measuring procedure for the friction torque in rolling bearings”, *Lubrication Science*, 22(4), (Apr. 2010), pp. 133–147, DOI: 10.1002/l.s.115.
- [45] M. Zander et al., “Evaluation of friction calculation methods for rolling bearings”, *Forschung im Ingenieurwesen*, 87, (Oct. 2023), pp. 1307–1316, DOI: <https://doi.org/10.1007/s10010-023-00715-1>.
- [46] John H. Tripp, “Hertzian Contact in Two and Three Dimensions”, *NASA*, (Jul. 1985), pp. 1–30, DOI: 85N32331.
- [47] Luc Houpert, “An Engineering Approach to Hertzian Contact Elasticity Part I”, *Journal of Tribology*, 123(3), (Jul. 2001), pp. 582–588, DOI: <https://doi.org/10.1115/1.1308043>.
- [48] Luc Houpert, “An Engineering Approach to Non Hertzian Contact Elasticity Part II”, *0*, 123(3), (Jul. 2001), pp. 589–594, DOI: <https://doi.org/10.1115/1.1308042>.
- [49] Wei Gao et al., “Machine tool calibration: Measurement, modeling, and compensation of machine tool errors”, *International Journal of Machine Tools and Manufacture*, 187, (Apr. 2023), DOI: <https://doi.org/10.1016/j.ijmachtools.2023.104017>.
- [50] Michael M. Khonsari and E. Richard Booser, “Applied Tribology. Bearing design and lubrication”, *John Wiley and Sons*, Third Edition, (2017), DOI: .
- [51] Chang Zhang et al., “Research on the influencing factors of thermal characteristics of high speed grease lubricated angular contact ball bearing”, *Advances in*

- Mechanical Engineering*, 13(6), (Jun. 2021), pp. 1–15, DOI: <https://doi.org/10.1177/16878140211027398>.
- [52] Piet M. Lugt, “Modern advancements in lubricating grease technology”, *Tribology International*, 97, (May 2016), pp. 467–477, DOI: <https://doi.org/10.1016/j.triboint.2016.01.045>.
- [53] Matthew Simpson et al., “An analytical friction model for point contacts subject to boundary and mixed elastohydrodynamic lubrication”, *Tribology International*, (Apr. 2024), DOI: <https://doi.org/10.1016/j.triboint.2024.109699>.
- [54] G.W. Stachowiak and A.W. Batchelor, “Engineering Tribology”, *Butterworth-Heinemann*, Third Edition, (Sep. 2005), DOI: .
- [55] Clare McCabe, Shengting Cui, and Peter T. Cummings, “Characterizing the viscosity temperature dependence of lubricants by molecular simulation”, *Fluid Phase Equilibria*, 183-184, (Jul. 2001), pp. 363–370, DOI: [https://doi.org/10.1016/S0378-3812\(01\)00448-4](https://doi.org/10.1016/S0378-3812(01)00448-4).
- [56] Shuyun Jiang and Hebing Mao, “Investigation of the High Speed Rolling Bearing Temperature Rise With Oil Air Lubrication”, *Journal of Tribology*, 133(2), (Jun. 2011), DOI: [10.1115/1.4003501](https://doi.org/10.1115/1.4003501).
- [57] William M. Hannon, “Rolling element bearing heat transfer Part I: Analytic model”, *Journal of Tribology*, 137(3), (Jul. 2015), DOI: <https://doi.org/10.1115/1.4029732>.
- [58] Theodore L. Bergman and Adrienne S. Lavine, “Fundamentals of Heat and Mass transfer”, *John Wiley and Sons*, Eight Edition, (2017), DOI: .
- [59] Kevin D. Cole et al., “Heat Conduction using Green’s Functions”, *CRC Press Taylor Frances Group*, Second Edition, (2011), DOI: .
- [60] G. Cinelli, “An extension of the finite hankel transform and applications”, *International Journal of Engineering Science*, 3(5), (Oct. 1965), pp. 539–559, DOI: [https://doi.org/10.1016/0020-7225\(65\)90034-0](https://doi.org/10.1016/0020-7225(65)90034-0).
- [61] K. Yan et al., “Thermal deformation coupling in internal thermal network for transient analysis of spindle bearing system”, *International Journal of Thermal Sciences*, 104, (Jun. 2016), pp. 1–12, DOI: <https://doi.org/10.1016/j.ijthermalsci.2015.12.007>.
- [62] Jenq-Shyong Chen and Wei-Yao Hsu, “Characterizations and models for the thermal growth of a motorized high speed spindle”, *International Journal of Machine Tools and Manufacture*, 43(11), (Sep. 2003), pp. 1163–1170, DOI: [https://doi.org/10.1016/S0890-6955\(03\)00103-2](https://doi.org/10.1016/S0890-6955(03)00103-2).
- [63] A. Clarke et al., “Heat Partition in Rolling/Sliding Elastohydrodynamic Contacts”, *Journal of Tribology*, 128(1), (Jan. 2006), pp. 67–78, DOI: <https://doi.org/10.1115/1.2125867>.
- [64] Evans et al., “The Role of Heat Partition in Elastohydrodynamic Lubrication”, *Tribology Transactions*, 53(2), (Jan. 2010), pp. 179–188, DOI: <https://doi.org/10.1080/10402000903097452>.
- [65] E. Uhlmann and J. Hu, “Thermal modelling of a high speed motor spindle”, *Procedia CIRP*, 1, (2012), pp. 313–318, DOI: <https://doi.org/10.1016/j.procir.2012.04.056>.

- [66] Wenjun Gao et al., “Validation and application of a numerical approach for the estimation of drag and churning losses in high speed roller bearings”, *Applied Thermal Engineering*, 153, (May 2019), pp. 390–397, DOI: <https://doi.org/10.1016/j.applthermaleng.2019.03.028>.
- [67] L. Q. Wang et al., “Operating temperature in high speed ball bearing”, *Journal of Mechanical Engineering Science*, 221(3), (Nov. 2006), pp. 353–359, DOI: <https://doi.org/10.1243/0954406JMES476>.
- [68] Wenjun Gao et al., “Model formulation of churning losses in cylindrical roller bearings based on numerical simulations”, *Tribology International*, 121, (May 2018), pp. 420–434, DOI: <https://doi.org/10.1016/j.triboint.2018.02.003>.
- [69] Jingyu Zhao et al., “Numerical Modeling of Unsteady Oil Film Motion Characteristics in Bearing Chambers”, *International Journal of Turbo Jet-Engines*, 32(3), (2015), pp. 233–245, DOI: <https://doi.org/10.1515/tjj-2014-0029>.
- [70] Wenjun Gao et al., “Numerical investigations on drag coefficient of circular cylinder with two free ends in roller bearings”, *Tribology International*, 123, (Jul. 2018), pp. 43–49, DOI: <https://doi.org/10.1016/j.triboint.2018.02.044>.
- [71] Yann Marchesse, Christophe Changenet, and Fabrice Ville, “Numerical Investigations on Drag Coefficient of Balls in Rolling Element Bearing”, *Tribology Transactions*, 57 (5), (Aug. 2014), pp. 778–785, DOI: <https://doi.org/10.1080/10402004.2014.911399>.
- [72] Thomas A. Lipo, “Introduction to AC Machine Design”, *IEEE Press*, (2017), DOI: .
- [73] Mihály Nemeth-Cséka, “Thermisches Management elektrischer Maschinen. Messung, Modell und Energieoptimierung”, *Springer Vieweg*, (2018), DOI: <https://doi.org/10.1007/978-3-658-20133-3>.
- [74] F. Pouly et al., “Investigations on the power losses and thermal behavior of rolling element bearings”, *Journal of Engineering Tribology*, 224 (9), (Jan. 2010), pp. 925–933, DOI: <https://doi.org/10.1016/j.triboint.2015.09.004>.
- [75] Y. Liu et al., “Improved thermal resistance network model of motorized spindle system considering temperature variation of cooling system”, *Advanced Manufacturing*, 6, (Nov. 2018), pp. 384–400, DOI: <https://doi.org/10.1007/s40436-018-0239-4>.
- [76] Kai Li, Shaoping Wang, and John P. Sullivan, “A novel thermal network for the maximum temperature rise of hollow cylinder”, *Applied Thermal Engineering*, 52(1), (Apr. 2013), pp. 198–208, DOI: <https://doi.org/10.1016/j.applthermaleng.2012.08.012>.
- [77] Changjiang Zhou et al., “Thermal network model and experimental validation for a motorized spindle including thermal mechanical coupling effect”, *The International Journal of Advanced Manufacturing Technology*, 115, (May 2021), pp. 487–501, DOI: <https://doi.org/10.1007/s00170-021-07221-0>.
- [78] Dexing Zheng, Weifang Chen, and Dateng Zheng, “An enhanced estimation on heat generation of angular contact ball bearings with vibration effect”, *International Journal of Thermal Sciences*, 159, (Jan. 2021), DOI: <https://doi.org/10.1016/j.ijthermalsci.2020.106610>.

- [79] Xu Min, Jiang Shuyun, and Cai Ying, “An improved thermal model for machine tool bearings”, *International Journal of Machine Tools and Manufacture*, 47(1), (Jan. 2007), pp. 53–62, DOI: <https://doi.org/10.1016/j.ijmachtools.2006.02.018>.
- [80] Yanfei Zhang et al., “Uneven heat generation and thermal performance of spindle bearings”, *Tribology International*, 126, (Oct. 2018), pp. 324–335, DOI: <https://doi.org/10.1016/j.triboint.2018.04.035>.
- [81] D. Niel et al., “Thermo mechanical study of high speed rolling element bearing: A simplified approach”, *Proceedings of the Institution of Mechanical Engineers, Part J: Journal of Engineering Tribology*, 233(4), (Dec. 2017), pp. 541–552, DOI: <https://doi.org/10.1177/1350650117750806>.
- [82] H. Blok, “The flash temperature concept”, *Wear*, 6(6), (Dec. 1963), pp. 483–494, DOI: [https://doi.org/10.1016/0043-1648\(63\)90283-7](https://doi.org/10.1016/0043-1648(63)90283-7).
- [83] Chao Jin, Bo Wu, and Youmin Hu, “Heat generation modeling of ball bearing based on internal load distribution”, *Tribology International*, 45(1), (Jan. 2012), pp. 8–15, DOI: <https://doi.org/10.1016/j.triboint.2011.08.019>.
- [84] Jialan Liu et al., “Thermal Structure Interaction Characteristics of a High Speed Spindle Bearing System”, *International Journal of Machine Tools and Manufacture*, 137, (Feb. 2019), pp. 42–57, DOI: <https://doi.org/10.1016/j.ijmachtools.2018.10.004>.
- [85] Kek-Kiong Tio and S.S. Sadhal, “Thermal constriction resistance: effects of boundary conditions and contact geometries”, *International Journal of Heat and Mass Transfer*, 35(6), (Jun. 1992), pp. 1533–1544, DOI: [https://doi.org/10.1016/0017-9310\(92\)90043-R](https://doi.org/10.1016/0017-9310(92)90043-R).
- [86] N. Laraqi and A. Bairi, “Theory of thermal resistance between solids with randomly sized and located contacts”, *International Journal of Heat and Mass Transfer*, 45(20), (Sep. 2002), pp. 4175–4180, DOI: [https://doi.org/10.1016/S0017-9310\(02\)00127-8](https://doi.org/10.1016/S0017-9310(02)00127-8).
- [87] M. Necati Ozisik et al., “Finite Difference Methods in Heat Transfer”, *CRC Press Taylor Frances Group*, Second Edition, (2017), DOI: .
- [88] Liqiu Wang, Xuesheng Zhou, and Xiaohao Wei, “Heat Conduction. Mathematical Models and Analytical Solutions”, *Springer Berlin, Heidelberg*, First Edition, (2008), DOI: 10.1007/978-3-540-74303-3.
- [89] Chi Ma et al., “Thermal characteristics analysis and experimental study on the high speed spindle system”, *The International Journal of Advanced Manufacturing Technology*, 79, (Feb. 2015), pp. 469–489, DOI: <https://doi.org/10.1007/s00170-015-6821-z>.
- [90] J.L. Stein and J.F. Tu, “A State Space Model for Monitoring Thermally Induced Preload in Anti Friction Spindle Bearings of High Speed Machine Tools”, *Journal of Dynamic Systems, Measurement, and Control*, 116(3), (Sep. 1994), pp. 372–386, DOI: <https://doi.org/10.1115/1.2899232>.
- [91] Roland S. Burns, “Advanced Control Engineering”, *Butterworth-Heinemann*, First Edition, (2001), DOI: .

- [92] James P. Lauffer et al., “Smart spindle unit for active chatter suppression of a milling machine: II. Dynamics and control”, *Proceedings of the SPIE*, 336, (Jun. 1998), pp. 167–173, DOI: [10.1117/12.310631](https://doi.org/10.1117/12.310631).
- [93] Y. S. Muzychka and M. M. Yovanovich and, “Thermal Resistance Models for Non Circular Moving Heat Sources on a Half Space”, *Journal of Heat and Mass Transfer*, 123(4), (Aug. 2001), pp. 624–632, DOI: <https://doi.org/10.1115/1.1370516>.
- [94] P.H. Mellor, D. Roberts, and D.R. Turner, “Lumped parameter thermal model for electrical machines of TEFC design”, *IEEE Proceedings B (Electric Power Applications)*, 138(5), (Sep. 1991), pp. 205–218, DOI: [10.1049/ip-b.1991.0025](https://doi.org/10.1049/ip-b.1991.0025).
- [95] A. Bejan, “Theory of Rolling Contact Heat Transfer”, *Journal of Heat and Mass Transfer*, 111(2), (May 1989), pp. 257–263, DOI: <https://doi.org/10.1115/1.3250672>.
- [96] Katsuhiko Nakajima, “Thermal Contact Resistance between Balls and Rings of a Bearing under Axial, Radial, and Combined Loads”, *Journal of Thermophysics and Heat Transfer*, 9(1), (Jan. 1995), pp. 88–95, DOI: <https://doi.org/10.2514/3.632>.
- [97] Tomohiro Shou, Shigeka Yoshimoto, and Tadeusz Stolarski, “Running performance of an aerodynamic journal bearing with squeeze film effect”, *International Journal of Mechanical Sciences*, 77, (Dec. 2013), pp. 184–193, DOI: <https://doi.org/10.1016/j.ijmecsci.2013.10.005>.
- [98] M. Sanchez-Rubio et al., “A new focus on the Walther equation for lubricant viscosity determination”, *Lubrication Science*, 18, (Apr. 2006), pp. 95–107, DOI: <https://doi.org/10.1007/s00170-022-09085-4>.
- [99] S. Cabezas, G. Hegedűs, and P. Bencs, “Transient heat convection analysis of a single rod in air cross flow”, *Pollack Periodica*, 18 (2), (Jul. 2023), pp. 23–28, DOI: <https://doi.org/10.1556/606.2023.00768>.
- [100] Van-The Than and Jin H. Huang, “Nonlinear Thermal Effects on High Speed Spindle Bearings Subjected to Preload”, *Tribology International*, 96, (Apr. 2016), pp. 361–372, DOI: <https://doi.org/10.1016/j.triboint.2015.12.029>.
- [101] SKF, “The SKF model for calculating the frictional moment.”, (2020), DOI: [https://cdn.skfmediahub.skf.com/api/public/0901d1968065e9e7/pdf\\_preview\\_medium/0901d1968065e9e7\\_pdf\\_preview\\_medium.pdf](https://cdn.skfmediahub.skf.com/api/public/0901d1968065e9e7/pdf_preview_medium/0901d1968065e9e7_pdf_preview_medium.pdf).
- [102] Manton SM, O Donoghue JP, and Cameron A., “Temperatures at lubricated Rolling sliding Contacts”, *Proceedings of the Institution of Mechanical Engineers*, 182(1), (1967), pp. 813–824, DOI: [10.1243/PIME\\_PROC\\_1967\\_182\\_061\\_02](https://doi.org/10.1243/PIME_PROC_1967_182_061_02).
- [103] C. V. Madhusudanda, “Thermal Contact Conductance”, *Mechanical Engineering Series*, Second Edition, (2014), DOI: [10.1007/978-3-319-01276-6](https://doi.org/10.1007/978-3-319-01276-6).
- [104] K. J. Negus and M. M. Yovanovich, “Constriction resistance of circular flux tubes with mixed boundary conditions by linear superposition of Neumann solutions”, *ASME Paper 84-HT-84*, (1984), pp. 1–6, DOI: .
- [105] S. Oechslen, “Thermische Modellierung elektrischer Hochleistungsantriebe”, *Springer Vieweg*, (Jul. 2018), DOI: <https://doi.org/10.1007/978-3-658-22632-9>.
- [106] Van-The Than et al., “Estimating time varying heat sources in a high speed spindle based on two measurement temperatures”, *International Journal of Thermal*

- Sciences*, 111, (Jan. 2017), pp. 50–65, DOI: <https://doi.org/10.1016/j.ijthermalsci.2016.08.004>.
- [107] Jianfu Zhang et al., “A method for thermal performance modeling and simulation of machine tools”, *International Journal of Advanced Manufacturing Technology*, 68, (Apr. 2013), pp. 1517–1527, DOI: <https://doi.org/10.1007/s00170-013-4939-4>.
- [108] Changlong Zhao and Xuesong Guan, “Thermal Analysis and Experimental Study on the Spindle of the High Speed Machining Center”, *2012 AASRI Conference on Computational Intelligence and Bioinformatics*, 1, (2012), pp. 207–212, DOI: [10.1016/j.aasri.2012.06.032](https://doi.org/10.1016/j.aasri.2012.06.032).
- [109] Kovács Endre and Majár János, “On some Analogous Transient Phenomena”, *Conference: MultiScience - XXXII. microCAD International Multidisciplinary Scientific Conference*, 1, (2018).